**RIGA TECHNICAL UNIVERSITY**

1862

# Katerīna Morozova

# PARAMETER ESTIMATION ON HYBRID ZENITH CAMERA AND GRAVIMETER DATA FOR INTEGRATED GRAVITY FIELD AND GEOID DETERMINATION BASED ON SPHERICAL-CAP-HARMONICS MODELLING

## Doctoral Thesis

Katerīna Morozova

Doctoral Thesis

# RIGA TECHNICAL UNIVERSITY

## K. Morozova

## Parameter Estimation on Hybrid Zenith Camera and Gravimeter Data for Integrated Gravity Field and Geoid Determination based on Spherical-Cap-Harmonics Modelling

# DOCTORAL THESIS

## 2022

**RIGA TECHNICAL UNIVERSITY**
Faculty of Civil Engineering
Department of Geomatics


**Katerīna MOROZOVA**
PhD Student of Doctoral Study Program "Construction"

# PARAMETER ESTIMATION ON HYBRID ZENITH CAMERA AND GRAVIMETER DATA FOR INTEGRATED GRAVITY FIELD AND GEOID DETERMINATION BASED ON SPHERICAL-CAP-HARMONICS MODELLING

**Doctoral Thesis**

Scientific Supervisors:
Dr.-ing., prof.,
**R. JÄGER**,
Dr. phys., prof.
**J. BALODIS**,
Dr.sc.ing, asoc. prof.
**J. KAMINSKIS**

**Riga**
**2022**

# ANNOTATION

The main objective of the Doctoral Thesis is to develop a new solution for the Earth gravity field determination based on spherical-cap-harmonic modelling, using both digital-zenith camera and gravimetric measurements' hybrid data. In first instance digital zenith cameras provide astronomic coordinates *(Φ, Λ)$_{ast}$* as information to the true gravity potential W of the Earth, in analogy to gravity values (*g*). *(Φ, Λ)$_{ast}$* give the direction vector in the observation point P of the true potential, and often called the geometrical information, while *g* is called physical information on W. Digital zenith camera is a new kind of astrogeodetic instruments, employing recent advancements in several technology areas (GNSS positioning, digital imaging, extensive and accurate astrometric reference star catalogues, and high resolution electronic tiltmeter technology) to obtain direct measurements of vertical direction *(Φ, Λ)* and derived vertical deflection ($ξ$, $η$) values. Over several years Institute of Geodesy and Geoinformatics (GGI) was engaged in design of the digital zenith camera. Presently the camera and data acquisition control and processing software are finished, and field measurements are actively done now. The intention is to use vertical deflection measurements along with GNSS/levelling and gravity data to improve a local gravity field and thus a local quasi-geoid model computation including both physical and geometrical data.

The method of Digital Finite Element Height Reference Surface software (DFHRS) is applied for this purpose, allowing the use of both physical observations and geometrical observation types. Main aspect is concerning the implementation of Spherical Cap Harmonics (SCH) modelling to local model of the potential, developing a general parameterization of gravity field related coefficients for a least squares' estimation. Terrestrial gravity measurements, deflections of vertical, height fitting points with known ellipsoidal and normal heights, and the use of the available global gravity models as additional observations will be used for quasi-geoid model determination. One of the aims is regarding the computation of a high precise local potential model W with the ability to derive all components related to the potential W. These observation components are gravity g, quasi-geoid height $ζ$, the geoid height N, deflections of the vertical in the east and north direction ($η$, $ξ$), the fitting points ($λ$, $ϕ$, h | H) and apriori information in terms of coefficients of a local potential model derived from the developed methods of a mapping of a global one. There are different types of Spherical Cap Harmonics, such as: Adjusted Spherical Cap Harmonics (ASCH), Translated-Origin Spherical Cap Harmonics (TOSCH) and the Revised

Spherical Cap Harmonics (RSCH) and the ASCH is chosen for the local gravitational potential modelling. The Spherical Cap Harmonics modelling encounters problems on the boundary, requiring application of the solution using an oversizing of the cap area with respect to the area of interest, but due to a lack of data near the borders, this is complicated task that still exist and should be investigated and solved.

The first chapter provides the fundamental theory of Earth gravity potential and quasi-geoid modelling, including the types of gravity data and methods of its processing and adjustment using both standard Least Squares and Robust estimation techniques. The height systems are described, and its physical differences are explained.

The second part introduces the development of Digital Zenith Camera at the Institute of Geodesy and Geoinformatics (GGI), the basic principle of vertical deflection determination, as well as its construction, measurement technique and data postprocessing is widely described in this chapter including all stages of data processing.

In the third chapter the principles of quasi-geoid determination are introduced, starting from DFHRS method and its stages of development and finishing with collocation method.

The fourth chapter concerns spherical harmonics and global gravity modelling, introducing spherical cap harmonic modelling and one of its methods – Adjusted Spherical Cap Harmonics modelling. The next part of this chapter concerns the basic principle of development of global gravity models and its techniques.

The fifth chapter introduces the results and analysis of quasi-geoid of Latvia based on new solution, where both vertical deflection data and gravity data are used. The summary results and conclusions of the fulfilled thesis are also discussed in this chapter.

The Thesis includes 39 figures, 127 formulas, and 7 tables. The total amount of PhD Thesis is 104 pages.

# ANOTĀCIJA

Promocijas darba mērķis ir izstrādāt jauno risinājumu Zemes gravitācijas lauka noteikšanai, balstoties uz sfērisko-segmenta harmoniku (SSH) modelēšanas iespējām izmantojot gravimetriskos un digitālās zenītkameras hibrīd-datus. Vertikāles nolieču vērtības, kuras izraisa gravitācijas lauka anomālijas, tiek aprēķinātas izmantojot digitālās zenītkameras mērījumus. Digitālā zenītkamera ir jaunas paaudzes astroģeodēziskais instruments, kurš apvieno jaunākas tendences no dažām tehnoloģiju jomām – GNSS pozicionēšana, digitālā attēla veidošana, paplašinātie un augstākās precizitātes astrometriskie zvaigžņu katalogi, un augstākās izšķirtspējas elektroniskā līmeņrāža tehnoloģija, ļauj aprēķināt vertikāles nolieču vērtības. Ģeodēzijas un ģeoinformātikas institūts pie digitālās zenītkameras izstrādes strādāja vairākus gadus. Šobrīd instruments un datu apstrādes programmatūra ir gatava un lauka mērījumi tiek veikti visā Latvijas teritorijā. Vertikāles nolieces kopā ar GNSS/nivelēšanas datiem un gravimetriskiem mērījumiem tiek izmantotas kvazi-ģeoīda precizitātes uzlabošanai, apvienojot gan fiziskos, gan ģeometriskos datus.

Digitālās galīgo elementu augstumu atbalsta virsmas programmatūra *(DFHRS – Digital Finite Element Height Reference Surface)* tiek izmantota šim nolūkam, ļaujot izmantot gan fiziskos gan ģeometriskos novērojumus. Viens no aspektiem ir sfērisko-segmenta harmoniku modelēšanas principa iekļaušana potenciāla lokālajā modelī, pēc mazāko kvadrātu metodes izstrādājot koeficientu parametrizāciju, un optimizējot datus, kuri ir nepieciešami koeficientu aprēķinam. Gravimetriskie dati, vertikāles nolieces, savietotie punkti ar zināmiem elipsoidāliem un normāliem augstumiem, globālie ģeopotenciāla modeļi tiek izmantoti kvazi-ģeoīda noteikšanai. Galvenais mērķis ir aprēķināt lokālo potenciāla modeli ar iespēju atvasināt visas komponentes, kas attiecas uz W potenciālu. Šīs novērojumu komponentes ir: gravimetriskie dati g, kvazi-ģeoīda augstums $\zeta$, ģeoīda augstums N, vertikālas nolieces ziemeļu un austrumu virzienā ($\xi$, $\eta$), savietotie punkti ($\lambda$, $\phi$, h | H) un primārā informācija par lokālā potenciāla modeļa koeficientiem, kuri ir atvasināti no globāliem modeļiem. Pastāv dažādi sfērisko-segmenta harmoniku tipi: izlīdzinātas sfēriskās-segmenta harmonikas, transformētas izcelsmes sfēriskās-segmenta harmonikas un koriģētas sfēriskās-segmenta harmonikas. Izlīdzinātas sfēriskās-segmenta harmonikas tika izvēlētas lokālā gravitācijas potenciāla noteikšanai. Šis modelēšanas princips saskarās ar robežproblēmu, un prasa

pielietot risinājumu, izmantojot lielāku segmentu, nekā interesējošais reģions, bet ārpus robežām datu trūkuma dēļ, tas ir sarežģīts uzdevums, kuru ir jāizpēta.

Pirmajā nodaļā tiek sniegts fundamentāls teorētisks izklāsts par Zemes gravitācijas potenciālu, ietverot gravimetrisko datu tipus, un to apstrādes un izlīdzināšanas metodes, izmantojot standartu mazāko kvadrātu metodi un robustas tehnoloģijas. Ir aprakstītas augstumu sistēmas un paskaidrotas to fizikālas atšķirības.

Otrajā nodaļā tiek aprakstīta Ģeodēzijas un ģeoinformātikas institūtā izstrādātā digitālā zenītkamera, vertikāles nolieces noteikšanas pamatprincips, zenītkameras konstrukcija, mērījumu tehnoloģija un datu apstrāde, kā arī vertikāles nolieču izmantošana kvazi-ģeoīda noteikšanā.

Trešajā nodaļā tiek demonstrēti kvazi-ģeoīda noteikšanas principi, sākot ar DFHRS metodi, un tā izstrādes posmiem, kā arī „remove-compute-restore" un kolokācijas metodes.

Ceturtā nodaļa skar sfēriskās harmonikas un globālā gravitācijas lauka modelēšanu, aprakstot sfērisko-segmenta harmoniku modelēšanu un vienu no tās metodēm – izlīdzinātas sfēriskās-segmenta harmonikas.

Piektajā nodaļā tiek atspoguļoti pētījuma rezultāti un Latvijas kvazi-ģeoīda analīze, kurš balstās uz jauno risinājumu. Šajā nodaļā tiek aprakstīti kopējie promocijas darba rezultāti un secinājumi.

Promocijas darbs ietver 39 attēlus, 127 formulas, un 7 tabulas. Darba kopējais apjoms ir 104 lappuses.

# ACKNOWLEDGMENTS

*Riga, September 2022*

*Katerina Morozova*

# CONTENT

# ACRONYMS

ASCH – Adjusted Spherical Cap Harmonics

BHS-77 – Baltic Height System 1977

CCD – Charged Coupled Devices

DTM – Digital Terrain Model

DTU – Technical University of Denmark

DoV – Deflection of Vertical

DZC – Digital Zenith Camera

DTM – Digital Terrain Model

DFHRS – Digital Finite-element Height Reference Surface

EGG97 – European Gravimetric Geoid 1997

EIGEN6C4 – Global Gravity Field Model by GFZ-Potsdam

EGM2008 – Earth Geopotential Model 2008

EGM2020 – Earth Geopotential Model 2020

ERS-1 - European remote sensing satellite

ETRS89 – European Terrestrial Reference System 1989

EVRF2007 – European Vertical Reference Frame 2007

FFT – Fast-Fourier Transform

FOD – First-order design problem

GGI – Institute of Geodesy and Geoinformatics

GNSS – Global Navigation Satellite System

GGM – Global Geopotential Model

GPM – Global Potential Model

GOGRA – Gravity geoid model developed from GOce and GRAce data

GLONASS – GLObalnaya NAvigatsionnaya Sputnikovaya Sistema – Global Navigation
Satellite system by Russian Federation

GRAVSOFT - GRAVity field modelling SOFTware

HSKA – HochSchule KArlsruhe – University of Applied Sciences

HRS – Height Reference Surface

IAG – International Association of Geodesy

KTH – Royal Institute of Technology in Stockholm

LAS – 2000.5 – Latvijas Augstumu Sistēma – Latvian Height System epoch 2000.5

LatPos – Latvian Positioning System

LAV – Local Astronomical Vertical

LGV – Local Geodetic Vertical

LGIA – Latvian Geospatial Information Agency

LV'14 – Latvian Quasi-Geoid Model 2014

LV98 – Latvian Quasi-Geoid Model 1998

LS – Least Squares

LSC – Least Squares Collocation

LSE – Least Squares Estimation

LU_GGI'20 – Latvian Quasi-Geoid Model 2020

NAVSTAR GPS– Navigation Signal Timing and Ranging Global Positioning System

NGA – National Geospatial-Intelligence Agency

NKG – Nordic Geodetic Commission

RTK – Real Time Kinematics

RWLSE – Robust Weighted Least Squares Estimation

SH – Spherical Harmonics

SCH – Spherical Cap Harmonics

UL – University of Latvia

VESTA – VErtical by STArs

# INTRODUCTION

## Subject topicality and formulation of the problem

The most important theoretical works on geoid determination using gravity observations belong to Stokes (1849) who proved that for theoretical studies of the Earth surface it is important to determine the gravity potential W on its surface and outer space and the equipotential surfaces, which have a form of approximately ellipsoidal shape. According to Stokes' theory, all the masses must be under equipotential surface which is called geoid. Besides, gravity measurements are carried out on the physical surface which does not coincide with geoid. The main task was to include corrections in measured gravity values, which would move all masses under sea level, without changing the equipotential surface, thus referring gravity measurements to the sea level (geoid). This problem has been widely discussed in scientific literature and is called the problem of the Earth regularization. But it was discovered that it is necessary to know the internal structure of the Earth for successful regularization.

In 1945, the Russian scientist M. S. Molodensky (*Molodensky, 1945, Molodensky et al., 1960, Molodensky, 2001*) proved that all the possible regularization solutions are quite similar but do not solve the problem strictly and offered an alternative solution for precise Earth figure and height determination. According to his theory, the heights (since than the term of "normal heights" has been used) are not determined in relation to the geoid, but to another surface, which is close to the geoid, and called it "quasi-geoid".

The first quasi-geoid in Latvia was developed in 1998 by Kaminskis (2010), and the estimated precision of this quasi-geoid was 6-8 cm. For the computation of this quasi-geoid various kind of data were used – satellite altimetry data obtained by ERS-1 as well as ~500 terrestrial gravity measurements and ~12000 digitized gravimetric points that were included in modelling. In 2014 in Latvia normal height system was changed from BAS-77 to LAS-2000.5, thus the need for a new more precise quasi-geoid model was obvious, therefore in the same year, the Latvian Geospatial Information Agency (LGIA) developed a new quasi-geoid LV'14 based on the remove-restore technique which is implemented in GRAVSOFT software. As input data, 4886 relative gravity measurements, 84 GNSS/levelling points, free air gravity anomaly model DTU13 from satellite altimetry, DTM model and GOGRA02s GGM were used, and it is the only quasi-geoid

which can be used in Latvia now, though the estimated precision of this quasi-geoid is 3–4 cm. Further (1-3 cm) quasi-geoid model has been computed for Latvia in 2012-2013 (*Jäger et al., 2012, Janpaule et al., 2013).* Of course, this precision is not sufficient anymore, e.g. Galileo positioning system has been launched and operated now and, as a result, the precision of GNSS observations has also been improved; many other satellite missions are also taking place now. Many countries have already achieved the precision of up to 1 cm level of quasi-geoid model (*Ellmann et al., 2019), (Farahani et al., 2017*), challenging project has been performed in Colorado (*Wang et al., 2021*) and others. Moreover, with the development of digital zenith camera in the institute of Geodesy and Geoinformatics (GGI) it became possible to use vertical deflection data for the quasi-geoid improvement, combining the deflection of vertical data, gravity data and fitting points. The solution of combining both geometrical $(\Phi, \Lambda)_{ast}$ and physical data (g) has not been implemented yet, and was not found by the author in scientific literature.

## Objective and tasks of the Doctoral Thesis

Nowadays, due to the fast developments of GNSS techniques, the development of a high accuracy (up to 1 cm) quasi-geoid model is very important and actual task because it allows to determine normal height (or orthometric height) directly from ellipsoidal height which is performed by GNSS and, of course, this method is much faster and easier for land surveyors in comparison to levelling measurements. The aim of the PhD Thesis is to offer a new solution for gravity field determination in terms of spherical-cap-harmonics modelling as a carrier function of the gravity potential *(W)* and to compute a precise quasi-geoid model, using all available data for it: both vertical deflection observations, gravity values and fitting points. Precise quasi-geoid model can be used in civil engineering, road and bridge constructions, as well as engineering geodesy and topography, etc. So, in order to carry out this research, the following tasks were defined:

- to investigate all possible terrestrial data for gravity field modelling and quasi-geoid determination, such as GNSS/levelling points, astronomical directions *(Φ, Λ)$_{ast}$* and derived vertical deflection *(ξ, η)* observations, as well as gravity values *g*, and to implement them in DFHRS software in terms of integrated geodesy by applying spherical-cap-harmonics parameterization of *W*;

- to describe the method of vertical deflection determination and data processing using the developed in GGI software;

- to evaluate the results of vertical deflection values in comparison to Global geopotential models (GGMs);

- to investigate different methods for gravity field and quasi-geoid determination and compare the modelling methods;

- to analyse the obtained results using the territory of Latvia as a test area and to make conclusions and summarize PhD Thesis.


## Scientific novelty of the Thesis

- There are different techniques for gravity field and quasi-geoid determination, but all of them are based mostly on gravity data as a function of the quasi-geoid based on the theory of Stokes. The extended and improved method of Digital Finite element Height Reference Surface software (DFHRS) allows to compute Height Reference Surface (HRS) in the context of GNSS and in terms of an integrated approach allowing the combination both of gravity data ($g$) and vertical deflection observation data ($\xi$, $\eta$), using in first instance the computation of the gravity potential W in its parameterization by spherical-cap-harmonics coefficients and then applying Molodensky theory to derive $N_{QG}$.

- Digital Zenith Camera (DZC) VESTA (VErtical by STArs) which has been developed in Latvia at the Institute of Geodesy and Geoinformatics (GGI) and has acquired an operational status allows to determine vertical deflection values. It is also quite a unique instrument and at the moment only about 5 such instruments are known in the world (e.g. in China, Germany, Switzerland and Turkey). The advantage of VESTA in comparison with other cameras is its precision – about 0.1 arcsec, moreover, it is portable, and therefore it is convenient for field observations. The measurement technique of vertical deflection and data processing software are presented in this Thesis. For the first time terrestrial vertical deflections have been used for quasi-geoid determination in Latvia.

- The above mentioned technique allows to compute up to 1 cm precise quasi-geoid model for the whole territory of Latvia, which has not been done before, and, of course, this solution can be applied not only in Latvia, but also in any other country or separate territory

in the world. It would be especially interesting to use the developed camera in mountain areas, where levelling is more expensive and less accurate.

- The provided results and their analysis are unique, as the presented research which combines both physical observations (gravity data) and geometrical data (GNSS/levelling points and vertical deflection observations) has not been introduced and implemented before.


## Practical relevance of the Doctoral Thesis

The new developed method allows to compute a high precision quasi-geoid model which can be used in civil engineering, road and bridge construction and other similar fields for precise normal height determination. According to the legal acts of the Cabinet of Ministers of the Republic of Latvia, it is allowed to use any quasi-geoid model the precision of which is higher than the precision of LV'14. This means that the developed quasi-geoid model can be officially used, so to say, not only for scientific research, but also in practice. It only has to undergo the validation, which can be done by LGIA.

The method can be very valuable in mountain areas, as well as in the regions of inappropriate levelling points, or insufficient amount of the points, e.g. Mongolia (Ulaanbaatar), where only one 1st order line goes through the city, which is not providing the polygons for adequate adjustment. But in this case it would be very useful to make observations by DZC, first of all, to check independently the levelling data, and secondly, to cover the region of interest by doing a sufficient amount of observations.

# 1. THE GRAVITY FIELD OF THE EARTH

The external gravity field plays a fundamental role in geodesy. This is because the figure of the earth has evolved under the influence of gravity, and most geodetic observations refer to gravity. Thus, modelling of observations requires knowledge of the gravity field. In addition, the analysis of the gravity field yields information on the structure of the earth's interior; in this way geodesy contributes to geophysics (*Torge, 2001*).

The force acting on a body at rest on the earth's surface is the resultant of gravitational force (v) and the centrifugal force (z) of the earth's rotation:

$$g = v + z \tag{1.1}$$

The force of gravity F is obtained by scaling *g* by the mass *m*:

$$F = mg \tag{1.2}$$

The Earth's gravitation is obtained by Newton's law of gravitation:

$$v(r) = G \iiint\limits_{Earth} \frac{r' - r}{|r' - r|^3} dm \tag{1.3}$$

where $r'$ and r are the geocentric position vectors of the source point $P'$ (mass element *dm*) and the attracted point P (unit mass m = 1), respectively. The value of gravitational constant is:

$$G = 6.673 \times 10^{-11} \, m^3 kg^{-1} s^{-2} \tag{1.4}$$

The mass element *dm* can be expressed by the volume density $\rho = \rho(r')$ and the volume element *dv* as:

$$dm = \rho dv \tag{1.5}$$

The centrifugal acceleration, as an inertial acceleration in a rotating system, is given by the vector of Earth rotation $\omega$ and the perpendicular distance to the rotation axis *d*:

$$z(r) = (\omega \times r) \times \omega = \omega^2 d \qquad (1.6)$$

Where the angular velocity of the Earth:

$$\omega = 7.292115 \times 10^{-5} \, rad \, s^{-1} \qquad (1.7)$$

is known to a high degree of accuracy from astronomy (*Torge, 1989*).

## 1.1.    Fundamentals of potential

The representation of the gravity field and related computations are simplified if we consider the scalar quantity "potential" instead of the vector quantity "acceleration". The corresponding potentials V and Z exist for the gravitational and centrifugal fields with the relationships *(Torge, 1989)*:

$$v = gradV, z = gradZ. \qquad (1.8)$$

For the gravitational potential of the Earth we have with (1.3) and (1.5)

$$V(r) = G \iiint\limits_{Earth} \frac{\rho(r')}{|r' - r|} dv, \lim_{r \to \infty} V = 0 \qquad (1.9)$$

and for the centrifugal potential with (1.6)

$$Z(r) = \frac{\omega^2}{2} d^2, \qquad (1.10)$$

the sum of the potential functions is the gravity potential of a mass point rotating with the earth:

$$W(r) = V(r) + Z(r). \qquad (1.11)$$

The unit of the potential is $m^2 s^{-2}$. The potential may be considered as work required for the displacement of a unit mass within the gravity field.

In analogy to (1.8) the relationship between gravity and gravity potential is:

$$g = gradW. \tag{1.12}$$

The gravity components in a certain direction are obtained as partial derivatives of W. In the global X, Y, Z system we have *(Torge, 1989):*

$$\boldsymbol{g}^T = (W_X, W_Y, W_Z) \tag{1.13}$$

$$\text{with } W_X = \frac{\partial W}{\partial X}, W_Y = \frac{\partial W}{\partial Y}, W_Z = \frac{\partial W}{\partial Z}$$

$$\text{and } |g| = \sqrt{W_X^2 + W_Y^2 + W_Z^2},$$

$$\Phi_{ast} = tan^{-1}\left(\frac{W_Z}{\sqrt{W_X^2 + W_Y^2}}\right) \text{ and}$$

$$\Lambda_{ast} = tan^{-1}\left(\frac{W_Y}{W_X}\right) \text{ see (3.18) and (3.19) respectively.}$$

## 1.2. Terrestrial gravity measurements

Terrestrial gravimetry consists of point measurements of the earth's gravity field on its physical surface. Terrestrial gravity on a complex physical surface contains all spectral information of gravity (*Yang, 2013*). There are two methods for the determination of gravity values – absolute and relative one. In this chapter both methods are described, and the determination of gravity values are introduced.

### 1.2.1. Absolute gravity measurements

Absolute measurements can be done by two different methods. The pendulum method is based on measuring the pendulum time *T* of a pendulum with length *l* very accurately. The accuracy of this observation is increased by observing the pendulum during a long time. The gravity value *g* is found with formula (*Ogorodova et al., 1978*) (1.14):

$$T = 2\pi \sqrt{\frac{l}{g}} \qquad (1.14)$$

The length of the pendulum and the influence of the suspension point need to be known very precisely. With a pendulum it is possible to determine absolute gravity values with a precision of some milligal. After 1975 the pendulum method was superseded by the 'free fall method' and the "rise-and-fall method", which is based on a falling prism in a vacuum tube (*Crombaghs et al., 1999*). Through the integration of $z = g$ for a free-fall experiment, one obtains the basis formula:

$$z = z_0 + \dot{z}_0 t + \frac{g}{2} t^2 \qquad (1.15)$$

Between the path $z$ and the fall time $t$. The constants of integration $z_0$, $\dot{z}_0$ represent the position and velocity of the body at $t=0$. If the body falls through at least three planes (Figure 1.1a), $z$ and $\dot{z}_0$ can be eliminated. We get:

$$g = 2 \frac{(z_3 - z_1)(t_2 - t_1) - (z_2 - z_1)(t_3 - t_1)}{(t_3 - t_1)(t_2 - t_1)(t_3 - t_2)} . \qquad (1.16)$$

For a symmetric rise and fall (Figure 1.1b), it is sufficient to measure the crossing times $t_1, t_2, t_3, t_4$ at only two planes (separated by the distance $\Delta z$). (1.16) then yields:

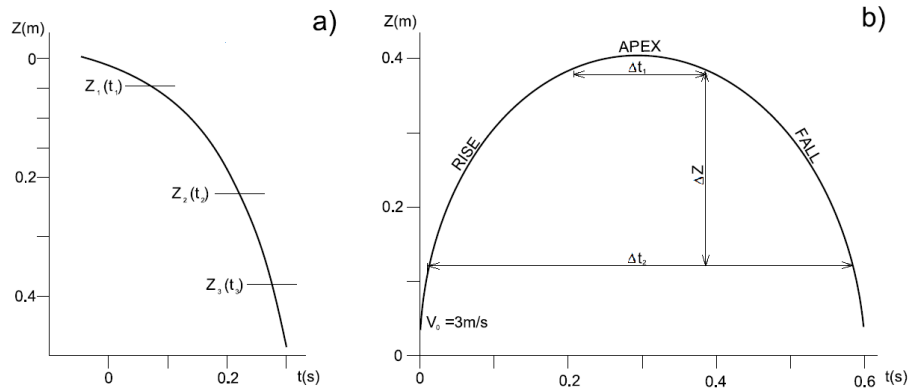$$g = \frac{8\Delta z}{(t_4 - t_1)^2 - (t_3 - t_2)^2} \qquad (1.17)$$



Figure 1.1. Distance-time diagram a) free-fall method b) symmetrical rise and fall method
(*Torge, 1989*)

19

Absolute gravimeters now in use measure the free fall of a body in a vacuum, using lasers and optical interferometry, to obtain accuracies of better than 0.01 mGals under favourable conditions (i.e. *Niebauer et al., 1986* and *Torge, 1989*). Whereas, these devices are transportable, they are still quite bulky and time consuming to set up and read. Typically, only one absolute reading per day can be made. Nevertheless, such absolute gravimeters are being routinely employed in establishing the absolute values of gravity at selected stations, which then may serve as base stations for relative gravity surveys, so that the results of the latter may then be expressed in absolute gravity terms, with almost the same accuracy as the values for the absolute stations themselves. Absolute gravity measurements are necessary as a base for relative gravity measurements, for the calibration of relative gravimeters, and for determining the drift of relative gravimeters (*Parseliunas et al., 2011*).

## 1.2.2. Relative gravity measurements

Relative gravity measurements are based on a completely different principle: the elongation of springs with a small weight attached to them is measured. The most popular relative gravimeters are Scintrex CG3, CG5, CG6 (Canada) and LaCoste Romberg (The US) (*Lobanov, 2017*). Taking measurements at different locations yields differences in elongation. These differences can be converted to gravity differences, on the condition that the instrument is calibrated on stations with known absolute gravity values. One relative measurement takes about 15 minutes, while a complete absolute measurement takes at least half a day. Well calibrated instruments can measure gravity differences with a precision up to 5 microgal *(Crombaghs et al., 1999).*

Relative gravity measurements allow to define only the difference of gravity between two stations ($\Delta$g) and these measurements are fundamental for determination of gravity values (*Ogorodova & Yuzefovich, 1980*). It is a common practice to collect redundant observations to ensure a better quality of gravity determination, and then gravity observations must be adjusted using an adequate mathematical and stochastic model *(Hwang et al., 2002).* Gravity measurements may contain gross (also called outliers), random and systematic errors. Systematic errors are basically caused by gravimeter drift and calibration factor.

## 1.2.2.1. Relative gravity data processing and its adjustment

There are different ways of gravity network adjustment and in this chapter some methods are introduced: the most common is based on least squares and more precise based on robust estimation.

The relative gravity observation equation is written as (*Hwang et al., 2002*):

$$l(t) + v = g + N_0 + \Delta F(z) + D(t),$$ (1.18)

where $t$ is the time of the measurement; $l(t)$ – the observed gravity value (z) multiplied by a calibration factor, $v$ – is the residual of $l(t)$; $g$ – gravity value at the reference station; $N_0$ – constant bias; $\Delta F(z)$ is the calibration function; $z$ – gravimeter reading, $D(t)$ – the drift of the gravimeter. For the stochastic modelling $\Delta F(z)$ and $D(t)$, in Eq. (1.18) are called systematic errors of the gravimeter. Here we model $\Delta F(z)$ as in (*Torge, 1989*):

$$\Delta F(z) = \sum_{l=1}^{r} b_l z^l + \sum_{l=1}^{s} (x_l cos\omega_l z + y_l sin\omega_l z),$$ (1.19)

where $b_l$, $x_l$, $y_l$ – are the coefficients, $\omega_l$ – the frequency of the reading $z$ and $r$, $s$ are the numbers of terms to model. The drift of gravimeter can be modelled as a polynomial:

$$D(t) = \sum_{p=1}^{a} d_p (t - t_0)^p,$$ (1.20)

where $t_0$ is an initial epoch and $a$ is a degree of the polynomial. So, the observation equation between two stations $i$ and $j$ is:

$$\Delta l_{i,j} + v_{i,j} = g_j - g_i + (\Delta F(z_j) - \Delta F(z_i)) + (D(t_j) - D(t_i)),$$ (1.21)

where $v_{i,j}$ – is the residual of $\Delta l_{i,j}$ and $\Delta l_{i,j} = l_j - l_i$, $t_j$ and $t_i$ – measurement times. Assuming that $n$ is the number of observations, in matrix form we get the observation equation:

$$l^b + v = Ax$$ (1.22)

$l^b$ is n ×1 vector of relative observations, weight matrix of constraints is $W_g$; $v$ - is n ×1 vector of residuals; $A_g$ is design matrix, and $x$ is the vector of unknowns (gravity values and gravimeter parameters). By inspecting the structure of $A$, the solution by least squares method is not possible

without constraint because **A** has rank defect of 1 (*Hwang et al. 2002*). In order to obtain a unique solution in the least squares sense, e.g. method of weighted constraints can be used (*Touati et al., 2009*):

$$\hat{x} = \left(A_g^T W_g A_g + A_g^T W_g A_g\right)^{-1} \cdot \left(A_g^T W_g l^b + A_g^T W_g l_g\right) \tag{1.23}$$

Where

$\hat{x}$ – estimates of **x;**

$l_g$ – absolute gravity vector (*Hwang et al., 2002*).

## 1.3.  Introduction to height systems

The geoid is used in geodesy, cartography, and oceanography as a reference surface for heights and depths (continental and ocean bottom topography, as well as sea surface topography). A point P can be attributed to a specified level surface by its gravity potential W (Figure 1.2). With respect to the geoid potential $W_0$, the "height" of P is given by the negative potential difference to the geoid, which is called the geopotential number C. We get from (*Hofmann-Wellenhof and Moritz, 2006*):

$$dW = -gdn \tag{1.24}$$

$$C = W_0 - W_P = -\int_{P_0}^{P} dW = \int gdn \tag{1.25}$$

The integral is independent of the path: hence, $P_0$ is an arbitrary point on the geoid. C can be determined from geometric levelling and gravity measurements along any path between $P_0$ and P.
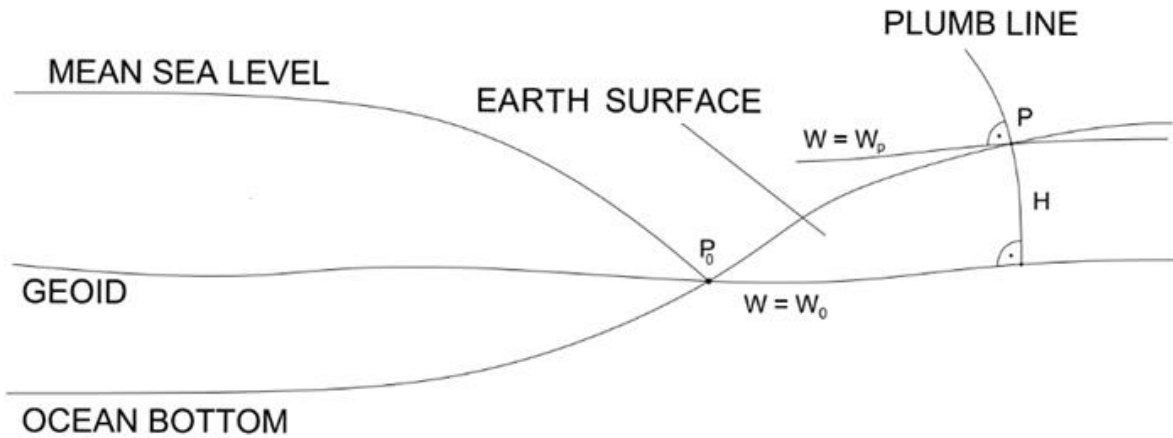
Figure 1.2. Geoid, mean sea level, continental and sea surface topography (*Torge, 2001*)

The geopotential number is an ideal measure for describing the behaviour of masses (e.g. water masses) in the gravity field. It could be used as a "height" in several applications, as in hydraulic engineering and oceanography. A more general use is limited by the potential unit $m^2s^{-2}$, which is in contradiction to the obvious demand for a metric height system that employs the "meter" unit. In order to achieve a certain agreement with the numerical value of the height in meters, the geopotential unit (gpu) 10 $m^2s^{-2}$, is also used for the geopotential number. With $g \approx 9.8$ m/s$^{-2}$, the values of C are about 2% smaller than the corresponding height values.

## 1.3.1. Dynamic heights

The dynamic height $H^{dyn}$ is obtained by dividing the geopotential number through a constant gravity value. The normal gravity for the surface of the level ellipsoid at certain latitude, usually 45° latitude is used (*Hofmann-Wellenhof and Moritz, 2006*):

$$H^{dyn} = \frac{C}{\gamma_0^{45}} \qquad (1.26)$$

The surfaces $H^{dyn}$ = const. remain equilibrium surfaces. Hence, points located on the same level surface have the same dynamic height. Unfortunately, a geometric interpretation of the dynamic heights is not possible, and larger corrections are necessary to convert levelling results into dynamic height differences:

$$\Delta H_{AB}^{dyn} = \Delta n_{AB} + k_{AB}^{dyn} \tag{1.27}$$

Where

$$k_{AB}^{dyn} = \int_{B}^{A} \frac{g - \gamma_0^{45}}{\gamma_0^{45}} dn \approx \sum_{A}^{B} \frac{g - \gamma_0^{45}}{\gamma_0^{45}} \delta n \tag{1.28}$$

is a dynamic correction.

That is why dynamic heights have not been widely used in Geodesy. National or continental height systems, and terrain-data based on them (topographic maps, DTM), use either orthometric or normal heights (*Hofmann-Wellenhof and Moritz, 2006*).

## 1.3.2. Orthometric heights

The orthometric height H is defined as the linear distance between the surface point and the geoid, reckoned along the curved plumb line (Figure 1.2). This definition corresponds to the common understanding of "heights above sea level". Expanding the right-hand side of (1.25) in H and integrating along the plumb line from $P_0$ *(H=0)* to *P (H)* we obtain (*Hofmann-Wellenhof and Moritz, 2006*):

$$H = \frac{C}{\bar{g}}, \bar{g} = \frac{1}{H} \int_{0}^{H} g dH \tag{1.29}$$

$\bar{g}$ is the mean gravity along the plumb line; gravity values inside the earth are required for its calculation. This is performed by introducing a model of the density distribution of the topographic masses. As this distribution is known only imperfectly, the accuracy of computed orthometric heights depends on the accuracy of the density model. In addition, points of equal orthometric height deviate slightly from a level surface, which is due to the non-parallelism of the level surfaces. These drawbacks are compensated by the fact that orthometric heights represent the geometry of the topographic masses. Geometric levelling only needs small corrections for the transformation into orthometric height differences (*Hofmann-Wellenhof and Moritz, 2006*).

### 1.3.3. Normal heights

The normal heights (geometric heights) are not supposed to describe the heights above the geoid (*Tenzer et al., 2012*). They relate the points to another surface known as quasi-geoid, which is close to the geoid, but not a level surface (*Sjoberg, 2018*), in order to avoid any hypothesis on the distribution of the topographic masses (*Vaniček, 1976; Foroughi & Tenzer, 2017*). Normal heights $H^N$ have been introduced by Molodensky and are used in many countries (*Vaniček et al, 2012*). The mean gravity $\bar{g}$ in (1.28) is replaced by the mean normal gravity $\bar{\gamma}$ along the normal plumb line, which is only slightly curved:

$$H^N = \frac{C}{\bar{\gamma}} \ , \bar{\gamma} = \frac{1}{H^N} \int\limits_{0}^{H^N} \gamma dH^N \tag{1.30}$$

$\bar{\gamma}$ can be calculated in the normal gravity field of an ellipsoidal earth model. The quasi-geoid deviates from the geoid on the mm to cm order at low elevations and may reach one-meter deviation in the high mountains. On the oceans, geoid and quasi-geoid practically coincide *(Sanchez, 2013).*

# 2. DIGITAL ZENITH CAMERA

The digital zenith camera is a portable astrometric instrument for vertical deflection measurements – angular difference between gravity field direction and normal to reference ellipsoid that can be used for local quasi-geoid precision improvement, Earth crust movement monitoring, local geological structure qualities determination, etc. There are only several DZC known in the world, e.g. TZK2-D or DIADEM (*Hirt et al., 2005; Hirt et al., 2010a; 2010b*), but in comparison to these cameras, our camera is portable and more convenient for field observations. At present the camera system developments have been completed, and more than 400 observations have been done in Latvia. The principle of digital zenith camera is based on the determination of plumb line by astronomical coordinates (Φ, Λ). The stars serve as orientation and approximately 20 stars around zenith frame should be used for observations. The precision of the developed digital zenith camera is about 0,1-0,2 arc seconds. The advantage of using deflections of the vertical observations for quasi-geoid determination is the provision of terrestrial gravity field information, which is independent from errors in local vertical datum (*Featherstone & Lichti, 2008*), (*Voigt et al., 2009*). GNSS techniques allow to determine geodetic (ellipsoidal) coordinates (*Celms et al., 2017*), as well as the exact time of positioning, which is needed for the astronomical zenith camera observations (Φ, Λ) for the modelling of the precession, nutation and Earth rotation terms.

## 2.1.      Basic principle of Vertical Deflections determination

Astronomical coordinates (Φ, Λ) define positions on earth surface and equatorial coordinates (δ, α) define positions of stars on the celestial sphere (Figure 2.1). The relationship of unreduced deflections related to the Earth surface, and the quasi-geoid is shown in Figure 2.2.
Both coordinate systems are linked by Greenwich apparent sidereal time – GAST (the hour angle of the vernal equinox) regarding the Earth's rotation (*Hirt & Burki, 2003*). The astronomic latitude Φ and longitude Λ determine the direction of the tangent to the plumb line and is defined by digital zenith camera and the geodetic coordinates (φ, λ) define the direction of the ellipsoid normal using GNSS techniques (*Halicioglu et al., 2012a, Haliciolgu et al., 2012b*).
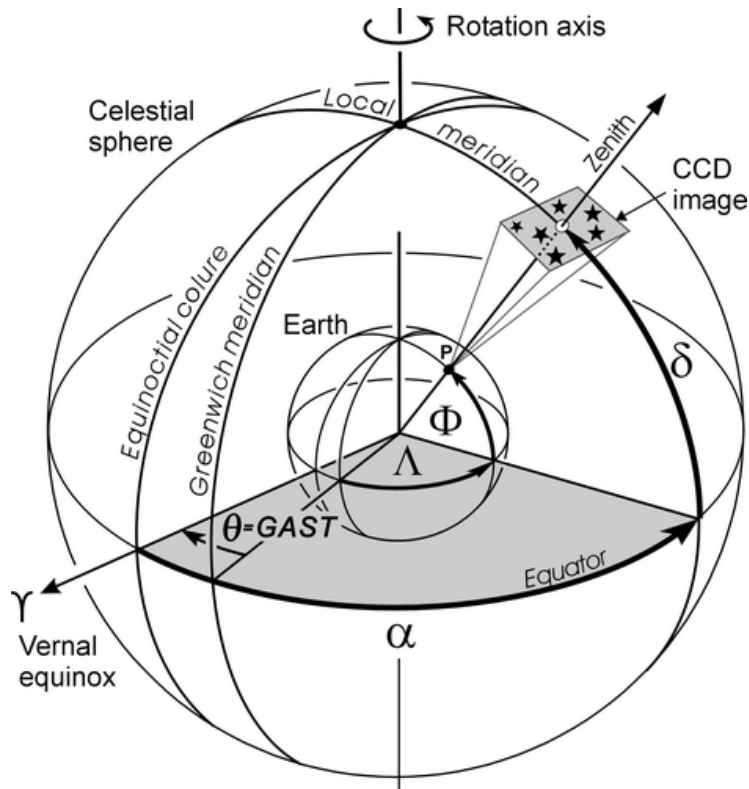
Figure 2.1. Basic principle of the determination of the plumb line ($\Phi$, $\Lambda$) by imaging the stars in zenith direction (*Hirt & Burki, 2003*).
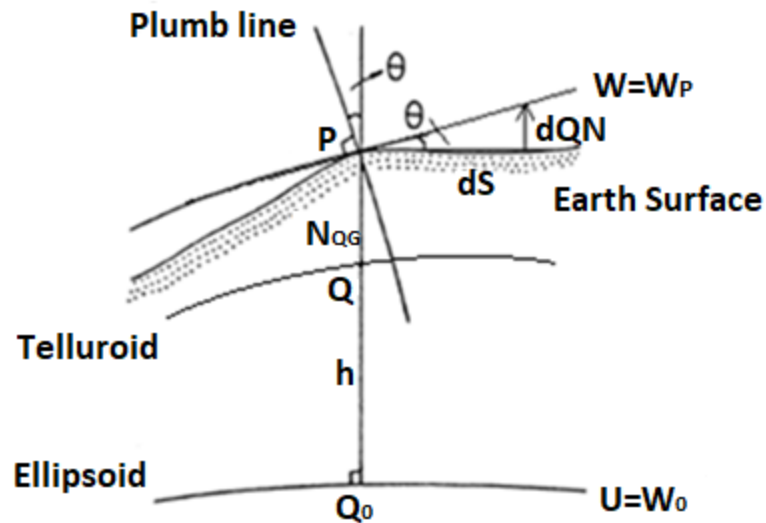


Figure 2.2. The relationship of unreduced deflections of vertical related to the Earth surface and the quasi-geoid (*author*)

Deflection of the vertical is the angular difference between plumb line direction and normal to the surface and consists of north and east component ($\xi$, $\eta$) (*Ceylan, 2009*). Deflections of the vertical can be calculated using astronomical coordinates ($\Phi$, $\Lambda$) and geodetic (ellipsoidal) coordinates reading (*Torge, 2001*):

$$\xi = \Phi - \varphi, \tag{2.1a}$$

$$\eta = (\Lambda - \lambda) \cdot \cos\varphi \tag{2.1b}$$

The component $\varepsilon$ in the azimuth $\alpha$ can be computed using $\xi$ and $\eta$ components:

$$\varepsilon = \xi \cos\alpha + \eta \sin \alpha \tag{2.2}$$

Equations (2.1a, b) and (2.2) are valid for all definitions of the deflection of the vertical.

The differential relationship between geoid height and deflection of the vertical is defined through the following formulae (*Heiskanen & Moritz, 1984; Vaniček, 1976*):

$$-dN = \varepsilon \cdot ds \ or \ \varepsilon = -\frac{dN}{ds} \tag{2.3}$$

By combining formulae (2.2) and (2.3) we obtain:

$$-\frac{dN}{ds} = \xi \cos\alpha + \eta \sin\alpha \ or \tag{2.4}$$

$$-\frac{\Delta N}{\Delta s} \approx \xi \cos\alpha + \eta \sin\alpha \tag{2.5}$$

## 2.2.  Construction of Digital Zenith Camera

The design of digital zenith camera was started in 2010 by Institute of Geodesy and Geoinformatics (*Abele et al., 2012*). Zenith camera consists of a rotating assembly, placed on a roughly (a few arc minutes) levelled platform (see Figure 2.3). Any rotation position can be used. Camera assembly is levelled with a few arc second accuracy in each rotation position using 3 linear actuators. After that a number of zenith area star images are obtained together with high resolution tiltmeter readings. An on-board GNSS receiver is used to obtain geocentric site coordinates and support accurate image timing. Hardware control and data acquisition is done by an on-board control computer. An observation session typically lasts 20-40 minutes.

Figure 2.3. Digital Zenith camera (VESTA – VErtical by STArs) (*author*)

## 2.3.     The principle of measurement method

GNSS provide geocentric coordinates (15-20 cm) in precise UTC time (10 mks) in order to compute the direction of normal to reference ellipsoid in astrometric coordinate system. Observations of reference stars provide instrument position of main axis relatively to normal of reference ellipsoid. Indications of tiltmeter provide corrections of inclination for base axis of the instrument relatively to plumb line. The difference between these positions should give vertical deflection, in case when all options and zero points of tiltmeter are precise. In practice, range of measurements should be done in different positions in order to exclude estimation errors.

The basic component are imaging sensors (CCD cameras) to track the camera-platform **p** or an object (b), on which p is mounted by stars S. For the unification of Astronomical Directions and Deflections of the Vertical by a camera platform p and the attitude determination $\mathbf{R}_b^{LGV}(r, p, y)$ of the body (b), the imaging sensor system and platform p are taken here as being axe-parallel to the body system (b).  In case that the camera system p is not mounted axe-parallel to the body (b) the

additional so-called lever-arm matrix $\mathbf{R}_p^b(\epsilon_x, \epsilon_y, \epsilon_z)$ can always be considered to rotate the resulting attitude matrix $\mathbf{R}_b^{LGV}(r, p, y)$ of the camera-system (p=b) to the true physical body (b).



Figure 2.4. Modern Startracker CT-602 Camera System for Navigation of Aircraft, as produced by Ball Aerospace's CT-602

So we have for the 3D platform-based vector **p** coordinates with p=b and the related normalized direction vector $r_S^b$ of the body system:

$$\mathbf{p}^{b,S} = \begin{bmatrix} x - x_0 \\ y - y_0 \\ f \end{bmatrix} \quad \text{and so, the direction vector} \quad \mathbf{r}^{b,S} = \frac{p}{|p|} = \frac{1}{|p|} \cdot \begin{bmatrix} x - x_0 \\ y - y_0 \\ f \end{bmatrix} \tag{2.6}$$

with

$(x, y)_{t\_UTC}$ – observed image coordinates of a star $S(\delta, \alpha)$ at time t_UTC;

$(x_0, y_0)$ – principal point of the image;

f – focal length of the sensor (see Figure 2.4) (*Hofman-Wellenhof et al., 2003*).

The transformation of the image star image-based vector $\mathbf{r}^{b,S}$ from the body-system to the local astronomical geodetic vertical system (LAV) system reads:

$$\mathbf{r}^{LAV,S} = \mathbf{R}_b^{LAV}(r, p, y) \cdot \mathbf{r}^{b,S} \tag{2.7}$$

$$\mathbf{R}_b^{LAV} = \begin{pmatrix} \cos p \cos y & \sin r \sin p \cos y - \cos r \sin y & \cos r \sin p \cos y + \sin r \sin y \\ \cos p \sin y & \sin r \sin p \sin y + \cos r \cos y & \cos r \sin p \sin y - \sin r \cos y \\ -\sin p & \sin r \cos p & \cos r \cos p \end{pmatrix} \quad (2.8)$$

where *p, y* and *r* are the pitch-, yaw- and roll-angle of the zenith-camera platform p as body with respect to the LAV. On the other hand, we get for an observed star $S(\alpha, \delta)$ transformed from its Cartesian coordinates from the ECIF inertial system (i)

$$r^{i,S} = \begin{pmatrix} \cos \delta \cdot \sin \alpha \\ \cos \delta \cdot \cos \alpha \\ \sin \delta \end{pmatrix} \quad (2.9)$$

to the ECEF at time t by

$$R_i^e(t\_UTC) = R_{Polar} \cdot R_{Earth-Rotation} \cdot R_{Nutation} \cdot R_{Pr\,ecession} \cdot R_{Eigen} \quad (2.10)$$

(*Xu, 2007*), and we get

$$r^{e,S}(t\_UTC) = R_i^e(t\_UTC) \cdot r(\alpha, \delta)^{i,S} \quad (2.11)$$

By the astronomical coordinates $(\Phi, \Lambda)$ and the rotation matrix

$$\mathbf{R}_e^{LAV}(\Phi, \Lambda) = \begin{bmatrix} -\cos \Lambda \cdot \sin \Phi & -\sin \Lambda \cdot \sin \Phi & \cos \Phi \\ -\sin \Lambda & +\cos \Lambda & 0 \\ \cos \Lambda \cdot \cos \Phi & \sin \Lambda \cdot \cos \Phi & \sin \Phi \end{bmatrix} \quad (2.12)$$

we get finally arrive at

$$r^{LAV,S}(t\_UTC) = \mathbf{R}_e^{LAV}(\Phi, \Lambda) \cdot R_i^e(t\_UTC) \cdot r(\alpha, \delta)^{i,S} \quad . \quad (2.13)$$

(2.6) and (2.13) lead to

$$\mathbf{R}_b^{LAV}(r, p, y) \cdot \mathbf{r}^{b,S} - \mathbf{R}_e^{LAV}(\Phi, \Lambda) \cdot R_i^e(t\_UTC) \cdot r(\alpha, \delta)^{i,S} = 0 \quad (2.14)$$

The matrix $\mathbf{R}_e^{LAV}(\Phi, \Lambda)$ in (2.14) can be replaced by

$$\mathbf{R}_e^{LAV}(\Phi, \Lambda) = \mathbf{R}_{LGV}^{LAV} \cdot \mathbf{R}_e^{LGV} \quad (2.15)$$

With

$$\mathbf{R}_e^{LGV}(B,L) = \begin{bmatrix} -\cos L \cdot \sin B & -\sin L \cdot \sin B & \cos B \\ -\sin L & \cos L & 0 \\ \cos L \cdot \cos B & \sin L \cdot \cos B & \sin B \end{bmatrix} \tag{2.16}$$

And

$$\mathbf{R}_{LGV}^{LAV} = \mathbf{R}_e^{LAV} \cdot (\mathbf{R}_e^{LGV})^T = \mathbf{R}_{LGV}^{LAV} = \mathbf{R}_{LGV}^{LAV}(B,L,\Phi,\Lambda) =$$

$$\begin{pmatrix} \sin B \sin\Phi \cos(\Lambda - L) + \cos B \cos\Phi & \sin B \sin(\Lambda - L) & \cos B \sin\Phi - \sin\phi\cos\Phi\cos(\Lambda - L) \\ -\sin\Phi\sin(\Lambda - L) & \cos(\Lambda - L) & +\cos\Phi\sin(\Lambda - L) \\ \sin B \cos\Phi - \cos B \sin\Phi\cos(\Lambda - L) & -\cos B \sin(\Lambda - L) & \cos B \cos\Phi\cos(\Lambda - L) + \sin B \sin\Phi \end{pmatrix}^T$$

$$\tag{2.17}$$

$$\mathbf{R}_{LGV}^{LAV} \cong \begin{pmatrix} 1 & \eta \cdot \tan B & \xi \\ -\eta \cdot \tan B & 1 & -\eta \\ -\xi & \eta & 1 \end{pmatrix}^T \tag{2.18}$$

*(Jekeli, 2001)*

With (2.15) to (2.18) we get from (2.14):

$$\mathbf{R}_b^{LAV}(r,p,y) \cdot \mathbf{r}^{b,S} - \mathbf{R}_{LGV}^{LAV}(B,\xi,\eta) \cdot \mathbf{R}_e^{LGV}(B,L) \cdot \mathbf{R}_i^e(t\_UTC) \cdot \mathbf{r}(\alpha,\delta)^{i,S} = \mathbf{0} \tag{2.19}$$

and, as an alternative in the LGV:

$$\mathbf{R}_b^{LGV}(r,p,y) \cdot \mathbf{r}^{b,S} - \mathbf{R}_e^{LGV}(B,L) \cdot \mathbf{R}_i^e(t\_UTC) \cdot \mathbf{r}(\alpha,\delta)^{i,S} = \mathbf{0} \tag{2.20}$$

Use of the equations (2.14) and (2.19), (2.20):

1) The equation (2.14) can be used for the determination of the astronomical position and absolute vertical directions $(\Phi, \Lambda)$ at position P by zenith camera measurements $\mathbf{r}^{b,S}$ to stars S. Here an inclinometer is needed to determine the tilts $(r, p)$. The yaw angle is (also) common to the measurements of all stars S, and can remain as an unknown in the equation. The GNSS position (P) is only needed for a georeferencing, namely to relate $(\Phi, \Lambda)$ to a gravity field model V (W = V(P) + Z(P)) in case of a further use of $(\Phi, \Lambda)$ for gravity field determination $V(r, \varphi, \lambda)$ as (B,L,h) $\Leftrightarrow$ (B,L,h) $\Leftrightarrow$ $(r, \varphi, \lambda)$.

2) The equation (2.19) can be used - like (2.14) but now together with an early use of the GNSS georeferencing P(B,L,h) - to determine the vertical deflections ($\xi, \eta$) at location P for gravity field determination and quasi-geoid determination by astronomical levelling.

3) Equation (2.20) can be used for navigation, namely attitude determination (r,p,y), as (r,p,y) in navigation are related to the LGV = n-frame (n-frame = Navigation frame). Here (B,L,h), more precisely only (B,L) for GNSS are actively used.

## 2.4. Control Software

The data and control processing software is designed as a single program under Windows system. It can be run either in measurement or post-processing mode. Difference between modes is mainly in data acquisition hardware treatment. On-board control process is monitored and controlled by remote terminal via "RemoteDesktop" connection. Though data processing and vertical deflection determination can be done in real time, this kind of mode is time-consuming and not practical. Generally, measurement data are saved in file system and processed later using post-processing mode. Exceptions are some critical data quality indicators, such as tiltmeter data dispersion and quality of star images on CCD image, which always are calculated in real time. Several control parameters, involved in measurement process, are stored in software configuration file and can be adjusted by operator (*Zarins et al., 2016*).

## 2.5. Raw data processing

Though the post-processing can be carried out within the control computer, downloading of the raw observation data to a safe location on a hard disk for a post-processing is a better option. Results of the observation session are stored in a numerous text and image files, contained in a specific directory of the session.

Technically, post-processing consists of:

• complementing the data with the Earth Orientation Parameters (EOP) and site coordinates;

• setting of the processing modes and parameters;

• execution of astrometric reduction of frames;

• calculation of ellipsoidal zenith position on frames;

• calculation of tiltmeter corrections;

- calculation of session model parameters.

Though the reasonable predicted values of EOP are available only in some days after measurement session, e.g. [ftp://cddis.gsfc.nasa.gov/pub/products/iers/](ftp://cddis.gsfc.nasa.gov/pub/products/iers/) the use of corrected values is beneficial for accuracy and credibility of the results. Therefore, post-processing is better to be done after this period of observations.

## 2.5.1. Processing settings

Raw data contain site coordinates, available to the control program, but they can be replaced by more accurate values in several ways:

- Site coordinate values can be edited directly in the session information file;

- Site coordinates can be entered in a sites database entry;

- Average values of site coordinate messages, obtained from on-board GNSS, can be set to session data.

Following processing settings are most likely to be modified:

- Batch processing mode includes such options as:
  - what kind of data subset should be processed: astrometric and/or leveling;
  - if the existing star image and identification data should be used or ignored;
  - if the existing solutions should be cleared (both astrometric and leveling; no any calculations in this mode);
  - which frame subset must be recalculated: all / those without astrometric solution / those, for which number of identified stars is less than indicated;

- star image recognition settings;

- autoImg and autoID modes: if set, star image recognition and/or identification will be performed on frame loading, if have not been done successfully before. For batch processing this mode is set by default;

- Identification mode – first option:
  - solution of the previous frame is attempted first. May make process considerably faster, but may also promote false identification to all subsequent frames of a position;
    Second option:
  - geometric similarity identification is attempted. It is the basic choice, but in some cases may produce false identification.

- Identification and star association tolerances: minimum star number, number of brightest images, used in ID, which accept RMS star association tolerance ("star from image"), ID timeout;
- Reference star selection parameters:
  - maximum magnitude: generally, value of 13.5 to 14 is optimal, but in case of bad sky conditions or bad focusing quality may be beneficial to decrease it to 11-13.
  - radius of star selection area: generally, 0.23 dg is enough, but if zenith is far away from the center of frame, it should be slightly increased to ensure full coverage of image. It can be changed by slider or in radius edit field of the main dialog.
- Focus distance value, especially if focusing has been significantly changed. The value is taken from the configuration, and it can be adjusted for the session needs by entering the value;
- Level correction settings: linear drift can be estimated, and it slightly improves the accuracy, but tiltmeter timing must be accurate at least within one second.
- Model residual outlier rejection limits (separate for stars and tiltmeter); values 2 - 2.5 are found to be optimal.

## 2.5.2. Frame processing

Frame processing can be done manually, frame by frame, or in batch mode (all frames below the current frame list selection, satisfying batch settings). In regular situation, batch mode is the first choice, after batch calculations are done; unsuccessful or suspicious frames can be reviewed individually, selecting a frame in the list for processing. When frame data is loaded, the image file should be displayed with star image and reference star marks on top. If there are more than 6 stars on the image and no major errors in data, automatic identification should be successful. If it fails, comparison with the other frames of the same position can reveal the problem. Often, trying astrometric solution of one of nearby frames for the same position is enough for identification. If identification is successful, frame astrometric model parameters are calculated by described below algorithm.

The purpose of astrometric reduction of star field images is to find the transformation, linking CCD coordinate system with inertial reference frame, defined by star positions. When such transformation is found, geocentric zenith point can be projected to CCD coordinate system, providing data for calculations of vertical deflection value.

Turner transformation with 6 or 4 parameters is used:

$$X = X_0 + A \cdot x + B \cdot y \tag{2.22a}$$

$$Y = Y_0 + C \cdot x + D \cdot y \tag{2.22b}$$

where $X$, $Y$ – CCD coordinates,

$x$, $y$ – topocentric apparent places of stars:

$$x = z \cdot \sin(A) \tag{2.23a}$$
$$y = -z \cdot \cos(A) \tag{2.23b}$$

where $z$ – apparent zenith distance,

$A$ – apparent azimuth,

$X_0, Y_0, A, B, C, D$ – parameters of transformation. In case of 4-parameter transformation $A= -D$ and $C=B$.

Interpretation of parameters is:

$X_0, Y_0$ – offset;

$F_x = \sqrt{(A^2 + B^2)}$ – image scale (focus distance) along $x$ axis;

$F_y = \sqrt{(C^2 + D^2)}$ – image scale (focus distance) along $y$ axis;

$tg(Ax - \pi) = \frac{B}{A}$ – CCD X-axis orientation azimuth;

$tg(Ay - \pi) = -\frac{C}{D}$ – CCD Y-axis orientation azimuth.

The values of transformation parameters are calculated using Least Squares algorithm on the set of normal equations (2.22a, 2.22b), composed of data for all identified stars and images.

As, because of shutter and star movement, there is small difference of scales along $X$ and $Y$ axes, 6–parameter model fits a little better then otherwise quite sufficient 4-parameter variant.

When transformation is acquired, ellipsoidal zenith point coordinates on CCD can be calculated, inserting $x=0$, $y=0$ in (2.22a, 2.22b), respectively, Xz=$X_0$; Yz=$Y_0$. For convenience $Xz$ and $Yz$ are reduced to the center of CCD.

Frame model calculation process is controlled and visualized in Astrometric groupbox of Session dialog (Figure 2.5).
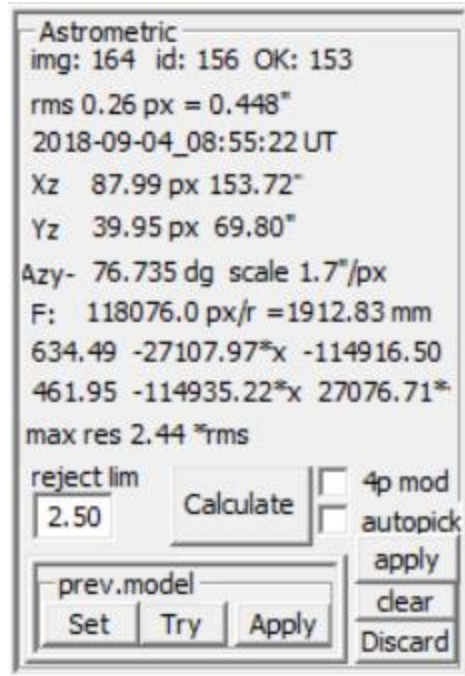
Figure 2.5. Astrometric groupbox of Session dialog

## 2.5.3. Tiltmeter data processing

As processing of tiltmeter data is much simpler than astrometric, a variant of residual tilt corrections (interpolated tilt values for exposure moment) is calculated already during frame acquisition and saved in frame information file along with raw tiltmeter readings. It can be used as it is or can be recalculated during the post-processing. Controls for manual operations with tiltmeter data are located in "Level" groupbox of Session dialog (Figure 2.6).
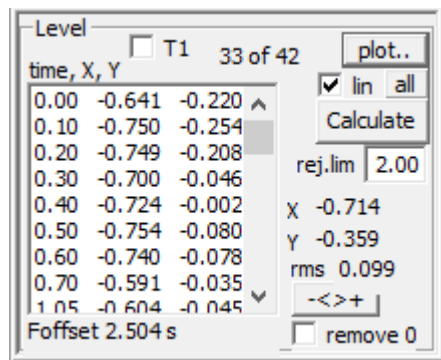


Figure 2.6. Level groupbox session dialog

The listbox contains list of tiltmeter readings (copy of it is located in the frame information file). "Calculate" button starts approximation of tilt values with 1-parameter (average value) or 2-

parameter (linear dependency on time; if checkbox "lin" is checked) model. Residual rejection tolerance in field "rej.lim" (in rms units) is used to discard outliers. "all" button can be used to reverse all rejections. "remove 0" checkbox is meant for discarding all near-zero values for case of malformed data exchange. "-<>+" button inverts status of the selected reading. Resulting average values and RMS are displayed next to listbox. "Plot" button opens model visualization dialog (Figure 2.7). Two modes of visualization are supported: XY plot and time dependency. In case of time dependency ("drift" checkbox checked) horizontal (X) coordinate is time from the first reading of the frame (range indicated below graph, usually 4-8 seconds); Y coordinate shows tilt values (channel X: red, Y: blue) in arc seconds, exposure moment is marked with vertical line, interpolated tilt values for that moment are marked by horizontal lines. Approximated linear trends are shown by lines of respective color. Marks for rejected outliers have thinner lines.
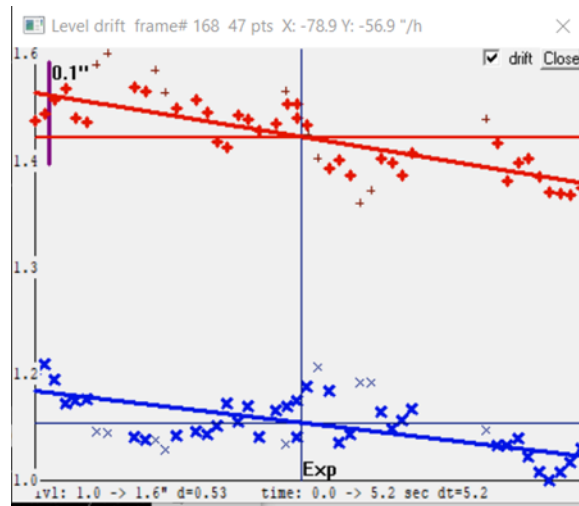


Figure 2.7. Model visualization dialog

## 2.5.4. Residual tilt corrections

To find corrected ellipsoidal zenith coordinates *dX* and *dY* measured residual tilt values *x, y* must be transformed to CCD coordinate system. For that purpose, model of CCD and tiltmeter relative orientation (Figure 2.10) is used. It assumes, that CCD axes are fairly orthogonal; tiltmeter axes are oriented in some angles (*dAx*, *dAy*) relative to corresponding CCD axes. The transformation is:

$$dX = X \cdot S - (x \cdot Sx \cdot cosdAx - y \cdot Sy \cdot sindAy) \qquad (2.24a)$$

$$dY = Y \cdot S - (y \cdot Sy \cdot cosdAy + x \cdot Sx \cdot sindAx) \qquad (2.24b)$$

where

*X, Y* – zenith coordinates on CCD (in pixels);

*x, y* – tiltmeter readings;

*S* – CCD scale factor (pix. size / focus distance);

*Sx, Sy* – tiltmeter scale factors, introduced because of approximate nature of their factory calibration.
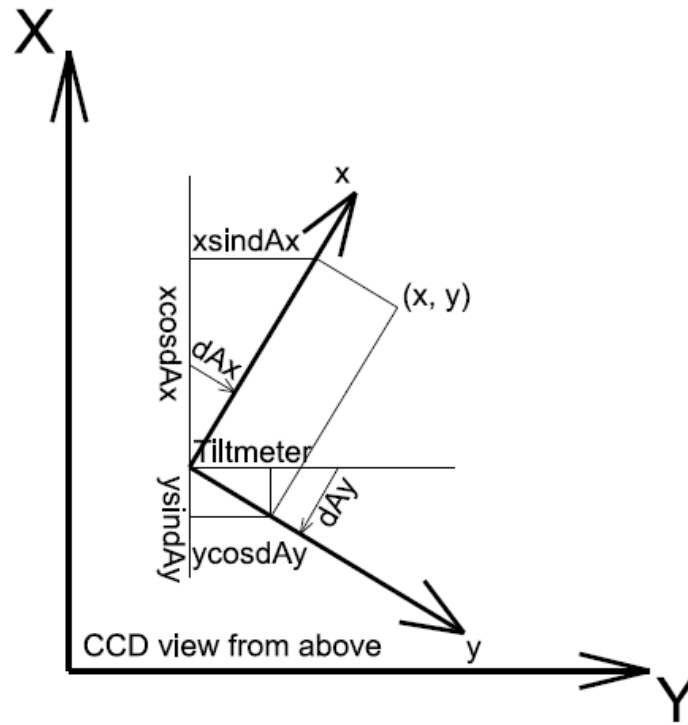


Figure 2.8. Model of CCD and tiltmeter relative orientation

Scale factor *S* is obtained by astrometric processing of the frame. *Sx, Sy, dAx* and *dAy* are instrument calibration constants, determined by special calibration measurement procedure (see 2.8).

Values of *x, y, X, Y* and *S* are stored in frame information file. Other calibration constants are stored both in session information file and program configuration. The transformation (2.24 a, b) is performed every time when processing of the session is requested.

## 2.5.5. Calculation of session model parameters

In order to find vertical deflection value, an approximating model is used, describing dependency of ellipsoidal zenith coordinates (corrected for residual tilt) on rotation angle (instrument orientation azimuth) in rotating CCD coordinate system:

$$dY = Y_0 + dZy \cdot cosA + dZx \cdot sinA + Yt \cdot dT \qquad (2.25a)$$

$$dX = X_0 - dZy \cdot sinA + dZx \cdot cosA + Xt \cdot dT \qquad (2.25b)$$

where

*dX, dY* – corrected ellipsoidal zenith coordinates;

$X_0$, $Y_0$ – center of trajectory, representing location of plumb line projection on CCD;

*dZy, dZx* – components of vertical deflection (same as ξ in North-South and η in West-East directions respectively; positive if geoid height increases in S and E directions);

*A* – frame orientation (negative direction of CCD Y axis) azimuth;

*Xt, Yt* – drift, represents linear part of dependency of $X_0$, $Y_0$ on time;

*dT* – time (from the first frame exposure moment);

Drift is included in model only on request ("drift" checkbox checked).

A Least Squares algorithm is used to determine model parameters $X_0$,$Y_0$, *dZx, dZy, Xt, Yt*. As always, outliers are removed, and model calculation repeated until all residuals are smaller than rejection tolerance.

Button "Model" of Session dialog is used to initialize model calculation. It opens Model dialog, calculation results and more control elements are located there. Mode "diff a-l" must be selected to use model (2.24 a, b), the other two modes are meant for approximation of only astrometric or only tiltmeter data for calibration or diagnostic purposes.

## 2.6.    Model visualization and controls

The model (2.25 a, b) represents circle on CCD coordinate plane, moving in time if drift components are included. In order to visualize it (Figure 2.9), marks of corrected zenith points are connected with residual lines to corresponding places on solution trajectory, forming bunches of measurement positions along model trajectory. For model itself only one circle, corresponding to driftless situation at the moment of the first position, is drawn.  From the center of this circle

(representing projection of plumb line in that moment) a line is drawn to the point, representing model position with CCD orientation azimuth 0. As it can be seen from formulas (2.25 a, b), relative placement of such point illustrates value of vertical deflection (but in topocentric, non-rotating coordinate system, which might be a little confusing to comprehend with other contents being in rotating CCD system. Axes of topocentric system are drawn in the center of circle).

Drift, if present, can be easily visualized only in the case if orientation azimuth has been linear function of time, what practically never happens. In real situation, orientation azimuth is wildly jumping along session. Nevertheless, an evenly moving spiral, representing linear dependency case, can be drawn (checkbox "drift"), however, it will coincide with real positions only occasionally.

There is a number of drawing options, controlled by checkboxes in the upper right corner of dialog window:

• "residuals" (by default on): drawing of residual lines and lines, connecting consecutive positions;

• "E-W": lines are drawn for all measurements, indicating E-W direction on CCD;

• "astro & lvl": marks for raw measurements (both astrometric and tiltmeter);

• "connect": lines, connecting consecutive measurements are drawn;

• "all": also measurements, not included in current subset, are drawn;

• "frame #" (by default on): frame numbers are indicated beside marks;

• "pos #":  position numbers and azimuth values are indicated beside corresponding places;

• "outline": draws solution outline for astro/level model types;

• "drift": draws model spiral; number of turns must be indicated;

"Redraw" button redraws the picture with actual options.
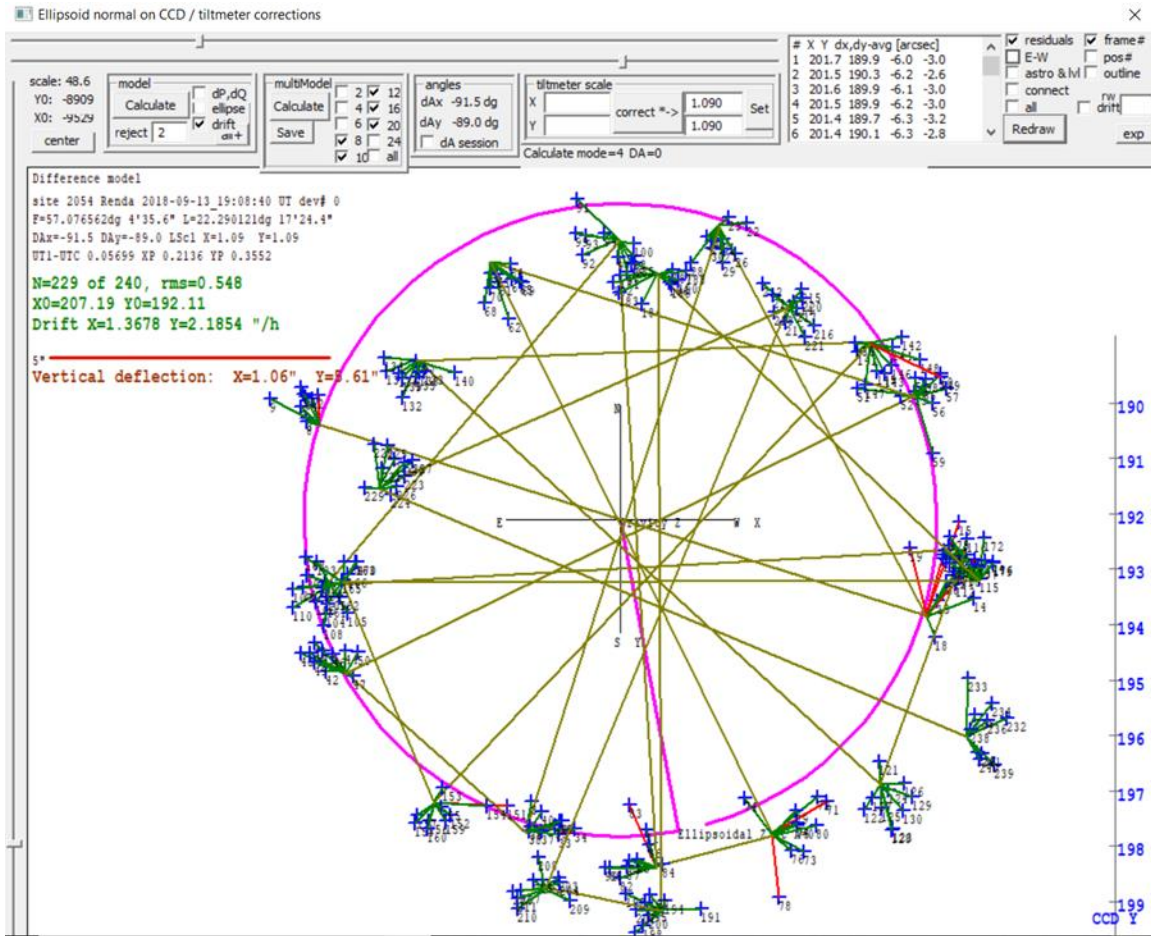
Figure 2.9. Model visualization and controls

The text block contains site and date information, used calibration constants, Earth rotation parameters, number of measurement points and model residual RMS, CCD coordinates of model center (place of plumb line projection at the time of the first position), drift values and estimated vertical deflection components.

Initially the graph is scaled and located so, that it fits in the area, available for painting. Sliders along upper and left edges of the window support changing scale and location of graph; "center" button places the graph close to window center. Parameters of screen coordinate system (scale in pixels per arc second, zero point in pixels) are shown in the upper left corner.

Controls of model calculation are located in the "model" groupbox. "Calculate" button repeats calculations (with drift option if "drift" checkbox is checked), using outlier rejection tolerance as specified in "reject" field. "+" button activates all rejected outliers.

## 2.7.        Data subset selection

The model (2.25 a, b) incorporates only that part of effects of several essential perturbations of measurement process (most notably, effect of anomalous refraction variability and thermal expansion effects in instrument construction), which can be described as linear dependency on time. Approximation of long sequences of measurements often show presence of unlinearity and other influences, manifesting as systematic trends in residuals and increase of residual RMS value. In order to outline effect of model inadequacy on vertical deflection estimates and, possibly, find out nature of these influences, approximation of various subsets of full session data have proved useful. Such approach is also efficient in identifying and isolating occasional measurement errors. Mechanism of subset selection is implemented using frame status flags. If a frame is currently active, it is marked with "+" in the first column of frame list (Figure 2.10).



Figure 2.10. Frame list dialog

Processing ("Model" button in Session dialog; "Calculate" buttons in Model dialog) uses only active frames. Controls for manipulating frame statuses are located in the "session results" groupbox:

- "-<" button makes all frames inactive;

- ">+"button makes all frames active;

- "N=0 ->-" button makes inactive all frames without astrometric or leveling solution;

- "-<>+" button reverses status of the selected frame (or selected position if "curr pos" is checked);

- ">+ frm/pos #" activates frames or positions within number interval, indicated in the fields to the right (initial #; number of frames/positions);

- "->" button moves the above interval ahead one step; it (and the previous as well) also invokes "Process" button.

## 2.8. Multi-model mode

In order to make analysis of different subsets of data more convenient, the multi-model calculation mode is implemented. In this mode models for a number of data subsets of different extent and time location are calculated. Results are presented as series of graphs (Figure 2.11), showing dependency of estimated vertical deflection components on subset parameters – number of included positions and represented time interval.
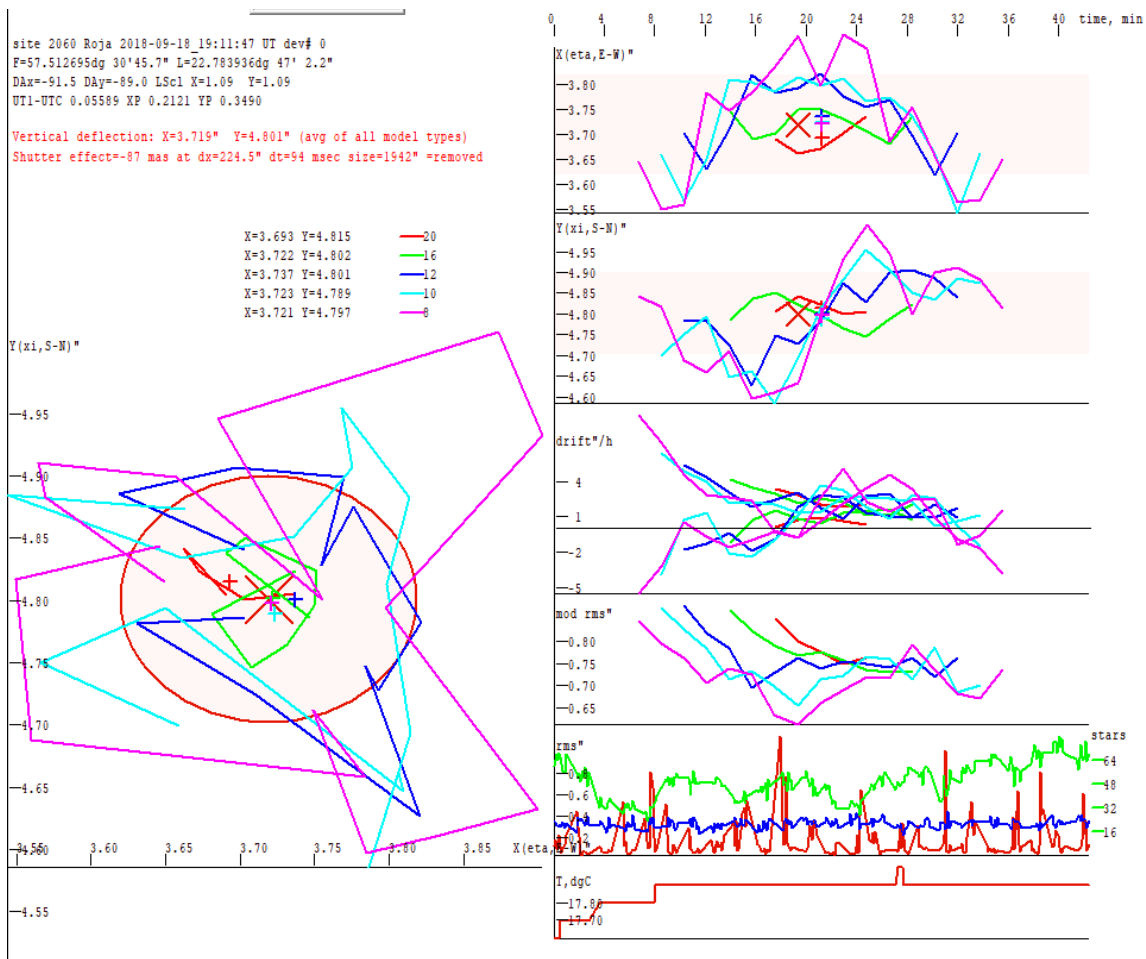


Figure 2.11. Visualisation of results

To complement the picture, also dependencies on time of drift estimates, approximation accuracy, source data accuracy, number of stars in frames and ambient temperature are shown.

Controls for multi-model mode in "multiModel" groupbox of Model dialog (Figure 2.12) consist of "Calculate" button and series of checkboxes for represented model sizes (number of represented consecutive positions).
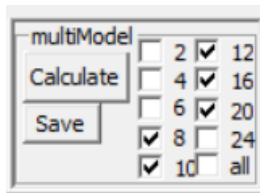


Figure 2.12. MultiModel dialog

For each requested size model parameters are calculated for a number of data subsets and visualized in specific color. Time moments are average for included positions, for smallest subsets they span almost all session duration while for largest – only middle interval; the subset, including all positions, is only one and is represented on graphs with one point.

On vertical deflection values graphs the area +/-0.1 arcsec around average is colored light-red. Except for cases of really big anomalous refraction variations, most of results for models with more than 6 positions should be inside that area.

All multiModel calculations are done using full model (2.25 a, b), including drift estimations. Duration of calculation depends on number of positions in session and selected set of model sizes, it can reach several seconds.

When interpreting the results, following considerations should be regarded:

• Small subsets are prone to big random fluctuations of model parameters, ranging up to ~arcsec for 2 positions;

• Random component decreases with more positions and longer time interval; systematic effects start to dominate typically at 8 positions (~15 minutes);

• Longer subsets show increasing of approximation errors due to unabsorbed systematic differences from model, mainly with non-linear drift and anomalous refraction origin.

• Value of drift often is big (tens of "/h) at the beginning of a session, especially, if instrument before session was stored at conditions, noticeably different from ambient. Drift rapidly decreases and after 10-20 minutes typically is down to a few "/h.

• Effect of variability of anomalous refraction on approximation errors is relatively small (~0.1 arcsec) and becomes noticeable only in conditions of low and stable drift.

• Variations of anomalous refraction have typical amplitude of up to 0.1-0.2" with periods of 0.5-2 hours, amplitude decreases for longer periods. Variability with shorted periods probably has bigger amplitudes, but it is difficult to estimate because of little number of measurement positions, each having systematic shift caused by variability with even shorter periods.

• Model accuracy starts to deteriorate if frame astrometric and/or leveling RMS increases above ~0.5 arcsec level. Possible reasons of that may be bad focusing, high microseismics level, wind, etc. Risk factor is also small (below ~10) number of stars per frame, especially if it is consequence of bad focusing quality.

• If attachment of some component of the instrument has become loose and some extent of free movement is present, measurement results can split into several subsets, each with own model (differient mainly in parameters $X_0, Y_0$). Indication of such situation is rejection of data for whole positions or solution with huge RMS and opposite directions of residuals for different positions.


## 2.9. Results of vertical deflection determination

A multitude of approximating models can be obtained from the results of an observation session, representing, besides vertical deflection value itself, also behavior of anomalous refraction and thermal expansion of instrument components during session. Which of these models is the best representation of actual vertical deflection value, is a matter of some assumptions and speculations. Presently it seems, that, although thermal drift increases the value of model residuals, it is fairly well averaged across session and do not contribute much in systematic shift. The main concern is about variations of anomalous refraction, causing apparent time dependency of estimated vertical deflection values. Typically oscillations with period around one hour and amplitude of 0.1-0.2 arcsec are found. Observations, covering at least half of that period are needed for averaging. Even then, shift of average value for up to about half-amplitude is possible. Therefore, we consider that ~0.1 arcsec accuracy for this kind of vertical deflection measurements with short (an hour or less) observation time is a reasonable estimation, even if formal dispersion of results is smaller. Longer sessions can reveal behavior of anomalous refraction more fully, possibly giving several times more accurate vertical deflection estimates. However, possibility of presence of anomalous refraction effects of very long period (e.g., seasonal) or even permanent nature, cannot be ruled out.

In order to obtain on the basis of an observation session data a reliable estimation of vertical deflection, average values for models of all sizes, included in multiModel mode are calculated. On the results graphs, these values are marked with crosses of corresponding color. Finally, an average of averages is calculated, marked on graphs with a bigger, slanted red cross, and component values of it shown above XY graph. Also a list of average component values for all model sizes is shown, along with variability (half of max-min).

When "Save" button in multiModel groupbox of Model dialog is pushed, a text line with results of current calculations (average of averages in case of multiModel mode) in format:

```
#=Kolka_#1 DATE=2019-09-18_21:44 F=57.751164 L=22.595641 H=25.3  ZX= 3.377 ZY= 1.804 ERR=0.10
```
 is added to file.

The time corresponds to the first frame of the session. Site coordinates are those, which were present in session information file (unless changes were made after reading it). Error estimate is fixed at 0.1 arcsec and should be changed manually if that is deemed necessary.


## 2.10.     Calibration session

A special observation session is needed to determine instrument calibration constants: orientation of tiltmeter axes relative to CCD and scale of tiltmeter readings. For that purpose, star observation are performed in a number of instrument leveling positions along trajectories, close to tiltmeter axes, so that readings of one axe are changing as little as possible in the process. In this way, tilt change along the other axis can be compared with zenith point projection trajectory on CCD, and both relative axes orientation and scale factor calculated.

In order to calculate movements of leveling actuators for such trajectory, approximate orientation of tiltmeter A1 is necessary (Figure 2.13). It is supplied in configuration constant Az #1: orientation of the 1$^{st}$ actuator radius relative to tiltmeter X (radial) axis. To keep readings of one axis constant, actuator positions should be proportional to: $cos \cdot (A1 + 120° \cdot (i - 1))$ for x and $sin \cdot (A1 + 120° \cdot (i - 1))$ for y, where $i$ – number of actuator.
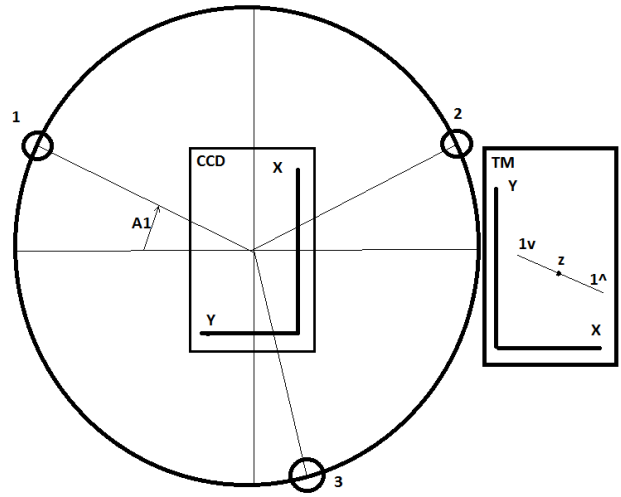
Figure 2.13. Scheme of actuators
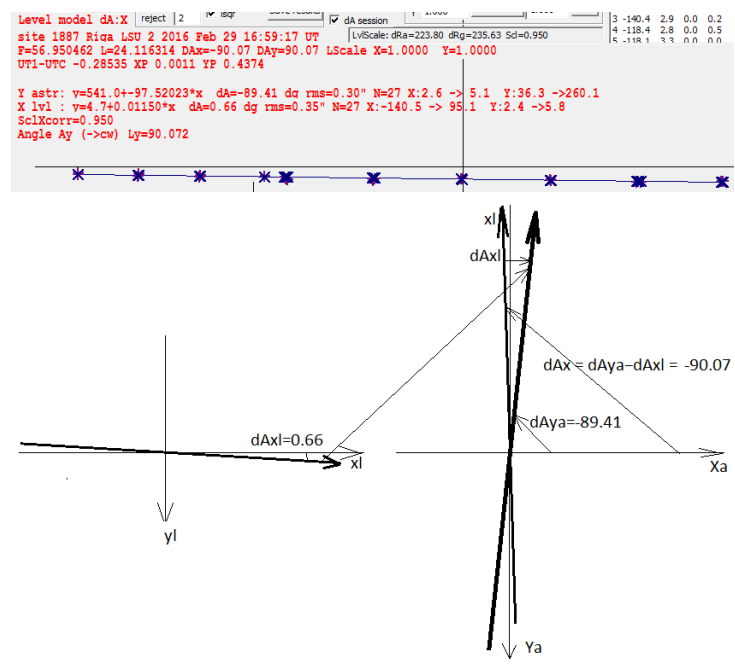


Figure 2.14. Tiltmeter close to X axis (xl); zenith close to CCD Y axis (Ya). Coordinate system of tiltmeter is left-handed. Trajectory of tiltmeter zero is matched with trajectory of zenith.

Calibration observation session is performed starting from leveled position. As the first step actuators are moved along the selected tiltmeter channel almost to the limit of tiltmeter range. Then a series of observation positions are visited moving back along the same trajectory, until tilt is close to the opposite end of tiltmeter range. Scenario of such sesssion must contain symbols DA_X or DA_Y; what in normal scenario is rotation angle, is here interpreted as tilt step (in arc seconds).

48

Processing of DA session results includes calculation of zenith point CCD coordinates and tiltmeter corrections just like for any other sessions. After that, however, process is quite different. Session data must be processed first in "astro" mode, calculating parameters of zenith trajectory on CCD, then in "level" mode, calculating parameters of tilt trajectory. When both trajectories are got, relative angle between them and tiltmeter scale factor is calculated.

The result of processing of DA session are parameters of line $Y = Y_0 + k \cdot X$, approximating trajectory of zenith projection or tiltmeter zero-point. Formula $tg(dA) = k$ gives angle $dA$ of this line to X axis. When these angles for both zenith and tiltmeter zero are obtained they must be combined so, that trajectories coincide, to get relative orientation of CCD and tiltmeter. Figure 2.15 illustrates the geometrical disposition; perpendicularity of respective axes and mixing of right and left coordinate systems can make the process a little confusing.
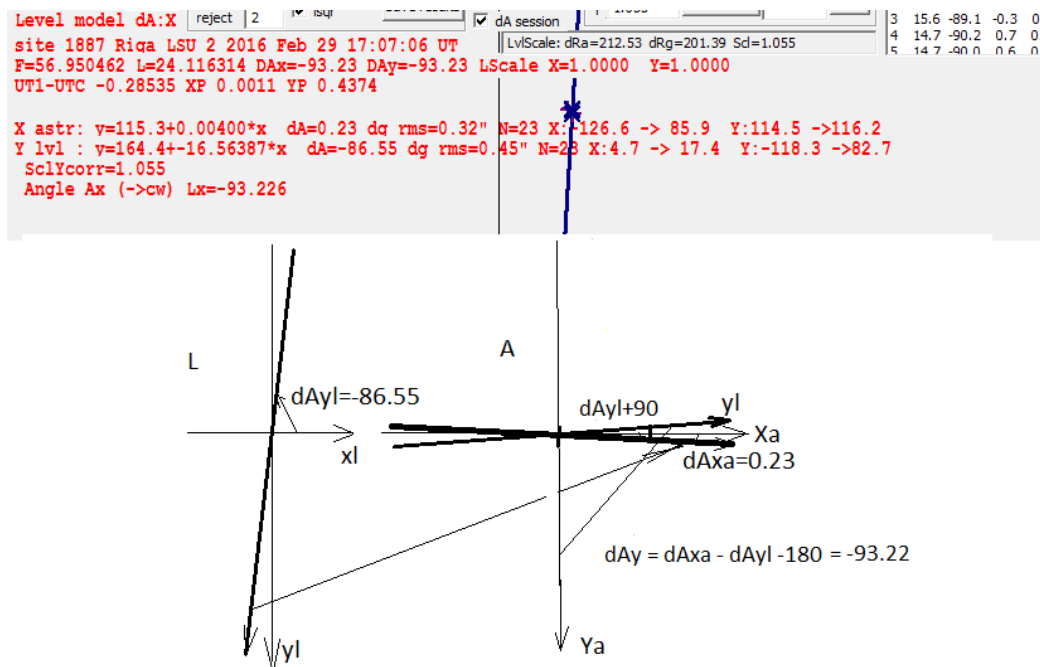


Figure 2.15. Trajectory of tiltmeter close to yl axis (direction negative); trajectory of zenith close to Xa axis.

The result of calibration calculations are two orientation angles between respective axes of CCD and tiltmeter. Due to inaccuracies in tiltmeter axes direction adjustment, difference between them can reach several dg. Other result is tiltmeter scale, it may quite noticeably (up to ~10%) differ from passport value, possibly can depend on time and/or other external factors, like ambient temperature, humidity, pressure, voltage of power source. Due to this, it is desirable to perform

measurements as close to the tiltmeter zero-point (or any other fixed value), as possible, avoiding scale or orientation error transfer to tilt corrections in coordinate transformation (2.24 a, b). Resulting angles and scales must be entered in configuration data in order to be saved in session information file for subsequent sessions. At processing of a session, values, stored in that file are used. However, if necessary, they can be edited in Session dialog (angles) and Model dialog (scale). Modified values will be used in subsequent calculations and written to session information file, if it is saved.

## 2.11.     The use of vertical deflections in Riga region

In case of the DFHRS software v. 4.3 the height reference surface is modelled by mesh-wise ($i=$ mesh index), but overall continuous polynomials $p_i$. So, we have (*Jäger, 2010*):

$$N_i = [1|B, L|B^2, BL, L^2|B^3, B^2L, BL^2, L^3|..] \cdot$$
$$[p_{00}|p_{10}, p_{01}|p_{20}, p_{11}, p_{02}|p_{30}, p_{21}, p_{12}, p_{03}]_i^T = f(B, L)^T \cdot p_i \qquad (2.26)$$

In (2.26) the parameters (B, L) mean the ellipsoidal latitude and longitude at position P. Considering that in case of computing a quasi-geoid ($N_{QG}$), we have to use surface vertical deflections instead of the Helmert type. These are related - according to the Molodensky theory - to the so-called Telluroid point $Q_j$, which is in a height $h_{Q,j} = h_{P,j} - N_{QG,j}$ below the surface point $P_j$. For the *j*-th couple of vertical deflections measured in the *i*-th mesh, we arrive at the the following observation equations:

$$\xi_{j,i} = -\frac{\partial N_{QG}}{\partial B_j} \cdot \frac{\partial B_j}{\partial S_N} = -\frac{\partial B_j}{\partial S} \cdot \frac{\partial N_{QG}}{\partial Bj} = \frac{-1}{(M_j + h_j)} \cdot f_{B_j}^T \cdot p_i \qquad (2.27a)$$

$$\eta_{i,j} = -\frac{\partial L_j}{\partial S} \cdot \frac{\partial N_{QG}}{\partial L_j} = \frac{-1}{(N_j + h_j) \cdot cosB_j} \cdot f_{L_j}^T \cdot p_i \qquad (2.27b)$$

*M* and *N* mean the radius of the curvature of the ellipsoid to the direction of the meridian and the prime vertical, respectively.

The Riga region was chosen as test area and includes 35 GNSS /levelling points (h,H) and 10 deflections of the vertical data points (η,ξ) observed by the developed digital zenith camera. The GNSS observations were partially provided by Latvian Geospatial Information Agency, as well as being carried out in 4 hours sessions and processed using Bernese GNSS software v 5.2

(*Dach et al., 2015*) as fiducial stations using the EUREF Permanent Network (EPN) stations (*Haritonova et al., 2015*) The postprocessed results were transformed to epoch 2017.0 using Helmert transformation (*Balodis, et al., 2017*). Besides field data observations from the developed zenith camera and GNSS/levelling points, quasi-geoid data N and vertical deflections data ($\eta,\xi$) were derived from EGM2008 (*Pavlis et al., 2008a; Pavlis et al., 2008b, Pavlis et al., 2012*) and EIGEN6C4 (*Förste et al., 2014; Kostelecky et al., 2014*) geopotential models http://icgem.gfz-potsdam.de/ICGEM/ (*Ince et al., 2019)* Both models are of the same degree and order n=m=2159. The graphical display of the polynomial mesh (thin blue lines) and patch design (thick blue lines) and the observed data (fitting points and deflections of the vertical) of the DFHRS software 4.3 are depicted in Figure 2.16.
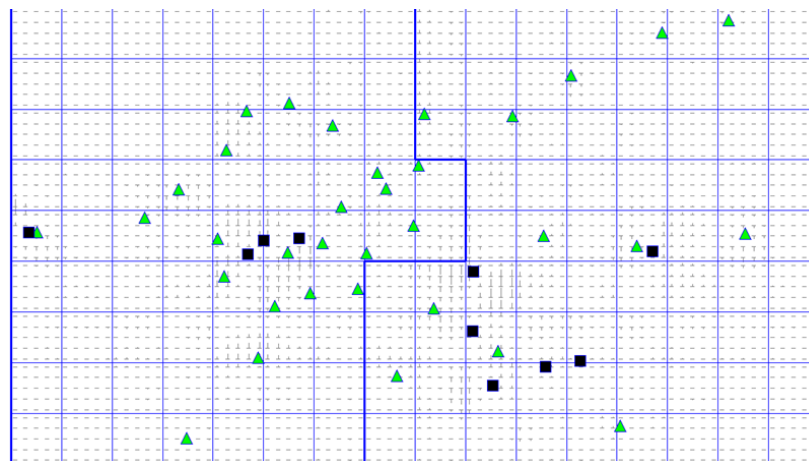


Figure 2.16. Riga region observations (green triangles – GNSS/levelling points, black squares – deflections of the vertical).

Different computation results are depicted in Figure 2.17, Figure 2.18 and Figure 2.19. Figure 2.17 shows the difference of the quasi-geoid models N based on EGM2008 and EIGEN6C4 geopotential models. In most parts of Riga region, the amplitude of difference in geoid heights is in range from -1 up to +1 cm. The difference in the north of Riga region can reach up to 3 cm. The Figure 2.18 depicts the use of deflections of vertical data derived from EGM2008 model and its impact on geoid heights determination. This difference can reach from -3 up to +3 cm. Figure 2.19 shows the differences of deflections of vertical observations from digital zenith camera in comparison without using this data. The range of differences varies from -7 up to +5 cm, what proves significant impact of the use of deflections of the vertical (*η, ξ*) on a quasi-geoid

determination. The standard deviation of the deflections of vertical data is equal to 0.09 arcsec for ξ (North- South) component and 0,14 arcsec for η (East-West) component. Other statistics is performed in Table 1.

Table 1

Statistics of vertical deflections observations (arcsec).

|   | Mean | RMS | Min | Max |
|---|------|-----|-----|-----|
| ξ | 0.072 | 0.09 | -0.100 | 0.162 |
| η | 0.091 | 0.14 | -0.311 | 0.226 |

The calculations based on the preliminary results of vertical deflections observations approve the successful use of digital zenith camera and instrument readiness for further collection of observations. The computations using the DFHRS software v.4.3 allowed to carry out additional control and software's check for modelling and data errors in the frame of the data processing.
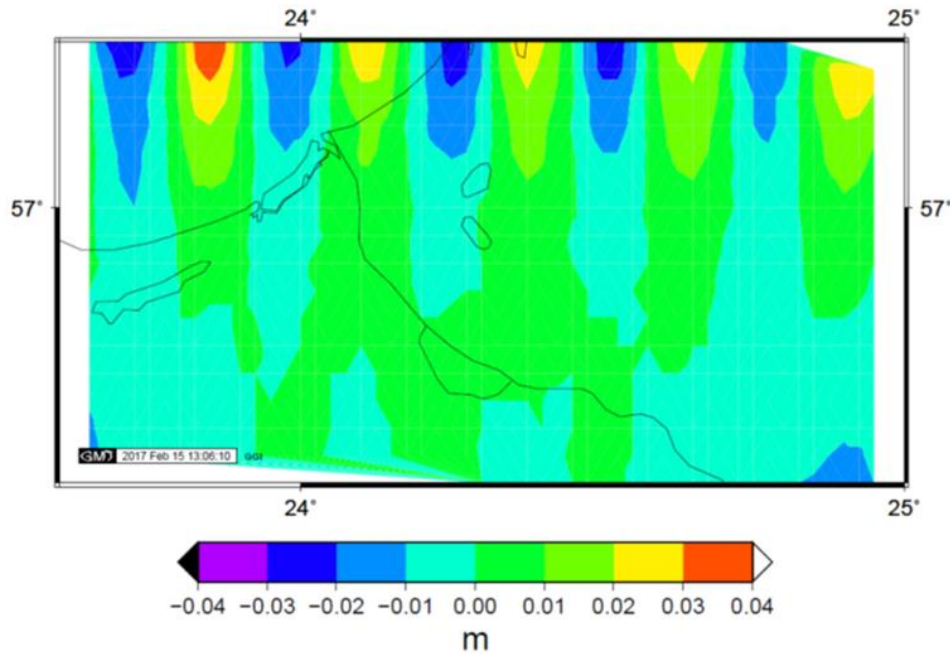


Figure 2.17. The difference of quasi-geoid model for Riga region in comparison to EIGEN6C4 and EGM2008 geopotential models.
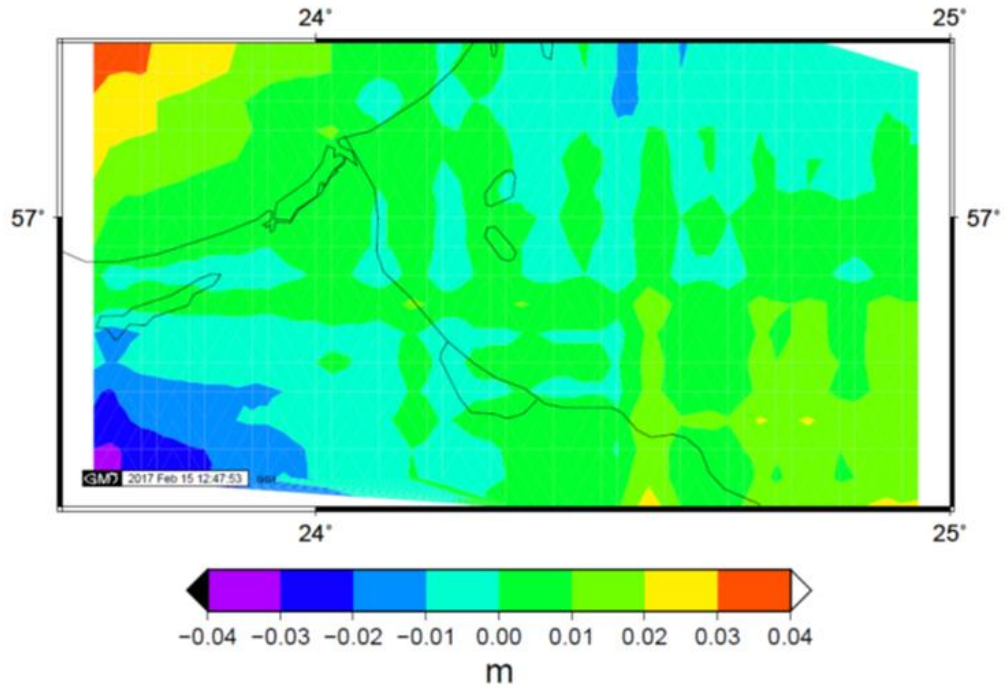
Figure 2.18. The difference between using derived deflections of vertical data and without this data.
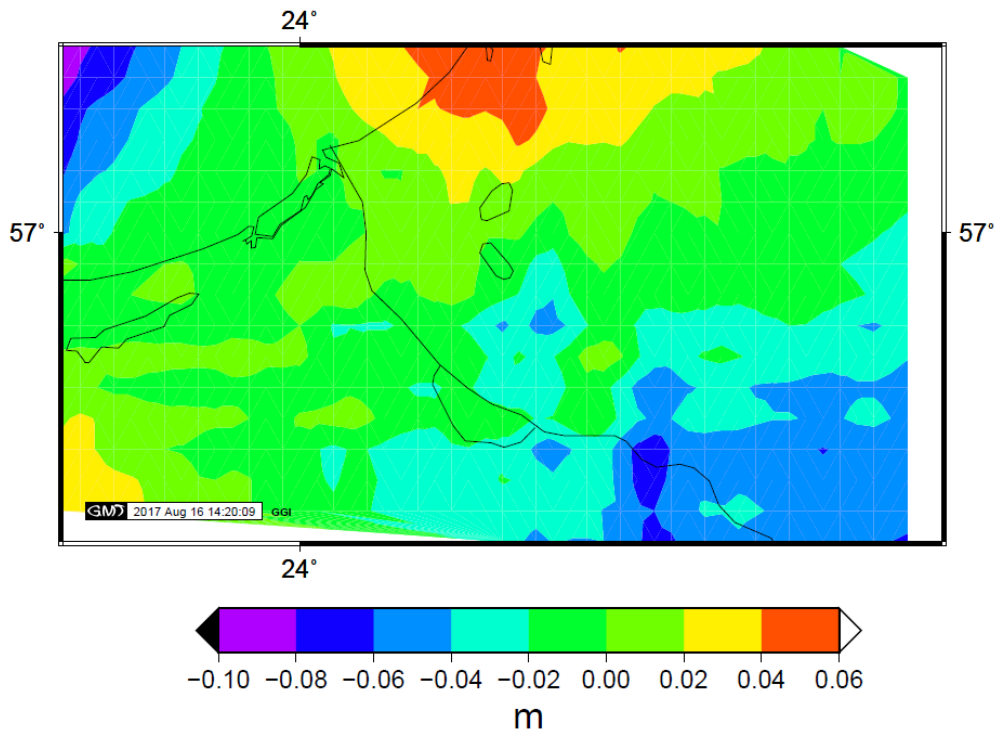


Figure 2.19. The impact of vertical deflections data from digital zenith camera.

The residuals of standard deviations are depicted in Table 2. As it is seen from the Table 2 the difference of the solutions is equal to 0.0001 m if we compare the results computed using EGM2008 model and EIGEN6C4 model. It can be explained by the fact that the same terrestrial data for these models were used in the territory of Latvia. The use of vertical deflection observations from digital zenith camera improves standard deviation twice. This shows favourable tendency for quasi-geoid improvement and also sustainability of digital zenith camera.

Table 2

Different solutions for Riga region quasi-geoid

| Used data | Standard deviation (m) |
|-----------|------------------------|
| **EGM2008 model + observations from digital zenith camera** | 0.0050 |
| **EGM2008 model** | 0.0109 |
| **EIGEN6C4 model** | 0.0110 |
| **EGM2008 model with derived vertical deflections** | 0.0127 |

The residuals of some vertical deflection measurements are depicted in Table 3.

Table 3

The values of VD and its residuals.

| Point number | $\xi('')$ | $\varepsilon(\xi'')$ |
|--------------|-----------|----------------------|
|              | $\eta('')$ | $\varepsilon(\eta'')$ |
| **Riga** | 1.40 | -0.060 |
|          | 5.60 | -0.086 |
| **Daug** | -0.45 | 0.075 |
|          | 6.30 | 0.226 |
| **Iks1** | -1.40 | -0.100 |
|          | 5.00 | -0.014 |
| **Iks2** | -1.15 | 0.029 |

|      |       |        |
| :--- | ----: | -----: |
|      | 5.15  | -0.009 |
| **Luni** | 1.80  | 0.162  |
|      | 6.30  | -0.311 |
| **Kang** | -0.40 | -0.016 |
|      | 6.72  | 0.059  |
| **Ceku** | -1.72 | -0.094 |
|      | 6.55  | 0.108  |
| **Salp** | -1.18 | -0.087 |
|      | 5.88  | 0.011  |
| **Vaiv** | 2.90  | 0.042  |
|      | 8.20  | -0.022 |
| **Zalv** | 1.55  | 0.053  |
|      | 6.20  | -0.059 |

The mean standard deviation after estimation is found to be about 0.11". The observations from digital zenith camera were continued in order to cover whole territory of Latvia and all "suspicious" places were checked and are discussed in the further chapter of this PhD thesis.

# 3. METHODS FOR QUASI-GEOID DETERMINATION

In this chapter several methods of quasi-geoid determination are introduced, as well as stages of development of DFHRS software, as well as new method of DFHRS including both vertical deflections and gravity measurements. Examples of quasi-geoid determination for Ulaanbaatar and Riga cities are introduced and the obtained results are performed. In order to compare the performed method of DFHRS and "classical" method performed by GRAVSOFT Riga region has been chosen and the results are introduced.

## 3.1. Geoid determination by DFHRS v 4.3.

DFHRS (Digital Finite element Height reference surface (HRS)) v4.3. software has been developed by Karlsruhe University, Institute of Applied Research. It is based on parametric modeling of the HRS as a continuous polynomial surface. The access to the parametric HRS model is enabled by DFHRS_DB data-bases and access-software, which allow direct conversion of GNSS-heights h into physical normal heights H. DFHBF_DB stores HRS polynomial parameters **p** and the scale difference ($p, \Delta m$) together with the mesh-design information. The principle of a GNSS-based height determination $H$ requires submitting the GNSS-height $h$ to the DFHRS ($B, L, h$)-correction $N$, reading *(Jäger, 2000-2022):*

$$H=h-N=h-DFHRS\ (p|B,\ L,\ h)\ =h-NFEM\ (p|B,\ L,\ h) \tag{3.1}$$
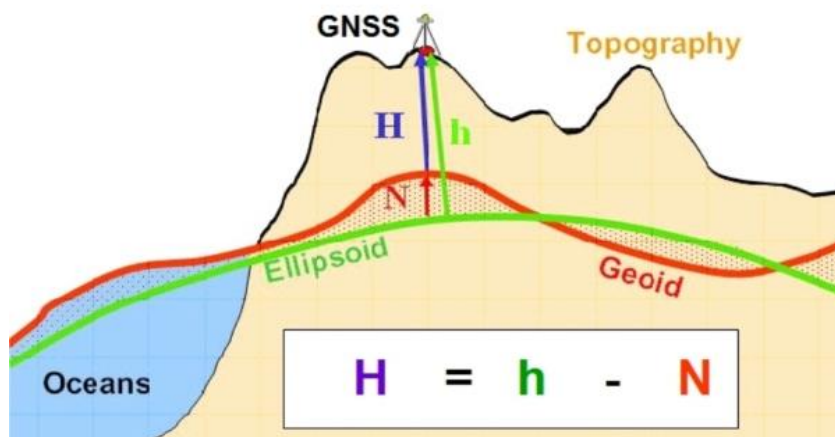


Figure 3.1. The principle of GNSS-based height determination (*Jäger, 2000-2022)*

The mathematical model for observation groups in a common least squares computation (Gauß-Markov-Model) for the evaluation of the DFHRS_DB parameters $p$ and $\Delta m$ is given by formulas (3.2 – 3.5) *(Jäger, 2000-2022; Jäger et al., 2012, Schneid, 2006))* where functional model for uncorrelated ellipsoidal heights $h$:

$$h = v = H + h \cdot \Delta m + NFEM(p|x,y) \tag{3.2}$$

with $NFEM(p|x,y) =: \mathbf{f}(x,y)^T \cdot \mathbf{p}$.

Functional model for correlated geoid height observations:

$$N_G(B,L)^j + v = \mathbf{f}(x,y)^T \cdot \mathbf{p} + \partial N_G(\mathbf{d}^j) \tag{3.3}$$

With a given real covariance matrix $C_{N_G}$ or $C_{N_G}$ evaluated from a synthetic covariance function.

Functional model for correlated observations of deflections from the vertical $(\xi, \eta)$.

$$\xi^j + v = \frac{-\mathbf{f}_B^T}{M(B) + h} \cdot \mathbf{p} + \partial\xi\left(\mathbf{d}_{\xi,\eta}^j\right) \tag{3.4a}$$

$$\eta^j + v = \frac{-\mathbf{f}_L^T}{(N(B) + h) \cdot \cos(B)} \cdot \mathbf{p} + \partial\eta(\mathbf{d}_{\xi,\eta}^j) \tag{3.4b}$$

Pairwise correlated or uncorrelated in case of astronomical observations. Correlated if derived from a gravity potential model.

Uncorrelated standard height $H$ observations:

$$H + v = H \tag{3.5}$$

with covariance matrix:

$$C_H = diag\left(\sigma_{H_i}^2\right) \tag{3.6}$$

Continuity condition equations introduced as uncorrelated so-called pseudo observations with accordingly small variances and high weights:

$$C + v = C(\mathbf{p}) \tag{3.7}$$

With $\mathbf{f}_B$ and $\mathbf{f}_L$ we introduce the partial derivatives of $\mathbf{f}(x(B, L), y(B, L))$ (3.4 a, b) with respect to the geographical coordinates $B$ and $L$. $M(B)$ and $N(B)$ mean the radius of meridian and normal curvature at a latitude $B$. The continuity of the resulting HRS representation $NFEM(\mathbf{p}|x,y) = \mathbf{f}(x,y)^T \cdot \mathbf{p}$ over the meshes (Figure 3.2, thin blue lines) is automatically provided by the

continuity equations $\mathbf{C}(\mathbf{p})$ (3.7). A number of identical fitting-points ($B, L, h; H$) are introduced by the observation equations (3.2) and (3.5) (Figure 3.2, green triangles). In the practice of DFHRS_DB evaluation, one or a number of different geoid-/GPM such as the EGG97 or EGM2008 are used in a least squares estimation related to the mathematical model (3.2 – 3.7), which is implemented in the DFHRS-software 4.4. To reduce the effect of medium- or long-wave systematic shape deflections, namely the natural and stochastic "weak-shapes", in the observations $N$ and ($\xi, \eta$) from geoid- or GPM models, these observations are subdivided into a number of patches (Figure 3.2, thick blue lines). These patches are related to a set of individual parameters, which are introduced by the datum parameterizations $\partial N_G(\mathbf{d}^j)$ (3.3) and $\partial\xi(\mathbf{d}^j{}_{\xi,\eta})$; $\partial\eta(\boldsymbol{d}^j{}_{\xi,\eta})$ (3.4 a, b). In this way, it is of course possible to introduce geoid height observations and vertical deflections from any number of different geoid- or GPM models in the same area, or observed vertical deflections (*Jäger, 2000-2022; Jäger et al., 2012*).

Continuity conditions should also be considered, boundaries between two meshes should be the same, so that meshes represent the whole continuous area (*Younis, 2013*). DFHRS v4.3 includes all types of geometrical input data: both ellipsoidal and normal/orthometric heights, geoid/quasi-geoid heights, vertical deflections, derived from Earth Gravity Model (EGM2008) or grids, and observed vertical deflection measurements from digital zenith camera, as well as gravity data derived e.g. from EGM2008.

As an example, in order to compute the DFHRS_DB for Ulaanbaatar 94 Identical points (ellipsoidal heights h and normal heights H in Baltic Height system) together with the EGM2008 geopotential model data were used. EGM2008 is a spherical harmonic model of the earth's external gravitational potential in degree and order of 2160, with additional spherical harmonic coefficients extending up to degree of 2190 and order of 2160 that offers a spatial resolution of 9 km. EGM2008 incorporates improved 5x5 min gravity anomalies, altimetry-derived gravity anomalies and has benefited from the latest GRACE based satellite solutions (*Pavlis et al., 2008a; Pavlis et al., 2008b).*
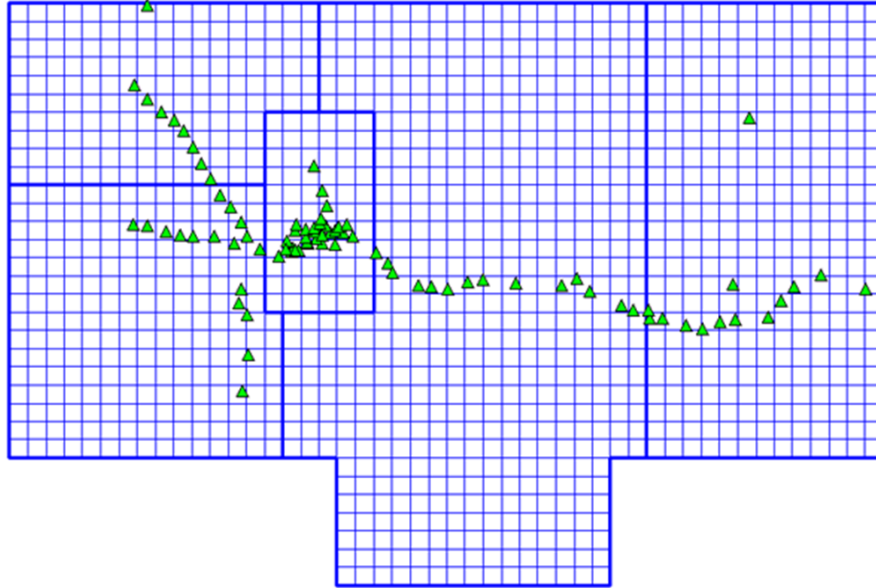
Figure 3.2. Computation design of DFHRS (meshes – thin blue lines, patches – thick blue lines, fitting points – green triangles)

For meshing the area, mesh size of 5x5 km was chosen. Total amount of meshes – 1536. The total number of patches is 5 (Figure 3.2). One patch must contain at least 4 fitting points. As points of the region are not homogenously located, patches, were not introduced in approximately the same size, but according to the location of the points. As geoid datum 3 translations and 3 rotations were introduced, additionally derived deflections of the vertical from the EGM2008 model were used.

The identical points and the EGM2008 geoid undulations were introduced together with the continuity conditions into a least squares estimation of the so-called "DFHRS production". The calculation has been done using the DFHRS v. 4.4 software. 88 normal height points H of the Baltic heights system could be used and were confirmed in the statistical testing (data-snooping) with the assumed standard deviation of 1 cm. 6 points – 4039, 216, 230, 5051, 509 and 22 were excluded from the computations because of gross errors. For 4 points (270, 1710, 1757 and GR70/70) the normal heights H were changed in comparison to the previous data package provided in 2017, the normal height for one point (1682) was used from previous data package. The partial adjustment protocol of the DFHRS-software 4.4 with the observation residuals, statistical testing of the height fitting points is depicted in Figure 3.3. (*Morozova et al., 2018*).

```
Characteristics:
  EV:     Redundancy factor
  NV:     Normalized residuals, test size a priori
  t_post: Test size a posteriori
  GF:     Estimated gross error is issued in case of exceeding
          the critical value by NV, bzw. T_post.
 Probability of error Alpha: 5 %
 Critical value a priori:       3.841552  degrees of freedom:  infinity
 Critical value a posteriori:   3.841549  degrees of freedom:    102887
```

| Point number | Height/Target sys. [m] | Res. [m] | EV [%] | NV | t_post | REPRO |
|---|---|---|---|---|---|---|
| 137 | 1168.601 | 0.00009 | 18.88 | 0.0 | 0.5 | -0.001 |
| 253 | 1441.619 | 0.00449 | 22.69 | 1.3 | 22.2 | -0.020 |
| 268 | 1459.774 | -0.00176 | 21.66 | 0.5 | 8.9 | 0.008 |
| 282 | 1318.717 | -0.00275 | 19.97 | 0.9 | 14.5 | 0.014 |
| 505 | 1433.682 | -0.00366 | 22.85 | 1.1 | 18.0 | 0.016 |
| 1598 | 1418.122 | 0.00106 | 16.46 | 0.4 | 6.1 | -0.006 |
| 1710 | 1478.901 | 0.00345 | 22.20 | 1.0 | 17.3 | -0.016 |
| 1731 | 1608.961 | 0.00347 | 20.96 | 1.1 | 17.9 | -0.017 |
| 1747 | 1313.276 | -0.00114 | 23.60 | 0.3 | 5.5 | 0.005 |
| 1757 | 1220.986 | 0.00231 | 20.85 | 0.7 | 11.9 | -0.011 |
| 2324 | 1263.574 | -0.00330 | 23.20 | 1.0 | 16.1 | 0.014 |
| 2329 | 1246.173 | -0.00198 | 23.35 | 0.6 | 9.6 | 0.008 |
| 4750 | 1456.719 | -0.00098 | 21.87 | 0.3 | 4.9 | 0.004 |
| 5006 | 1419.172 | 0.00655 | 23.67 | 1.9 | 31.8 | -0.028 |
| 5019 | 1425.403 | 0.00617 | 23.32 | 1.8 | 30.2 | -0.026 |

Figure 3.3. Final DFHRS software adjustment protocol at the example of Ulaanbaatar

The present DFHRS was calculated on the basis of the EGM2008 geoid and 88 identical reference points. The accuracy of the identical points was confirmed with 1.0 cm, so the geoid of the Ulaanbaatar region has an estimated 1-3 cm accuracy within the area of the outer ring polygon-line of the fitting-points. The DFHRS_DB can be used by the software DFHBF-Tools to compute the geoid height *N*, and so the normal heights *H* from the input of a 3D GNSS-position (*B, L, h*) or (*X, Y, Z*), and in order to set up a respective geoid 2018 grid for the Baltic Height System (BHS-77) in the Ulaanbaatar Region. Especially for the borders of the Region (Figure 3.2) additional vertical deflection observations made by digital zenith camera (*Zarins et al., 2016*), (*Morozova et al., 2017*) are recommended. In that way, the 1-3 cm accuracy will hold for the whole area.

## 3.2. Geoid determination by DFHRS v. 5.0

The DFHRS software 5.0 can process in addition also gravity observations. The mathematical model of the integrated adjustment approach of the DFHRS software, version 5.0 parameterizes the gravity potential W in a regional Spherical Cap Harmonic (SCH) representation, namely by the SCH-coefficients ($C'_{nm}, S'_{nm}$). As observation data the input the coefficients ($C_{nm}, S_{nm}$) of a

global geopotential model (GGM), such as e.g. EGM2008 can be used, which are mapped to regional SCHA-coefficients $(C'_{nm}, S'_{nm})$ (*Younis et al., 2011*). Further observations of the least squares adjustment with the parameters $\mathbf{p} = (C'_{nm}, S'_{nm})$ are observed gravity values $g(B, L, h)$, vertical deflection observations $(\xi, \eta)$, e.g. from zenith-cameras, and identical points $(B, L, h / H)$. The HRS results from the computed SHA parameters $\mathbf{p} = (C'_{nm}, S'_{nm})$ and $\mathrm{W}(C'_{nm}, S'_{nm})$, respectively basically by the theorem of Bruns, namely as quasi-geoid. Quasi-geoid can be further evaluated to a geoid N model. The results of quasi-geoid heights and geoid heights can be mapped again to the HRS, which is represented by the above polynomial parameters $\mathbf{p}$ or by a traditional HRS Grid.



Figure 3.4. Scintrex CG-6 relative gravimeter *(author)*

The extension of DFHRS concept and software to physical observation types – such as terrestrial, air- or space-borne gravity measurements (for terrestrial gravity meter see Figure 3.4), or physical observation types taken from geopotential models, e.g. EGM2008 – is based on a regional spherical cap harmonic parameterization (SCH) of the Earth's gravitational potential (V). The benefit of an SCH-parameterization (3.8) with a local cap pole and a limited cap size area, instead of an ordinary global spherical harmonic (SH), is that the same resolution of V can be achieved

with SCH by a much smaller number of parameters than with SH. Thus, for a 2 mm resolution for the HRS, a degree of 7200 for the SH parameterization by $(C_{nm}, S_{nm})$ is required, while for a cap size area of 100 km a degree of only $k_{max}$=80 is enough in the case of an SCH parametric model. Therefore, SCH is the key model for enabling the computation of high resolution HRS in the 2nd stage of the DFHRS research and development, meaning an integrated over-determined HRS-computation for all types of geometrical and physical observations. The representation of gravitational potential V of the Earth in terms of SCH with parameters $(C'_{n(k),m}, S'_{n(k),m})$ reads:

$$
\begin{aligned}
V(r,\lambda',\theta') = \sum_{k=0}^{k\ max} (\frac{a}{r})^{n(k)+1} \sum_{m=0}^{k} (C'_{n(k),m} \cdot cosm\lambda' + S'_{n(k),m} \cdot sinm\lambda') \\
\cdot P'_{n(k),m}(cos\theta')
\end{aligned}
\tag{3.8}
$$

Here the space position refers to the triple of spherical cap coordinates $(r, \lambda', \theta')$. In the following, the observation equation for terrestrial and air- or space-borne gravity observations $g_p$ is briefly worked out.

The gravity observation $g_p$ at the Earth surface point P (taken with a gravity meter, see (Figure 3.4) is referring to the local astronomical vertical (LAV) system, and, therefore, for the respective observed 3D gravity vector we have in total:

$$
\mathbf{g}^{LAV} = [0, 0, -g_P]^T
\tag{3.9}
$$

– Original gravity observation and vector.

The astronomical vertical $(\Phi=B+\xi, \Lambda=L+\frac{\eta}{\cos(B)})$ is set up by the ellipsoidal vertical $(B, L)$ and the deflections – from the vertical $(\xi, \eta)$. The original vector $g^{LAV}$ (3.9) is first rotated to the Earth-centered Earth-fixed system (ECEF) using the astronomical direction $(\Phi, \Lambda)$ from a geopotential model. In that coordinate frame, the centrifugal part of $\mathbf{g}^{LAV}$ (3.9) is removed.

$$
g_{rot}^{LGV} = [g_N, g_E, g_r]^T
\tag{3.10}
$$

The observation vector $g_{rot}^{LGV}$ (3.10) is then further rotated in 3 components of the sphere as $g_{grav}^{SCH}$ to the SCH-representation frame (3.8). The SCH-related representation of the gravity vector (3.10) reads:

$$g_{grav}^{SCH} = [\frac{1}{r} \cdot \frac{\partial V}{\partial \theta'}, \frac{1}{r \cdot sin\theta'} \cdot \frac{\partial V}{\partial \lambda}, \frac{\partial V}{\partial r}]^T \tag{3.11}$$

The principal component of the rotated observed gravity observation $g_{rot}^{LGV}$ (3.10) is related to the third component of (3.11), and the accuracy of the vertical component of the SCH-transformed observation vector (3.10) is nearly unaffected. So, in the so-called integrated DFHRS approach we have the following observation equation for a gravity observation:

$$g_{grav_r}^{SCH} + v_g = \frac{GM}{r^2} \cdot \sum_{k=0}^{k\,max} \left(\frac{a}{r}\right)^{n(k)+1} (n(k) + 1) \cdot \sum_{m=0}^{k}(C'_{n(k),m} \cdot cosm\lambda' + $$
$$+S'_{n(k),m} \cdot sinm\lambda') \cdot P'_{n(k),m}(cos\theta') \tag{3.12}$$

With $v_g$ (3.12) we describe the observation correction of the gravity observation in the integrated adjustment approach. By introducing the disturbance potential:

$$T_P = (V(\hat{C}'_{n(k),m}, \hat{S}'_{n(k),m}) - V_{ref})_P \tag{3.13}$$

applied to the Bruns theorem and Molodensky's theory, we obtain the observation equation for fitting-points $(h - H)$ converted to quasi-geoid heights (see 3.14) and vertical deflections $(\xi, \eta)_P$ (3.15 a, b) observed at point $P$ as:

$$h - H_{Normal} = N_{QG} = \frac{(V - V_{ref})_P}{\gamma_Q} = \frac{T_P}{\gamma_Q} \tag{3.14}$$

$$\xi = -\frac{\partial N_{QG}}{\partial B} \cdot \frac{\partial B}{\partial S_N} = -\frac{\partial B}{\partial S} \cdot \frac{\partial N_{QG}}{\partial B} = \frac{-1}{(M+h)} \cdot \frac{1}{\gamma_Q} \cdot \frac{\partial}{\partial B} T_P = \frac{-1}{\gamma_Q \cdot (M+h)} \cdot (\frac{\partial T}{\partial B})_P + $$
$$\delta\xi_{norm.curv.} \tag{3.15a}$$

$$\eta = -\frac{\partial L}{\partial S} \cdot \frac{\partial N_{QG}}{\partial L} = \frac{-1}{(N+h) \cdot cosB} \cdot \frac{1}{\gamma_Q} \cdot \frac{\partial}{\partial L} T_P = \frac{-1}{\gamma_Q \cdot (N+h) \cdot cosB} \cdot (\frac{\partial T}{\partial L})_P \tag{3.15b}$$

$\delta\xi_{norm.curv.}$ is the difference between between the ellipsoidal normal and the tangential vector to the normal gravity vector $\bar{\gamma}$ grad *(U)* at a point P and $\gamma_{Q_j}$ is the ellipsoidal normal gravity value for the point Q, the so called telluroid point, associated to P by the same latitude and longitude and an ellipsoidal height $h_Q = h_P - N_{QG}$, see Figure 3.5, Figure 3.7. The telluroid is not an equipotential surface and defined as the surface whose normal potential is equal to the actual potential at point P (see Figure 3.7). In *Younis et al (2011)* a new adjustment-based approach is given, which enables the estimation of the coefficients $(C'_{n(k),m}, S'_{n(k),m})$ for regional SCH model V (3.8) as functions of coefficients $(C_{nm}, S_{nm})$ of a GGM. The estimated coefficients $(C'_{n(k),m}, S'_{n(k),m})$ *(Younis et al., 2011)* can be introduced as so-called direct observations in the integrated approach, and we thus have:

$$C'_{n(k),m} + v = \hat{C} \ and \ S'_{n(k),m} + v = \hat{S} \tag{3.16}$$

The integrated DFHRS approach, represented by formulas (3.9 – 3.16), is a far-reaching alternative to the model described by (3.1-3.8), because it allows both "geometrical" and "physical" observations and is free from a reduction. The integrated approach is presently being investigated and implemented in the DFHRS software version 5.0.

The DFHRS v. 5.0 needs no reduction on topography or interior masses, and (3.9) can be directly modelled as:

$$g_P + V_{g_P} = \sqrt{W_x{}^2 + W_y{}^2 + W_z{}^2}$$
$$= \sqrt{(V_x(C'_{nm}, S'_{nm}) + Z_x)^2 + (V_y(C'_{nm}, S'_{nm}) + Z_y)^2 + (V_z(C'_{nm}, S'_{nm}) + Z_z)^2} \tag{3.17}$$

and direct relation of $(\Phi, \Lambda)_{astr}$ from zenith cameras also reads reduction-free:

$$\Phi_{astr} + V_{\Phi_P} = tan^{-1}(\frac{W_z}{\sqrt{W_x^2 + W_y^2}}) \tag{3.18}$$

$$\Lambda_{astr} + V_{\Lambda_P} = tan^{-1}(\frac{W_y}{W_x}) \tag{3.19}$$

Formula (3.14) is used to derive the quasi-geoid from the estimated SCH-parameters. The quasi-geoid model or a grid (computed by the DFHRS approaches (3.1-3.8) or (3.9-3.16), respectively) can be transformed to a geoid-model by the equation:

$$N_G = N_{QG} + \frac{\bar{g} - \bar{\gamma}}{\bar{\gamma}} \cdot H \qquad (3.20)$$

The mean true gravity: $\bar{g}$ along the plumb line can be taken from a density model or a geopotential model, while the mean reference gravity value: $\bar{\gamma}$ - from the closed formulas related to the GRS80 *(Younis, 2013)*.

In case of orthometric heights as a national vertical height system (e.g. NAVD88 – North American Verical Datum 1988), the transformation equation between orthometric height $H_{orth}$ and normal height $H_{norm}$ can be used:

$$H_{norm} - H_{orth} = N_G - N_{QG} = \frac{\bar{g} - \bar{\gamma}}{\bar{\gamma}} \cdot H \qquad (3.21)$$

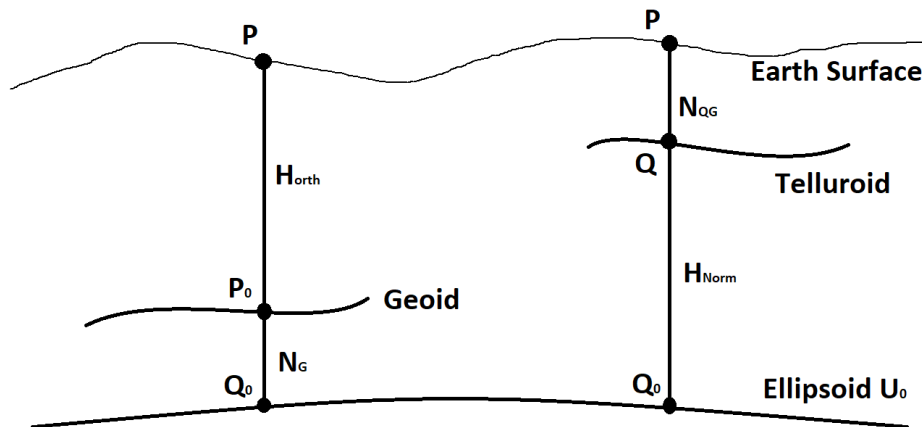The difference between normal height and orthometric height is depicted in Figure 3.5:



Figure 3.5. Orthometric height vs. normal height (*Younis, 2013*).

## 3.3.  Development of the DFHRS v. 5.1 software

The next development step of the software concerns the use of spherical-cap-harmonics as the designed carrier function for the DFHRS v.5.1. It enables – in the sense of the strict integrated geodesy approach, holding also for geodetic network adjustment – both a full gravity field and geoid determination. In addition, it allows the inclusion of gravimetric measurements, together with deflections of the vertical from digital zenith cameras, and all the other types of observations. The advantage of spherical-cap-harmonics (SCH) modelling in comparison to spherical harmonics (SH) that less parameters are needed in order to compute local area instead of whole sphere (*Younis et al., 2011*), (*Younis, 2013*). This method was developed by (*Haines, 1985a*), (*Haines 1985b*). The gravitational potential V in terms of SCH for a point P (r, α, θ) within the cap reads (*Haines, 1988*):

$$V(r, \alpha, \theta) = \frac{GM}{R} \sum_{k=0}^{k\ max} \left(\frac{R}{r}\right)^{n(k)} \sum_{m=0}^{k} (C'_{nm} cosm\alpha + S'_{nm} sinm\alpha)\bar{P}_{n(k),m}(cos\theta) \qquad (3.22)$$

The $C'_{nm}$ and $S'_{nm}$ coefficients are unknowns and have to be determined by least square estimation.

The basic concept behind SCH is to expand gravity potential V in two sets of basis functions which satisfies Laplace's equation (*De Santis &Torta, 1997*), (*De Santis et al., 1999*) within the spherical cap and are mutually orthogonal in each set.  The Legendre functions are chosen in order to satisfy the following boundary conditions (*Haines, 1985a*);

$$\frac{dP_{n_k}^m(\theta=\alpha)}{d\theta} = 0 \text{ for k} - \text{m} = \text{even}, \qquad (3.23)$$

$$dP_{n_k}^m(\theta = \alpha) = 0 \text{ for k} - \text{m} = \text{odd}, \qquad (3.24)$$

where a is the cap half-angle, and k is used to index (in ascending order) the roots $n_k$ of (3.23) and (3.24) at a given value of *m* (*De Santis, 1991*).

The local coordinate system is defined by cap opening angle and local pole is depicted in Figure 3.6.
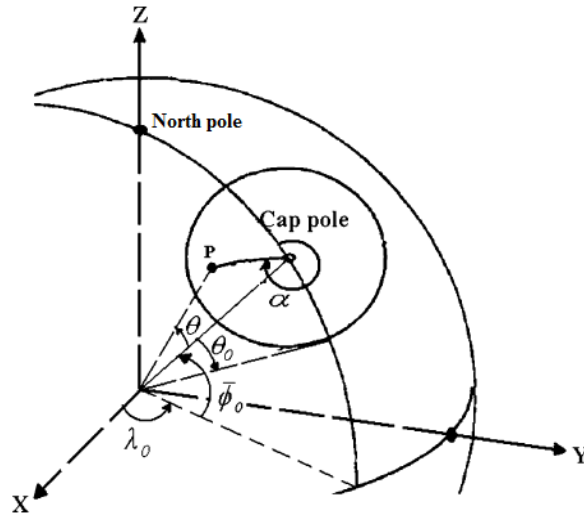
Figure 3.6. Spherical cap area with its own pole located at the origin of area of interest (*Younis, 2013*).

The starting point for the quasi-Geoid based theory of Molodensky implemented in the DFHRS-approach and software 5.0 reads with:

$$T_P = \left( V\left( r, \alpha, \theta \middle| C'_{nm}, S'_{nm} \right) + Z(x, y) - U(\beta, \alpha, u) \right)_P \tag{3.25}$$

$$N_{QG} = \frac{(V + Z - U)_P}{\gamma_Q} = \frac{T_P}{\gamma_Q} \tag{3.26}$$
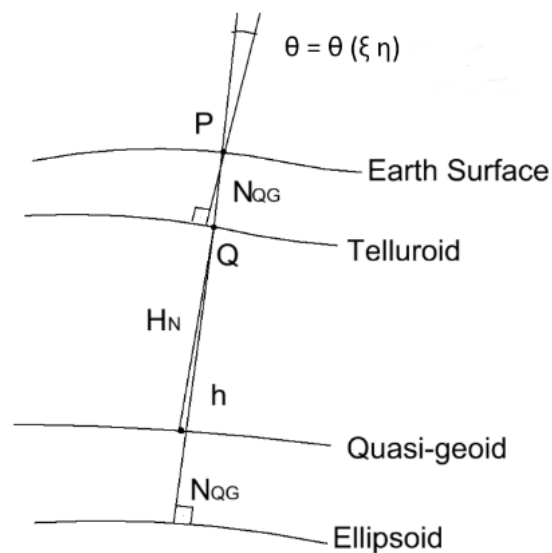


Figure 3.7. Deflection of vertical at point P (*author*)

Consistent with the above quasi-geoid theory of Molodensky and the Bruns theorem, we have zenith-camera based measured surface vertical deflections at surface point P, referring to the telluroid point Q (see Figure 3.7):

$$\xi_P = \varphi_{astr,P} - B \tag{3.27 a}$$

$$\eta_P = (\alpha_{astr,P} - L) \cdot cosB. \tag{3.27 b}$$

Starting with the quasi-geoid formula and introducing again the potential model related $T_P$ we get the vertical deflections at the Earth Surface P as (see Figure 3.7).

$$\xi_P = -\frac{dN_{QG}}{ds_{North}} = -\frac{\partial N_{QG}}{\partial B}\frac{\partial B}{\partial s_N} = -\frac{\partial B}{\partial s}\frac{\partial N_{QG}}{\partial B} = \frac{-1}{(M+h)}\frac{1}{\gamma_Q}\frac{\partial}{\partial B}T_P$$

$$= \frac{-1}{\gamma_Q(M+h)}\left(\frac{\partial T}{\partial B}\right)_P + \delta\xi_{norm.curv.} = \tag{3.28 a}$$

$$= -\frac{-1}{\gamma_{Q_j}\cdot(M_j+h_j)}\cdot\left(\frac{\partial T(C_{n(k),m,}S_{n(k),m})}{\partial B_j}\right)_{P_j} + \delta\xi_{norm.curv.}$$

$$\eta_P = -\frac{dN_{QG}}{ds_{East}} = -\frac{\partial L}{\partial s}\frac{\partial N_{QG}}{\partial L} = \frac{-1}{(N+h)cosB}\frac{1}{\gamma_Q}\frac{\partial}{\partial L}T_P$$

$$= \frac{-1}{\gamma_Q(N+h)cosB}\left(\frac{\partial T}{\partial L}\right)_P = \tag{3.28 b}$$

$$= \frac{-1}{\gamma_{Q_j}\cdot(N_j+h_j)\cdot cosB_j}\cdot\left(\frac{\partial T(C_{n(k),m,}S_{n(k),m})}{\partial L_j}\right)_{P_j},$$

For above differentiation of $T_P$ in the direction of the ellipsoidal latitude B and longitude L 4 different coordinate systems in $T_P$ have to be handled, as we have (3.25) the solution at first we bring together the local CAP system and the spherical system, we have:

$$r = r \tag{3.29 a}$$

$$tan\alpha = \frac{cos\varphi sin(\lambda - \lambda_0)}{sin\varphi cos\varphi_0 - cos\varphi sin\varphi_0 cos(\lambda - \lambda_0)} \tag{3.29 b}$$

$$cos\theta = sin\varphi sin\varphi_0 - cos\varphi cos\varphi_0 cos(\lambda - \lambda_0) \tag{3.29 c}$$

For the remaining 3 systems for the position of the point P, the common denominator are the Cartesian 3D coordinates (x, y, z) (*Jäger, R. 2002-2022*):

$$\begin{bmatrix} x \\ y \\ z \end{bmatrix} = \begin{bmatrix} r\cos\varphi\cos\lambda \\ r\cos\varphi\sin\lambda \\ r\sin\varphi \end{bmatrix} \tag{3.30}$$

$$\begin{bmatrix} x \\ y \\ z \end{bmatrix} = \begin{bmatrix} (N(B) + h)\cos(B)\cos(L) \\ N(B) + h)\cos(B)\sin(L) \\ \left(\dfrac{b^2}{a^2}N(B) + h\right)\sin(B) \end{bmatrix} \tag{3.31}$$

$$\begin{bmatrix} x \\ y \\ z \end{bmatrix} = \begin{bmatrix} u\sqrt{1 + \varepsilon^2/u^2}\,\cos\beta\cos\lambda \\ u\sqrt{1 + \varepsilon^2/u^2}\,\cos\beta\sin\lambda \\ u\sin\beta \end{bmatrix} \tag{3.32}$$

With (3.29 a, b, c), (3.30), (3.31) and (3.32) and the common relation to (x, y, z) we have consistency in the georeferencing and we can set up the derivatives $\left(\frac{\partial T}{\partial B}\right)_P$ (3.27a) and $\left(\frac{\partial T}{\partial L}\right)_P$ (3.27b) by applying the chain rule to (3.29 a, b, c) to (3.32).

So the vertical deflections parameterize now in DFHRS 5.x the carrier function of the spherical Cap harmonics potential and respective $C_{nm}$', $S_{nm}$' coefficients instead of polynomial coefficients used in the DFHRS approach and software 4.x. By DFHRS 5.x also surface gravity measurements $g_P$ can be included, in opposite the DFHRS 4.x.

From the final potential computed in a least squared adjustment the quasi-geoid can be computed again by using (3.29) and (3.30). A geoid can be computed afterward by applying:

$$N_G = N_{QG} + \frac{\overline{g} - \overline{\gamma}}{\overline{\gamma}}H \tag{3.33}$$

The method of spherical-cap-harmonics modelling in terms of integrated geodesy allows to compute precise quasi-geoid model to be used for GNSS measurements. Combination of all data gives an opportunity to define height reference surface using independent measurements (both geometrical and physical observations). The use of vertical deflections measurements allow to check/control reliability of heights computed by GNSS/levelling points. SCH in comparison to ordinary SH is fast method and does not need so much memory for computations (*Torge, 2001*), (*Vaniček, 1976*). The realization of this method combining all data and implementation in DFHRS v 5.0 version is developed under Visual Studio 2015 using C++ programming language.

## 3.4. Geoid determination based on the Stokes Approach

In this chapter the basic principle of Stokes approach is discussed. Though this method is neither an integrated approach nor Gauss-Markov approach, this method was used for Riga region in order to compare the results of two methods.

The GRAVSOFT Fortran software for the determination of a regional or local approximation to the anomalous gravity potential is based on the 3D Least-Squares Collocation (LSC) developed by (*Krarup, 1969; Moritz, 1972*) and its principle is described in this chapter. The software also implements the remove-compute-restore (*Hofmann-Wellenhof and Moritz, 2006*) method so that gravity variations outside the region of computation are accounted for by subtracting the contribution of a Global Geopotential Model (GGM) and so that statistical homogenization is achieved by removing the contribution of topographic short wavelength features (*Tscherning, 2008*).

In the RCR technique, the contribution of the long-wavelength component and the terrain effect are removed from terrestrial gravity anomalies (3.34). Accordingly, the reduced gravity are obtained by:

$$\Delta g_{res} = \Delta g_{FA} - \Delta g_{GGM} - \Delta g_{RTM} \tag{3.34}$$

where $\Delta g_{FA}$ – the free-air gravity anomaly on the geoid surface;

$\Delta g_{GGM}$ – the contribution of the GGM (e.g. EGM2008) to gravity anomaly;

$\Delta g_{RTM}$ – the terrain effect on gravity.

Then the reduced gravity anomalies are processed to obtain the geoid undulation, and finally the long-wavelength contribution and the effect of the topography are restored to the undulation (3.35). The geoid undulation with restored long-wavelength term and topographical effect can be summarized by:

$$\widetilde{N} = N_{GGM} + N_{\Delta g_{res}} + N_{RTM} \tag{3.35}$$

where $N_{GGM}$ – the contribution of the GGM;

$N_{\Delta g_{res}}$ – the residual geoidal height;

$N_{RTM}$ – the indirect effect of the terrain on the geoidal height.

The contributions of the GGM on the geoidal height and gravity anomaly are:

$$N_{GGM} = \frac{GM}{\gamma r} \sum_{n=2}^{n_{max}} \left(\frac{a}{r}\right)^n \sum_{m=0}^{n} (\bar{c}_{nm} cosm\lambda + \bar{s}_{nm} sinm\lambda) \bar{P}_{nm}(cos\theta) \qquad (3.36)$$

And

$$\Delta g_{GGM} = \frac{GM}{r^2} \sum_{n=2}^{n_{max}} (n-1) \left(\frac{a}{r}\right)^n \sum_{m=0}^{n} (\bar{c}_{nm} cosm\lambda + \bar{s}_{nm} sinm\lambda) \bar{P}_{nm}(cos\theta) \qquad (3.37)$$

can be calculated by the GGM coefficients (*Heiskanen and Moritz, 1967*). In equalities, GM is the product of the Earth's mass and the gravitational constant, g is the normal gravity on the reference ellipsoid, r is the radial distance to the computation point, a is the semi-major axis of the reference ellipsoid, Cnm and Snm are the fully normalized harmonic coefficients of the anomalous potential, Pnm is the fully normalized Legendre function, y and l are the geodetic co- latitude and longitude of the computation point P, respectively. In the RCR application of the study, a grid of reduced free-air anomalies, Dgred, obtained with the subtraction of GGM contributions from the mean free-air gravity anomalies, inputs to Stokes' kernel, then the residual geoid height is calculated by:

$$N_{\Delta g_{red}} = \frac{R}{4\pi\gamma} \iint_{\sigma} S(\psi) \Delta g_{red} d\sigma \qquad (3.38)$$

where σ denotes Earth's surface, $S(\psi)$ is the original Stokes' function. In gravity reduction, Helmert's second method of condensation can be applied. Accordingly, the terrain effect on gravity is computed as follows (*Heiskanen and Moritz, 1967*):

$$\Delta g_H = -\frac{G\rho R^2}{2} \iint_{\sigma} \frac{(H_Q - H_P)^2}{l_0^3} d\sigma \qquad (3.39)$$

and the terrain contribution on geoid height ($N_{topo}$) is calculated with spherical FFT (*Schwarz et al., 1990*) evaluation of Stokes' kernel using $\Delta g_H$ in "Compute" step (*Erol et al., 2009*). Also the indirect effect on the geoid heights for Helmert's second condensation method can be computed (*Sideris, 1994*):

$$\Delta N_{ind} = -\frac{\pi G\rho H_P^2}{\gamma} - \frac{G\rho R^2}{6\gamma} \iint_{\sigma} \frac{(H_Q^3 - H_P^3)}{l_0^3} d\sigma \qquad (3.40)$$

where

ρ – the topographic density,

$l_0$ – the planar distance between the points P and Q, $H_Q$, $H_P$ are the heights of the computation and running points, respectively. Finally the gravimetric geoid height is restored as the summation of the constituents in the "compute step".

The Riga region has been computed using the above mentioned method in terms of supervised master's thesis. For the computation of Riga quasi-geoid model such data sets were used:

1. Free-air gravity anomaly data provided by LGIA for the region from 56° 45' 00" to 57° 15' 00" latitude and  23° 30' 00" to 24° 45' 00" longitude;

2. Spherical harmonic model of the Earth's gravitational potential EGM2008;

3. Digital terrain model DTM developed by LGIA;

4. 15 Fitting GNSS/levelling points for Riga administrative territory and its close surroundings and 6 GNSS postprocessed points for checking the model.

Using GRAVSOFT software quasi-geoid model RĪGA'20 (see Figure 3.7.) (*Pahtusovs, 2021*) has been computed with a standard deviation of 1σ (68 %) probability – 6mm. To check quasi-geoid model 6 GNSS postprocessed points (ellipsoidal heights) were used and in the result normal height differences in range of -0.015 m to -0.007 m, with a mean difference -0.002 m were computed.
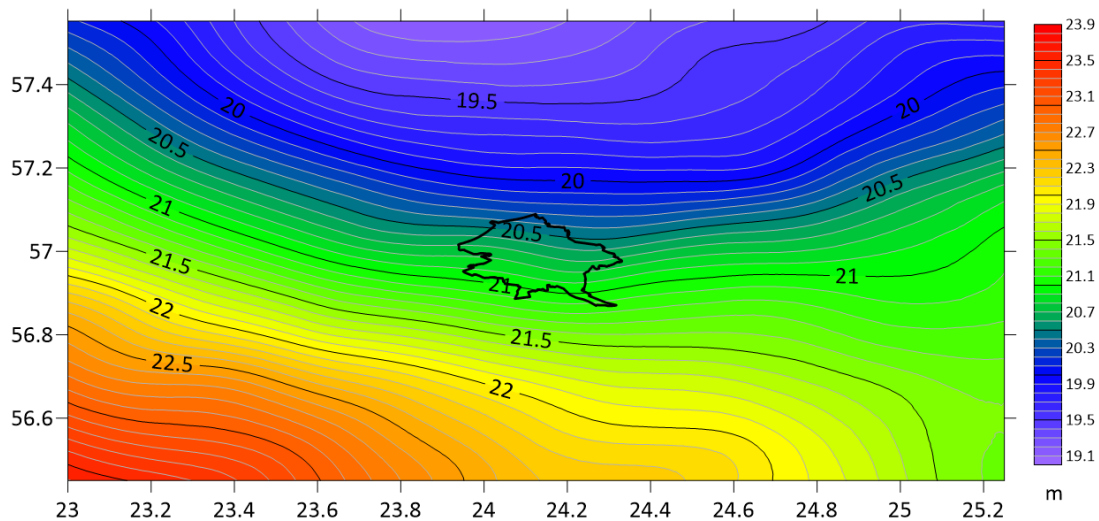


Figure 3.7. Quasi-geoid model for Riga region computed by GRAVSOFT software

(*Pahtusovs, 2021*)

Quasi-geoid model has been checked also in RTK (Real Time Kinematics) mode and in the result normal height differences using LatPos (*Zvirgzds, 2007*; *Zvirgzds, 2012*) were in range of -14 mm to 26 mm, with a mean difference of 8 mm, and in case of EUPOS-Rīga (*Balodis*

*et al., 2009*) system – the differences were obtained in a range of 23 mm to 27 mm, and a mean difference equal to 5 mm.

RĪGA'20 has been compared with LU_GGI'20 quasi-geoid model at 40 GNSS/levelling points. The results are depicted in Figure 3.8. and Table 4.
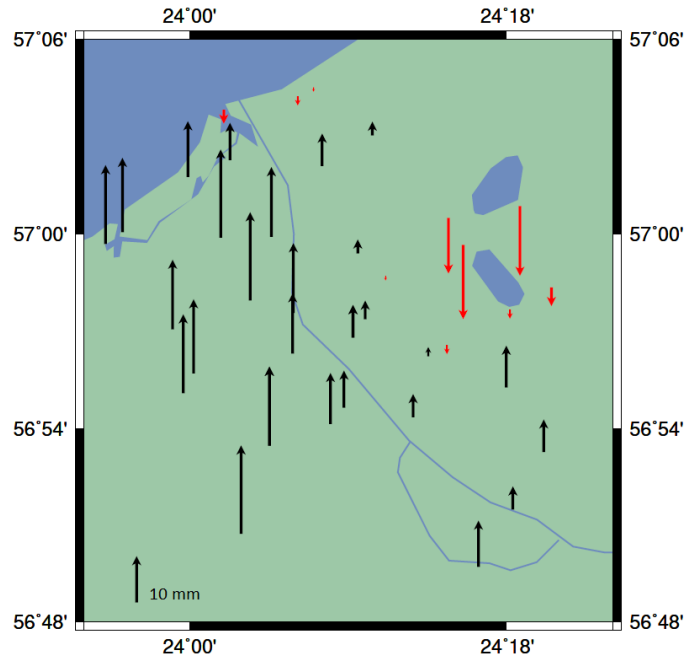


Figure 3.8. Comparison of RĪGA'20 and LU_GGI'20 at levelling points (*author*).

The differences vary from -0.016 m to 0.019 m, and the mean difference is equal to 0.006 m. As it can be seen from the Figure 3.8. the majority of differences are positive, what means that quasi-geoid model computed by GRAVSOFT is higher in a mean, especially it can be well seen from the left bank of the Daugava river.

Table 4

The differences of RĪGA'20 and LU_GGI'20.

| Nr. | Point | B | L | Δξ |
|-----|-------|-----------|-----------|--------|
| 1 | 1 | 56.857980 | 24.305300 | 0.005 |
| 2 | 37 | 57.008250 | 24.244450 | -0.012 |
| 3 | 75 | 57.050550 | 24.172550 | 0.003 |
| 4 | 173 | 56.950900 | 23.984010 | 0.015 |
| 5 | 249 | 56.938420 | 24.097310 | 0.013 |

73

| | | | | |
|---|---|---|---|---|
| **6** | 393 | 57.014300 | 24.311940 | -0.015 |
| **7** | 435 | 56.845520 | 24.048640 | 0.019 |
| **8** | 728 | 56.887760 | 24.334430 | 0.007 |
| **9** | 824 | 56.998530 | 24.077240 | 0.015 |
| **10** | 1128 | 57.037940 | 24.038190 | 0.008 |
| **11** | 1176 | 56.978440 | 24.185100 | -0.001 |
| **12** | 1277 | 56.928160 | 24.003810 | 0.016 |
| **13** | 1837 | 56.902110 | 24.133100 | 0.011 |
| **14** | 1870 | 56.956140 | 24.165860 | 0.004 |
| **15** | 1960 | 57.063800 | 24.032320 | -0.003 |
| **16** | 2885 | 57.070690 | 24.102160 | -0.002 |
| **17** | 3336 | 56.942870 | 24.242950 | -0.002 |
| **18** | 3389 | 56.891000 | 24.075380 | 0.017 |
| **19** | 3389 | 56.891000 | 24.075390 | 0.017 |
| **20** | 4407 | 56.965740 | 24.057210 | 0.019 |
| **21** | 4416 | 56.998010 | 24.029370 | 0.019 |
| **22** | 5340 | 56.974650 | 24.254680 | -0.011 |
| **23** | 5715 | 56.905610 | 24.211070 | 0.005 |
| **24** | 6330 | 56.972420 | 24.341700 | -0.004 |
| **25** | 6475 | 56.946650 | 24.154340 | 0.007 |
| **26** | 6475 | 56.946670 | 24.154290 | 0.007 |
| **27** | 6709 | 56.959380 | 24.097970 | 0.015 |
| **28** | 6980 | 57.029300 | 23.998350 | 0.012 |
| **29** | 7705 | 57.034820 | 24.125140 | 0.007 |
| **30** | 8000 | 56.989990 | 24.158840 | 0.003 |
| **31** | 8584 | 56.994430 | 24.258350 | -0.016 |
| **32** | 024C | 56.828400 | 24.272770 | 0.010 |
| **33** | 0753i | 57.075410 | 24.117050 | -0.001 |
| **34** | 114B | 56.961080 | 24.302520 | -0.002 |
| **35** | 1272i | 57.000900 | 23.936600 | 0.016 |
| **36** | 366A | 56.937010 | 24.225330 | 0.002 |

| 37 | 661A | 56.994800 | 23.920690 | 0.017 |
| 38 | 872i | 56.910530 | 24.145840 | 0.008 |
| 39 | 875A | 56.920950 | 24.299100 | 0.009 |
| 40 | RUTK | 56.918000 | 23.993950 | 0.017 |

## 3.5. Geoid determination by KTH method

The geoid calculation by KTH method was developed at the Royal Institute of Technology (KTH) in Stockholm. It is also well known method and is used in many countries (e.g. Abdalla et al., 2016). This method is based on the modification of Stoke's formula (*Sjöberg 1986; 1991; 2003a; 2003b*):

$$N = \frac{R}{4\pi\gamma} \iint_\sigma S(\psi)\Delta g d\sigma \tag{3.44}$$

where

$R$ – the mean Earth radius;

$\gamma$ – the normal gravity on the reference ellipsoid;

$\psi$ – the geocentric angle;

$\Delta g$ – the gravity anomaly;

$d\sigma$ – an infinitesimal surface element of the unit sphere $\sigma$;

$S(\psi)$ – the Stokes function which can be expressed as a series of Legendre polynomial $P_n(cos\psi)$ over the sphere (*Heiskanen and Moritz, 1967*):

$$S(\psi) = \sum_{n=2}^{\infty} \frac{2n+1}{n-1} P_n(cos\psi) \tag{3.45}$$

Where *n* is the spherical harmonics degree.

For geoid determination the surface integral in Stokes' formula (3.45), has to be applied over the whole Earth. Nonetheless, in practice, the area is limited to a small spherical cap so around the computational point due to limited coverage of available gravity anomaly. In this case the integral has to be truncated at the borders of the study area $\sigma_0$. Due to the neglection of gravity anomalies in the remote zone, a truncation error takes place. Molodensky et al. (1962) proposed that this truncation error can be reduced when Stokes' formula combines the terrestrial gravity anomalies

and long-wavelength information from the GGM. The method is called modification of Stokes' formula (*Abbak et al., 2012*). The KTH method combines terrestrial gravity data and longwavelength components of the gravity field in a stochastically modified Stokes' kernel. Accordingly, the stochastic KTH method uses the least squares principle to minimize the expected global mean square error of the modified Stokes formula (*Sjoberg, 1984; 1991; 2003b*)

$$\widetilde{N} = \frac{R}{4\pi\gamma} \iint_{\sigma_0} S^L(\psi)\Delta g d\sigma + \frac{R}{2\gamma} \sum_{n=2}^{M} b_n \Delta g_n \tag{3.46}$$

where

$S^L(\psi)$ – modified Stokes' function;

L – Maximum degree of the arbitrary parameters $S_n$ of the modification;

$\Delta g_n$ – gravity anomaly derived from GGM;

M – upper limit of the GGM.

The modified Stokes' function is:

$$S^L(\psi) = \sum_{n=2}^{\infty} \frac{2n+1}{n-1} P_n(cos\psi) - \sum_{n=2}^{L} \frac{2n+1}{n-1} S_n P_n(cos\psi) \tag{3.47}$$

where the first part of the right side of the equation is the original Stokes function, $S(\psi)$, in terms of Legendre polynomials. Generally the upper bound of the harmonics to be modified in Stokes' function, L, is arbitrary and may not necessarily be equal to M, the upper limit of the GGM.

In addition to the least-squares modification, the KTH approach also applies specific additive corrections. Thus the geoidal height $\widetilde{N}$ can be summarized by the following formula (Sjoberg, 2003b):

$$\acute{N} = \widetilde{N} + \delta N_{comb}^{top} + \delta N_{DWC} + \delta N_{comb}^{Atm} + \delta N_{ell} \tag{3.48}$$

where $\widetilde{N}$ is the approximate geoid undulation defined in equation (3), and the additive corrections are: $\delta N_{comb}^{top}$ – combined topographic correction including the sum of direct and indirect topographical effects on the geoid;

$\delta N_{DWC}$ – downward continuation (DWC) effect;

$\delta N_{comb}^{Atm}$ – combined atmospheric correction including the sum of the direct and indirect atmospherical effects;

$\delta N_{ell}$ – ellipsoidal correction for spherical approximation of the geoid in Stokes' formula to ellipsoidal reference surface.

The combined topographic correction $\delta N_{comb}^{top}$ can be computed by (*Sjoberg, 2007*):

$$\delta N_{comb}^{top} = -\frac{2\pi G \rho H^2}{\gamma}\left(1 + \frac{2H}{3R}\right) \tag{3.49}$$

Where G – the Newton gravitational constant;

$\rho$ – Earth's crust density;

H – the elevation of the topography.

The downward continuation (DWC) effect $\delta N_{DWC}$ in its terms can be computed by the sum of its components:

$$\delta N_{DWC} = \delta N_{DWC}^{1} + \delta N_{DWC}^{L1} + \delta N_{DWC}^{L2} \tag{3.50}$$

where

$$\delta N_{DWC}^{1} = \frac{\Delta g_P}{\gamma} H_P + 3\frac{\widetilde{N}}{r_P} H_P - \frac{1}{2\gamma}\frac{\partial \Delta g}{\partial r}\bigg|_P H_P^2 \tag{3.51}$$

,

$$\delta N_{DWC}^{L1} = \frac{R}{2\gamma}\sum_{n=2}^{M} b_n\left[(\frac{R}{r_P})^{n+2} - 1\right]\Delta g_n \tag{3.52}$$

and

$$\delta N_{DWC}^{L2} = \frac{R}{4\pi\gamma}\iint_{\sigma_0} S^L(\psi)\left[\frac{\partial \Delta g}{\partial r}\bigg|_P (H_P - H_Q)\right]d\sigma_0 \tag{3.53}$$

Where $r_p = R + H_p$ is the spherical radius of the point P, $H_P$ is the orthometric height of point P. The gravity gradient at point P is calculated based on (*Heiskanen and Moritz, 1967*):

$$\frac{\partial \Delta g}{\partial r}\bigg|_P = \frac{R^2}{2\pi}\iint_{\sigma_0}\frac{\Delta g_Q - \Delta g_P}{l_0^3}d\sigma_0 - \frac{2}{R}\Delta g_P \tag{3.54}$$

where

$$l_0 = 2R\sin(\frac{\psi_{PQ}}{2})$$

is the spherical distance between the computation point P and running point Q.

In the KTH scheme, the combined atmospheric effect can be approximated to topographic height H (*Sjoberg and Nahavandchi, 2000*).

$$\delta N_{comb}^{Atm} = -\frac{2\pi GR\rho^a}{\gamma}\sum_{n=2}^{M}\left(\frac{2}{n-1}-b_n\right)H_n - \frac{2\pi GR\rho^a}{\gamma}\sum_{n=M+1}^{M}\left(\frac{2}{n-1}-\frac{n+2}{2n+1}Q_n^M\right)H_n \quad (3.55)$$

where $\rho^a$ is the density of the atmosphere at sea level. An ellipsoidal correction calculated by simple formula (*Ellmann and Sjoberg, 2004*):

$$\delta N_{ell} \approx [(0,0036 - 0,0109\sin^2\varphi)\Delta g + 0.0050\tilde{N}\cos^2\varphi]Q_0^L \quad (3.56)$$

where $Q_0^L$ denotes the Molodensky truncation coefficient.

# 4. SPHERICAL HARMONICS AND GLOBAL MODELS

This chapter is devoted to the construction and manipulation of so-called global models of the anomalous potential. These are basically truncated series of spherical or ellipsoidal harmonics. These functions are so important in physical geodesy that they need to be carefully introduced and their mathematical properties have to be known by everyone dealing with gravity field representations (*Pavlis et al., 2006; Barnes et al., 2020*). In this chapter the definition of spherical harmonics definition, Legendre functions, development of global geopotential models are represented. New global model EGM2020 is about to release soon, and in order to contribute this model the collected vertical deflection data which were observed on the territory of Latvia has been provided to NGA.

## 4.1. Legendre functions

The definition of $P_n(t)$ as coefficients of the Taylor series of the function:

$$G(s,t) = \frac{1}{\sqrt{1 + S^2 - 2st}} \tag{4.1}$$

Also called the generating function of Legendre polynomials.

So, we have

$$G(s,t) = \sum_{n=0}^{+\infty} S^n P_n(t) \tag{4.2}$$

The series being convergent in the interval

$$0 \leq s < 1.$$

Note that in the end we want to substitute $t = cos\psi$, so we can restrict ourselves to study $P_n(t)$ in the interval:

$$-1 \leq t \leq 1$$

Corresponding to

$$0 \leq \psi \leq \pi.$$

Since (4.2) is a Taylor series, we can compute $P_n(t)$ from

$$P_n(t) = \frac{1}{n!} D_s^n G(s, t)|_{s=0}. \tag{4.6}$$

In this way for instance we can get:

$$P_0 \equiv 1, \ P_1(t) \equiv t, \ P_2(t) = \frac{1}{2}(3t^2 - 1), \ P_3(t) = \frac{1}{2}(5t^3 - 3t), \tag{4.7}$$

Suggesting that $P_n(t)$ are polynomials of degree $n$, with the same parity as $n$, i.e. even for $n$ even and odd for $n$ odd. We shall soon see that this is the case, however we will need a more handy tool than formula (4.6). In fact consider that $G(s,t)$ satisfies identically the relation

$$(1 + S^2 - 2st)D_s G(s, t) = (t - s)G(s, t). \tag{4.8}$$

If we insert series (4.2) into (4.8) and equate the coefficients of the same powers in $s$, we find the remarkable recursive relation:

$$(n + 1) P_{n+1}(t) = (2n + 1)t \, P_n(t) - n \, P_{n-1}(t) \tag{4.9}$$

Since we already know that $P_0 \equiv 1$, $P_1(t) \equiv t$, (4.9) allows the direct computation of $P_n(t)$ for any $t$.

Furthermore, not only (4.9) provides us with a rule for a very fast computation of $P_n$ up to $n$ equal to several thousands, but also gives us the possibility of better understanding the nature of $P_n(t)$.

First of all we now see that if $P_{n-1}$, $P_n$ are polynomials of degree n-1 n respectively, that $P_{n+1}$ is a polynomial of degree n+1; furthermore, if $P_{n-1}$ has a certain parity and $P_n$ the opposite parity, then $P_{n+1}$ has the same parity as $P_{n-1}$.

Moreover, by taking t=±1, (i.e. ψ=0 or π) in (4.1) and (4.2) we find:

$$\sum_{n=0}^{+\infty} s^n P_n(\pm 1) = \frac{1}{(1 \pm s)} = \sum_{n=0}^{+\infty} (\mp s)^n \; ; \tag{4.10}$$

(4.10) has to be an identity in s, so we have proved that

$$P_n(1) = 1, P_n(-1) = (-1)^n. \tag{4.11}$$

## 4.2. Fully normalized Legendre functions

The fully normalized associated Legendre functions $\bar{P}_{mn}(t)$ sometimes also called fully normalized harmonics, can be computed from the conventional associated Legendre functions $P_{n,m}$ by (*Torge, 1991*):

$$\bar{P}_{n,m}(t) = \sqrt{k(2n+1)\frac{(n-m)!}{(n+m)!}P_{n,m}(t)}, \tag{4.12}$$

$$with \; k = \begin{cases} 1 \; for \; m = 0; \\ 2 \; for \; m \neq 0. \end{cases}$$

The associated Legendre functions can be computed with the following recursive formulas (e.g., *Bronstein and Semendjajew, 1991; Abramowitz and Stegun, 1972*):

$$P_{n+1,0}(t) = (2n+1)tP_{n,0}(t) - nP_{n-1,0}(t) \tag{4.13a}$$

$$P_{n,n}(t) = (2n-1)uP_{n-1,n-1}(t) \tag{4.13b}$$

$$P_{n,m}(t) = P_{n-2,m}(t) + (2n-1)uP_{n-1,m-1}(t) \tag{4.13c}$$

With the starting values if we assume $t = sin\bar{\varphi}$ and $u = cos\bar{\varphi}$:

$$P_{0,0}(t) = 1$$
$$P_{1,0}(t) = t,$$
$$P_{1,1}(t) = u,$$
$$P_{2,0}(t) = \frac{3}{2}t^2 - \frac{1}{2},$$
$$P_{2,1}(t) = 3ut,$$

$$P_{2,2}(t) = 3u^2$$

However, these recursion formulas become numerically unstable for large *m* and *n* (>120) and you may have to use more sophisticated formulas (*Moore, 1999*). As example, one method from (*Holmes and Featherstone, 2002*) is introduced:

For the fully normalized *non-sectorial* (i.e., n > m) $\bar{P}_{n,m}(t)$ you can use the following recursion:

$$\bar{P}_{n,m}(t) = a_{n,m}t\bar{P}_{n-1,m}(t) - b_{n,m}t\bar{P}_{n-2,m}(t), for \; all \; n > m \quad\quad (4.14)$$

Where

$$a_{n,m} = \sqrt{\frac{(2n-1)(2n+1)}{(n-m)(n+m)}}$$

$$b_{n,m} = \sqrt{\frac{(2n+1)(n+m-1)(n-m-1)}{(n-m)(n+m)(2n-3)}}$$

The sectorial (i.e. *n=m*) $\bar{P}_{m,m}(t)$ serve as seed values for the recursion in Formula 4.14. Starting from $\bar{P}_{0,0}(t)=1$ and $\bar{P}_{1,1}(t)=\sqrt{3}u$, it can be computed from (*Moore, 1999*):

$$\bar{P}_{m,m}(t) = u\sqrt{\frac{2m+1}{2m}}\bar{P}_{m-1,m-1}(t) \quad\quad (4.15)$$

For all *m>1,* so, that:

$$\bar{P}_{m,m}(t) = u^m\sqrt{3}\prod_{i=2}^{m}\sqrt{\frac{2i+1}{2i}} \quad\quad (4.16)$$

## 4.3. Spherical Harmonics

The solid spherical harmonics are an orthogonal set of solutions of the Laplace equation represented in a system of spherical coordinates, e.g. (*Hobson, 1931; Freeden, 1985; Hofmann-Wellenhof and Moritz, 2005*). Thus, each harmonic potential, i.e. which fulfils Laplace's equation, can be expanded into solid spherical harmonics and can be solved e.g. using MATLAB (*Bucha and Janak, 2013; Trauth, 2006*). The spherical harmonic (or Stokes') coefficients represent in the

spectral domain the global structure and irregularities of the gravity field of the Earth (*Barthelmes, 2013*).

The equation relating the spatial and spectral domains of the geopotential is as follows:

$$W_a(r, \lambda, \varphi) = \frac{GM}{r} \sum_{l=0}^{l_{max}} \sum_{m=0}^{l} (\frac{R}{r})^l P_{lm}(sin\varphi) \cdot (C_{lm}^W cosm\lambda + S_{lm}^W sinm\lambda) \qquad (4.17)$$

Where:

$r, \lambda, \varphi$ – spherical geocentric coordinates of computation point (radius, longitude, latitude);

$R$ – reference radius;

$GM$ – product of gravitational constant and mass of the Earth;

$l, m$ – degree and order of spherical harmonic;

$P_{lm}$ – fully normalised Lengendre functions;

$C_{lm}^W$ , $S_{lm}^W$ – Stokes' coefficients (fully normalised).

Formula represents the Earth's gravity field with an accuracy depending on the accuracy of the coefficients $C_{lm}^W$ , $S_{lm}^W$ and a spatial resolution depending on the maximum degree $l_{max}$.

## 4.4.  Data and missions for the development of Global Geopotential models

The recent developments of GGMs have been based on satellite-only solutions or solutions that combine satellite and terrestrial measurements and, they have been produced in the form of spherical harmonic expansions (*Torge, 2001*). Three kinds of gravitational information are available for the development of high-degree combination models (*Pavlis, 1997*):

1. Information obtained from the analysis of satellite orbit perturbations, which is necessary for the accurate determination of the low degree part of the model. The European Space Agency (ESA) launched the Gravity field and steady-state Ocean Circulation Explorer (GOCE) in order to map the earth's gravity field. It carried a full-tensor gradiometer consisting of 6 three-degree-of-freedom accelerometer pairs oriented in three orthogonal directions over a very short baseline. All nine components of the differential acceleration tensor were measured independently, though not all with equal precision. The gravitational gradients are derived from them and angular accelerations and velocities derived from symmetry properties and star tracker data (*Rummel et al., 2011*). The other well known satellite missions for measuring gravity field are CHAllenging

Minisatellite Payload (CHAMP) (*Reigber et al., 1999*) and Gravity Recovery and Climate Experiment (GRACE) (*Tapley et al., 2004*).

2.  In order to solve both long and short wavelength features of the gravity field surface and airborne gravimetric data are used. This however requires global coverage with dense gravity data of high accuracy (which is problematic in some regions (*Marchenko and Dzhuman, 2015*). Though gravity anomaly data are susceptible to various systematic errors (*Heck, 1990*) and these errors, in conjunction with the non-uniformity of coverage, degrade the long wavelength integrity of the gravitational information which can be extracted from surface gravimetry, nevertheless, surface and airborne gravimetry presently provide the only data that can resolve short wavelength gravity features over land. In addition, ship borne gravity measurements help to separate the geoid from the dynamic ocean topography (DOT) signal when used in combination with satellite altimetry.

3. Satellite altimetery data (*Eshagh, 2021*) allows to perform the mapping of the field over the oceans, both in terms of accuracy and in terms of resolution. Satellite altimetry missions began at 1991 by launching ESA satellite ERS-1. The U.S.-French Topex/Poseidon (T/P) (*Fu et al., 1994*) was launched from Kourou in August 1992. T/P routinely provides measurements of the sea surface which, for the first time, are not significantly contaminated by radial orbit error (RMS radial orbit error at the ± 2 to 3 cm level). However, altimetric measurements are confined over the ocean areas bounded by the satellite's inclination, and furthermore provide a mapping of the sum of the geoid undulation plus the DOT. These aspects weaken somewhat the contribution of altimeter data in the determination of the long wavelength gravitational field and necessitate the appropriate modeling of the DOT when altimeter data are used in combination solutions. The complimentary character (both in a spectral as well as in a geographic sense) of satellite tracking, altimetry and surface gravimetry data, enables the determination of the gravitational field in combination solutions, over a wider band of its spectrum, with improved accuracy than can be obtained by using any of the three data types alone (*Pavlis, 1997*).

# 5. TESTS AND ANALYSIS

The three solutions of the quasi-geoid model for Latvia were prepared using different data sets: global geopotential model EGM2008 (*Pavlis et al., 2008a; Pavlis et al., 2008b; Pavlis et al., 2012*) and GNSS/levelling points; EGM2008, GNSS/levelling points and VD observed by DZC; and EGM2008 using additionally VD derivatives from the model, GNSS/levelling points and VD observed by DZC. The results of 3 solutions can be found in the Table 4.

Table 4

The statistical results of 3 solutions for quasi-geoid model evaluation using 3 data sets [in units of m].

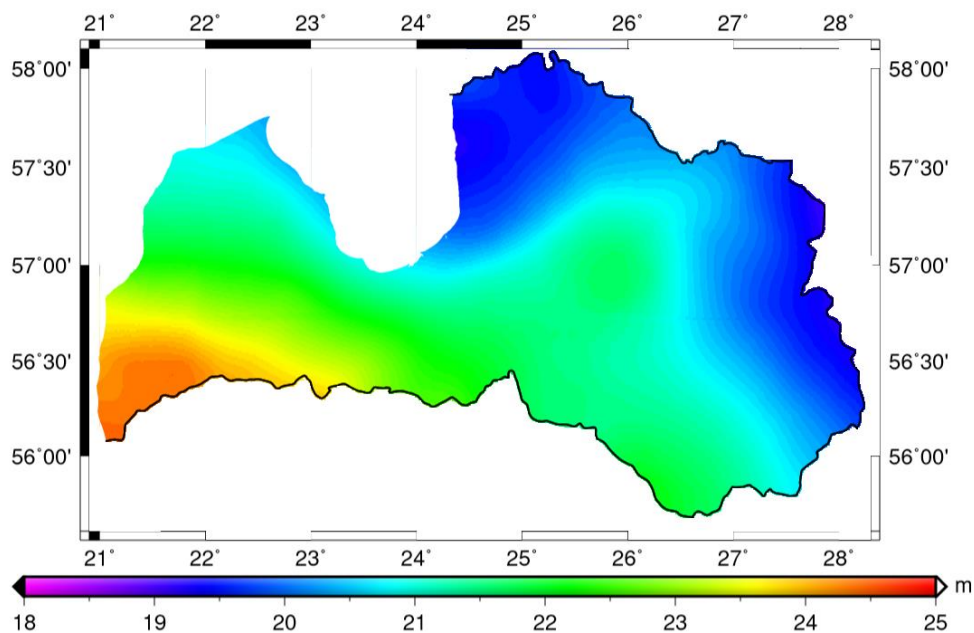| Data set | SD | Min | Max | Mean |
|---|---|---|---|---|
| **GNSS/levelling points + VD derivatives from EGM2008 + observed VD by DZC** | 0.006 | -0.012 | 0.012 | 0.000 |
| **EGM2008 (without VD)+GNSS/levelling points + VD by DZC** | 0.017 | -0.068 | 0.074 | 0.001 |
| **EGM2008 (without VD)+GNSS/levelling points** | 0.038 | -0.106 | 0.246 | 0.006 |



Figure 5.1. LU_GGI'20 quasi-geoid model (*author*)

The developed quasi-geoid model is depicted at Figure 5.1. The quasi-geoid heights vary from 18.94 m in the North and North-East at Estonian and Russian borders and 24.44 m in the South-West near the Baltic Sea and the Lithuanian border. The computed quasi-geoid model (A solution) has been compared with the national Latvian model LV'14 (*LGIA homepage*) and quasi-geoid model NKG2015 (*Ågren et al., 2016*) computed by the Nordic Geodetic Commission.
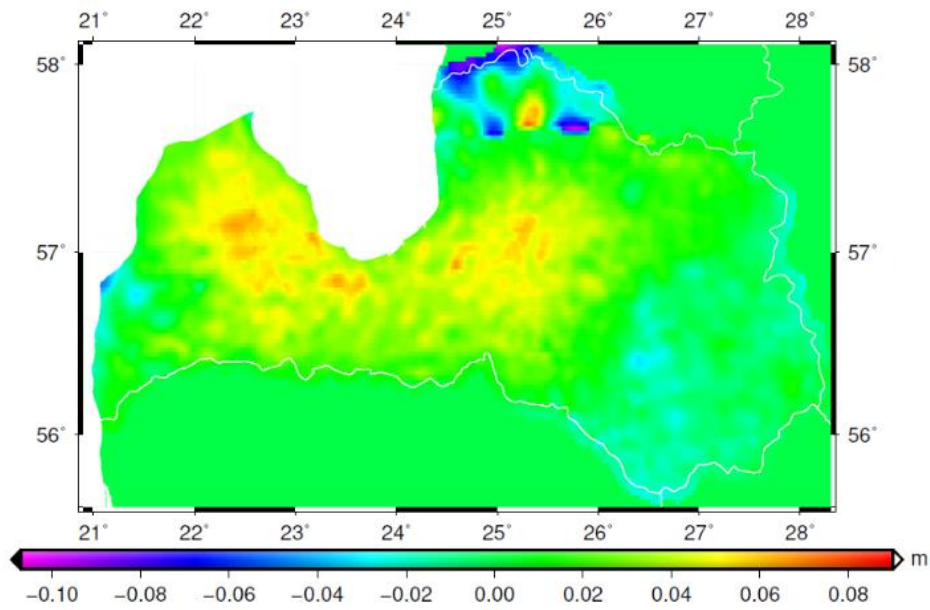


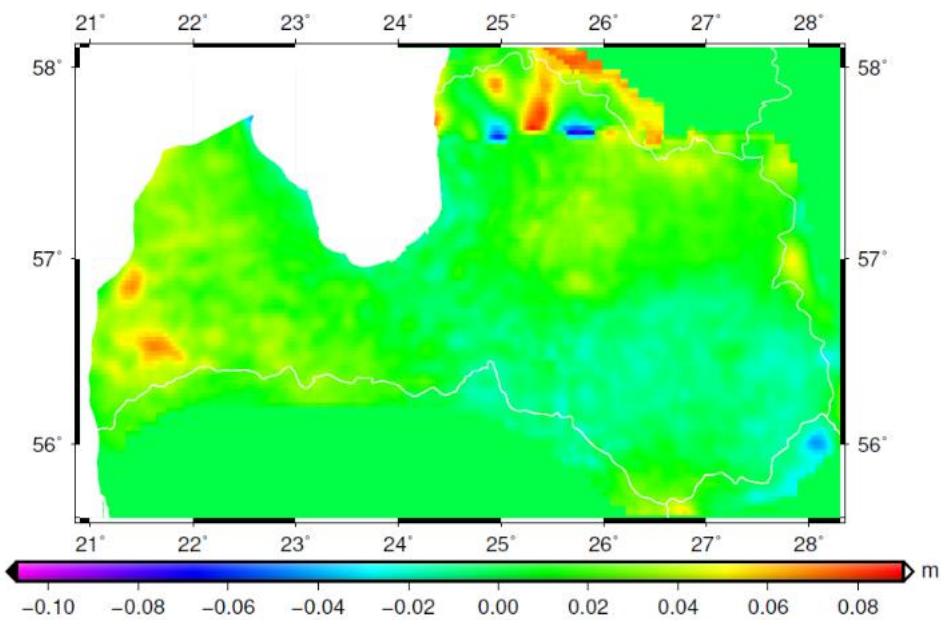Figure 5.2. The comparison of LU_GGI20 quasi-geoid and LV'14



Figure 5.3. The comparison of LU_GGI20 quasi-geoid and NKG2015

The comparison of LU_GGI'20 and LV'14 is depicted in Figure 5.2. The differences between LU_GGI'20 and NKG2015 are depicted in Figure 5.3. The average differences and standard deviations are depicted in Table 5.

<div align="right">Table 5</div>

The comparison of LU_GGI'20 quasi-geoid model with LV'14, NKG2015 models.

|  | *Min* | *Max* | *Avg* | *STDEV* |
|---|---|---|---|---|
| **LV'14** | -0.098 | 0.073 | 0.009 | 0.020 |
| **NKG2015** | -0.065 | 0.086 | 0.008 | 0.017 |

The comparison of the quasi-geoid heights and geodetic (h) minus normal heights (H) from LGIA database has also been performed for LU_GGI20 (Figure 5.4), LV'14 (Figure 5.5) and NKG2015 (Figure 5.6). The summary of these differences is depicted in Table 6.
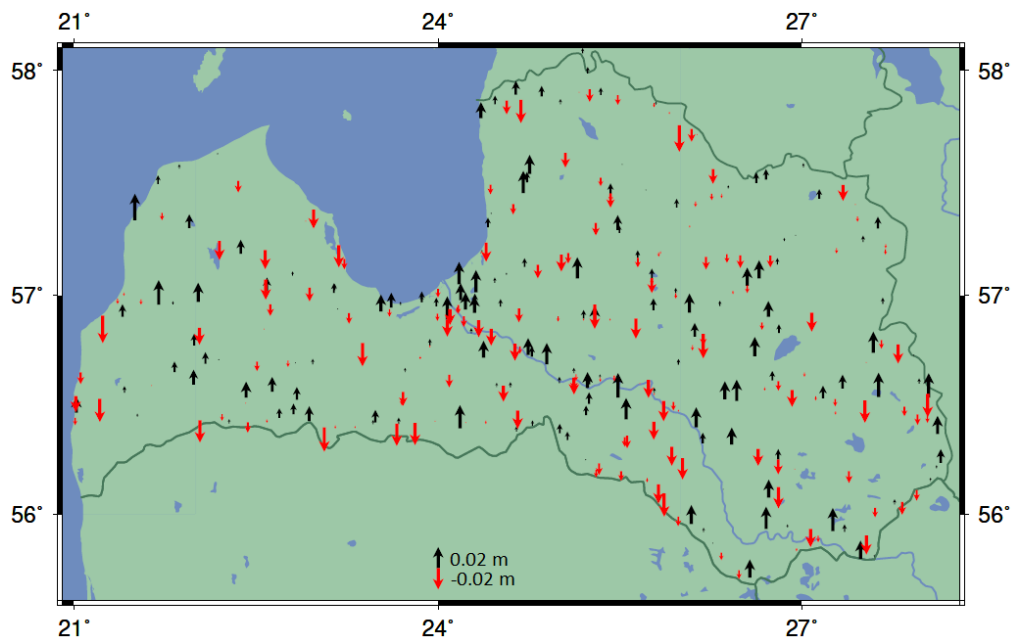


Figure 5.4. The difference between LU_GGI'20 quasi-geoid heights and h-H values from LGIA database (*author*)
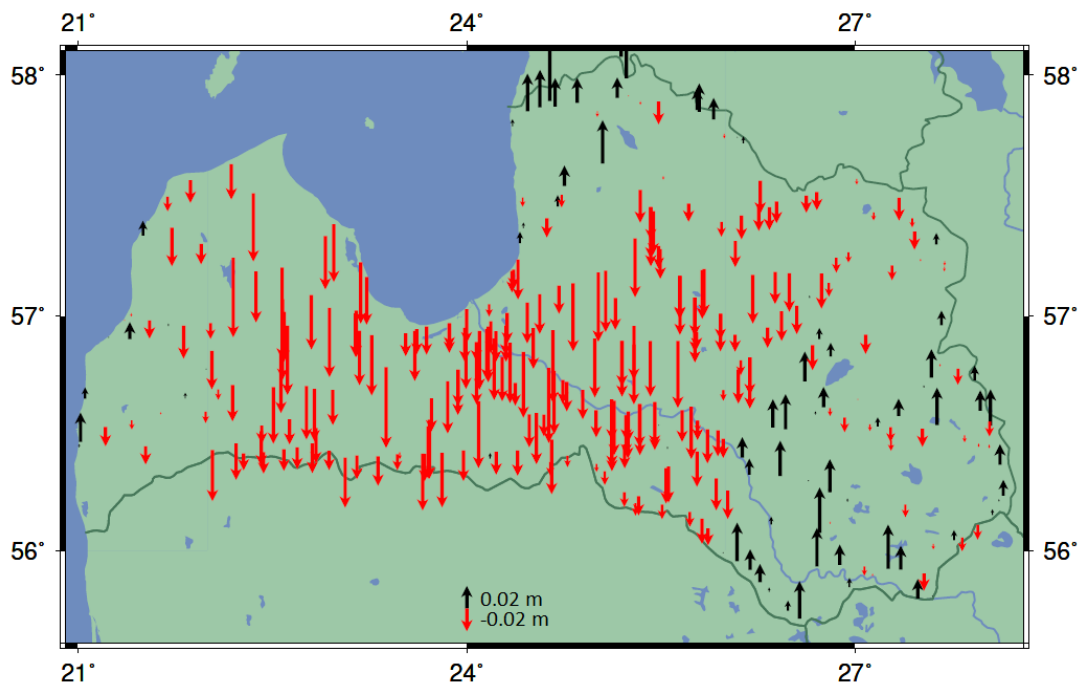
Figure 5.5. The difference between LV'14 quasi-geoid heights and h-H values from LGIA database (*author*).
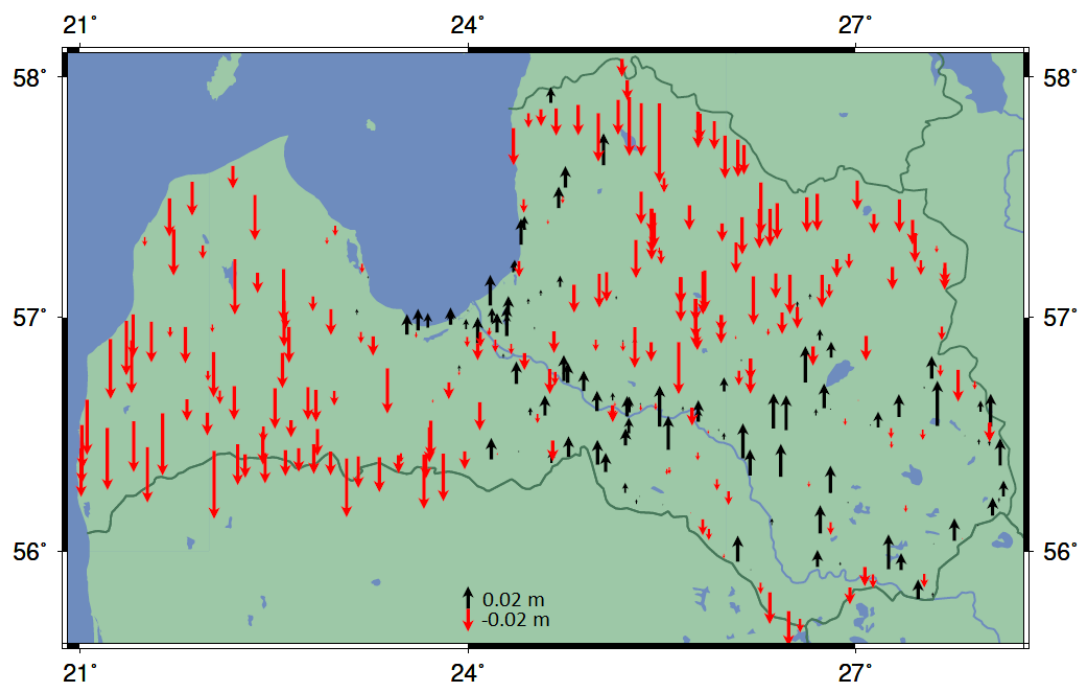


Figure 5.6. The difference between NKG2015 quasi-geoid heights and h-H values from LGIA database (*author*).

Table 6

The comparison of quasi-geoid heights and h-H values from LGIA database [in units of m].

|  | *Min* | *Max* | *Avg* | *STDEV* |
|---|---|---|---|---|
| **LU_GGI20** | -0.026 | 0.025 | 0.000 | 0.012 |
| **LV'14** | -0.081 | 0.082 | -0.017 | 0.026 |
| **NKG2015** | -0.070 | 0.040 | -0.010 | 0.021 |

Terrestrial VDs observed by DZC were compared with VD derivatives from global geopotential models (see Table 4), e.g. GGMplus (*Hirt et al., 2013*) and EGM2008, and computed the quasi-geoid model LU_GGI20. The results show a better correspondence with the GGMplus model by evaluating the standard deviation: 0.314 and 0.307 arcsec for $\xi$ and $\eta$ components respectively in comparison to 0.346 and 0.358 arcsec for $\xi$ and $\eta$ components for the EGM2008 model. The correspondence of terrestrial VD to derivatives computed from the LU_GGI20 quasi-geoid model is significantly better: the standard deviation is 0.055 and 0.046 arcsec for $\xi$ and $\eta$ respectively.

More statistics can be found in Table 7. The comparison of terrestrial VD observations to EGM2008 and GGMplus are depicted in Figure 5.7 and Figure 5.8 respectively.

Table 7

The comparison of terrestrial VD observations observed by DZC to GGMs, and LU_GGI20 [in units of arcsec].

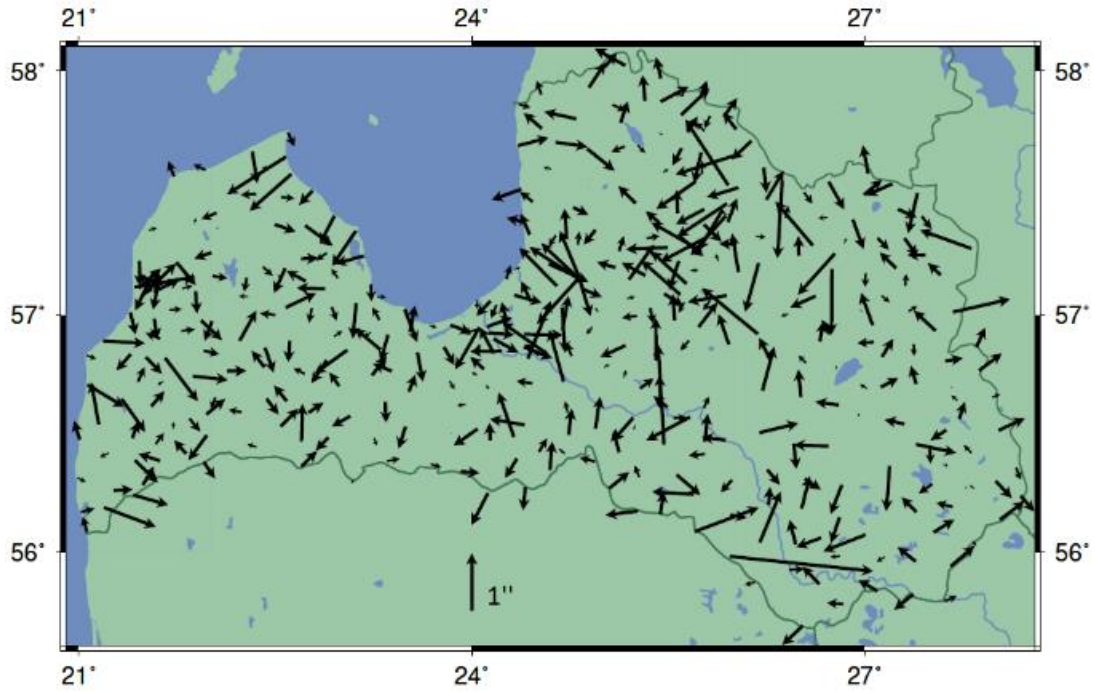|  | *Min* | | *Max* | | *Avg* | | *STDEV* | |
|---|---|---|---|---|---|---|---|---|
|  | $\xi$ | $\eta$ | $\xi$ | $\eta$ | $\xi$ | $\eta$ | $\xi$ | $\eta$ |
| **LU_GGI'20** | -0.348 | -0.190 | 0.216 | 0.162 | 0.007 | -0.002 | 0.055 | 0.046 |
| **GGMplus** | -1.300 | -1.370 | 1.105 | 1.194 | 0.008 | -0.025 | 0.314 | 0.307 |
| **EGM2008** | -1.351 | -1.031 | 1.747 | 2.509 | 0.013 | -0.024 | 0.346 | 0.358 |

Figure 5.7. The comparison of terrestrial VD and EGM2008 (*author*)
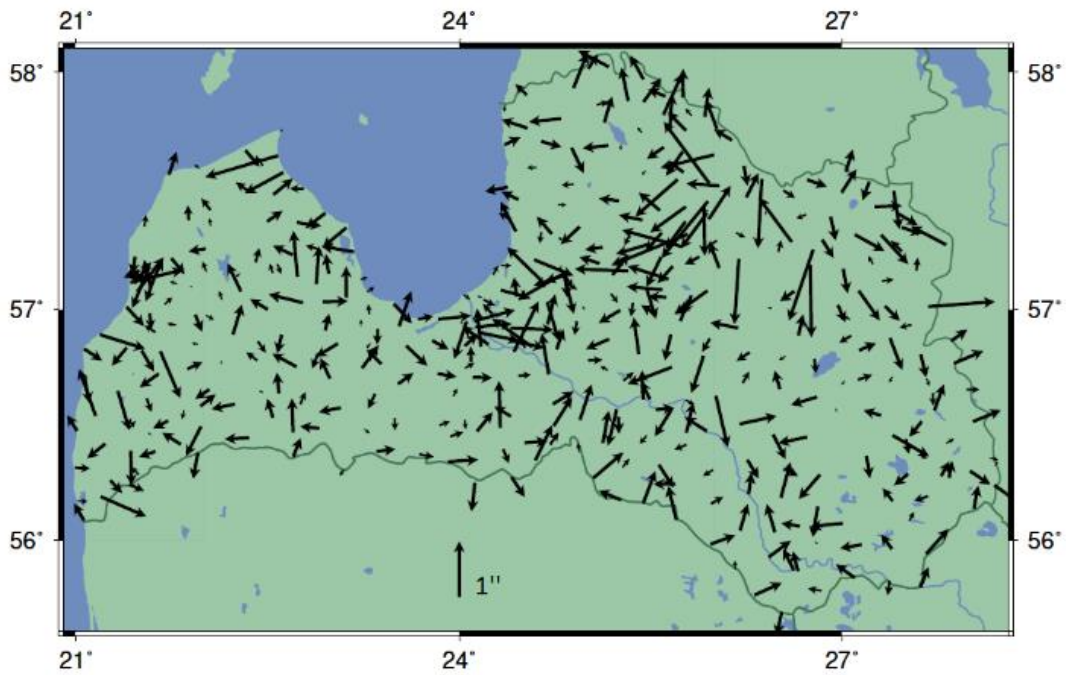


Figure 5.8. The comparison of terrestrial VD and GGMplus *(author)*

For the first time a high number of observations of terrestrial vertical deflections (VD) have been done on the territory of Latvia. The application of VD observations for the quasi-geoid model determination has shown the significant improvement of the computed quasi-geoid model. The standard deviation of the observation residuals after the adjustment, considering both VD derivatives from GGMs and terrestrial VD observed by DZC is equal to 0.006 m. Terrestrial VD observations fit the developed quasi-geoid model well, and the standard deviation for ξ and η components are equal to 0.055 and 0.046 arcsec respectively. Comparing the terrestrial VD observations to GGMs: no significant difference in standard deviation between GGMplus and EGM2008 was found, though the maximum difference for η component was 2 times less for GGMplus model. The final LU_GGI20 quasi-geoid model corresponds better to the NKG2015 model: the average difference is equal to 0.008 m in comparison to the LV'14 model, where this difference is equal to 0.009 m. The quasi-geoid heights have also been compared to ellipsoidal minus levelling heights: the standard deviation is equal to 0.012 m with minimum and maximum differences -0.026 m and 0.025 m respectively. As astrogeodetic deflections of the vertical are an additional observation group, being independent from gravimetric geoid models and gravity observations, the combination of both gravity data and terrestrial VD observations, together with the stochastic prior information of the SCH coefficients from a global gravity field model, give a complete integrated approach for quasi-geoid determination. In this context, the next research step should deal with the 1st order design problem of the optimal positions of VD and gravity observations for regional gravity field determination.

The next research step concerning the DZC, is to test the DZC in various environments for the investigation of anomalous refractions in zenith. It will include long-term observations for seeking characteristics of anomalous refraction in several test sites during various weather conditions. Simultaneous observations with two adjacent DZCs will be a method to distinguish instrument-attributed variations from changes in the measured quantity itself and find the spatial properties of anomalous refraction effects.

Further in-depth study will be involved aiming at a comprehensive characterization of the DZC VESTA; it will include testing of various instrumental settings, such as analyses of the CCD binning parameter, star magnitude and star colour impacts on accuracy.

# MAIN CONCLUSIONS

1) The improved methodology and software allowed to conclude:

   a) The use of terrestrial vertical deflection observations or $(\Phi, \Lambda)_{ast}$ instead for quasi-geoid determination significantly improves the precision of it: the achieved precision is equal to 0.017 m in comparison to 0.038 m when vertical deflections were ignored.

   b) The standard deviation of the observation residuals after the adjustment, considering both VD derivatives from GGMs and terrestrial vertical deflections observed by Digital Zenith Camera is equal to 0.006 m.

   c) Terrestrial VD observations fit the developed quasi-geoid model well, and the standard deviation for $\xi$ and $\eta$ components are equal to 0.055 and 0.046 arcsec respectively.

   d) The final LU_GGI'20 quasi-geoid model corresponds better to the NKG2015 model: the average difference is equal to 0.008 m in comparison to the LV'14 model, where this difference is equal to 0.009 m.

   e) The quasi-geoid heights have also been compared to ellipsoidal minus levelling heights: the standard deviation is equal to 0.012 m with minimum and maximum differences −0.026 m and 0.025 m respectively.

2) The carried out and post-processed 414 vertical deflection observations fit well the global geopotential models:

   a) no significant difference in standard deviation between GGMplus and EGM2008 was found: 0.314 arcsec and 0.346 arcsec for $\xi$ component; 0.307 arcsec and 0.358 arcsec for $\eta$ component respectively.

   b) average differences are equal to 0.008 arcsec and 0.013 arcsec for $\xi$ component, and -0.025 arcsec and -0.024 arcsec for $\eta$ component respectively.

3) The used methodology was compared with GRAVSOFT algorithms based on collocation method and remove-restore technique. The region of Riga was compared and the results showed the average difference between the LU_GGI2'0 quasi-geoid heights and ellipsoidal heights minus normal heights from data base equal to 0.017 m in comparison to RIGA'20 quasi-geoid computed with GRAVSOFT equal to 0.022 m, what proves that developed methodology fits better than remove-restore technique.

# REFERENCES

1. Abbak, R. A., Erol, B., and Ustun, A. (2012) "Comparison of the KTH and remove–compute–restore techniques to geoid modelling in a mountainous area", Computers & Geosciences, Volume 48, 2012, Pages 31-40, ISSN 0098-3004, https://doi.org/10.1016/j.cageo.2012.05.019.

2. Abdalla, A., and Green, C. (2016) "Utilisation of Fast Fourier Transform and Least-squares Modification of Stokes formula to compile a gravimetric geoid model over Khartoum State: Sudan". Arab J Geosci 9, 236 (2016). https://doi.org/10.1007/s12517-015-2117-8

3. Abele, M., Balodis, J, Janpaule, I., Lasmane, I., Rubans, A., and Zarins, A. (2012) "Digital zenith camera for vertical deflection determination," Geodesy and Cartography 38: 2012, pp. 123–129. https://doi.org/10.3846/20296991.2012.755324.

4. Abramowitz, M. and Stegun, I. A. (1972). Handbook of Mathematical Functions. Dover Publications, Inc., New York, pp. 1046.

5. Ågren, J., Strykowski, G., Bilker-Koivula, M., Omang, O., Märdla, S., Forsberg, R., Ellmann, A., Oja, T., Liepins, I., Parseliunas, E., Kaminskis, J., Sjöberg, L., and Valsson, G. (2016). The NKG2015 gravimetric geoid model for the Nordic-Baltic region. 10.13140/RG.2.2.20765.20969.

6. Balodis, J., Silabriedis, G., Caunite, M., Janpaule, I., Balodis, K., Rubans, A., Aleksejenko, I., Otto, R., Ratkus, B., Reiniks, M., Mitrofanovs, I., Plotnikovs, S., Zvirgzds, J. (2010) EUPOS®-RIGA NETWORKELEVATION ANALYSES. International Symposium on Global Navigation Satellite Systems. Space-Based and Ground-Based Augmentation Systems and Applications. Berlin. Germany. 30 November – 2nd December 2009; Conference Proceedings. Senate Department for Urban Development. Berlin. Germany 2010; Publication ISBN 978-3-938373-93-4;

7. Balodis, J., Morozova, K., Reiniks, M., and Normand, M. (2017) IOP Conference Series: Materials Science and Engineering, Volume 251, 3rd International Conference on Innovative Materials, Structures and Technologies (IMST 2017) 27–29 September 2017, Riga, Latvia

8. Barnes, D., Barnes, D., Beale, J., Small, H., and Ingalls, S. (2020): Introducing EGM2020, EGU General Assembly 2020, Online, 4–8 May 2020, EGU2020-9884, https://doi.org/10.5194/egusphere-egu2020-9884, 2020

9. Barthelmes, F (2013) Definition of Functionals of the Geopotential and their Calculation from Spherical Harmonic Models, Theory and formulas used by the calculation service of the International Centre for Global Earth Models (ICGEM) http://icgem.gfz-potsdam.de/ICGEM/, Scientific Technical Report STR09/02, Revised Edition, 2013

10. Bronstein, I. N. and Semendjajew, K. A. (1991). Taschenbuch der Mathematik. B. G. Teubner Verlagsgesellschaft, Stuttgart, 25. Edition, pp. 824.

11. Bucha, B., and Janák, J. (2013). A MATLAB-based graphical user interface program for computing functionals of the geopotential up to ultra-high degrees and orders. Computers & Geosciences. 56. 186–196. 10.1016/j.cageo.2013.03.012.

12. A. Celms, I. Reķe, D. Rekus and G. Balevičius, "National Height System Testing in Baltic Countries Using GNSS Measurements," 2017 Baltic Geodetic Congress (BGC Geomatics), 2017, pp. 257-262, doi: 10.1109/BGC.Geomatics.2017.38.

13. Ceylan, A. (2009) "Determination of the deflection of vertical components via GPS and levelling measurement: A case study of a GPS test network in Konya, Turkey," Scientific research and essay Vol. 4, (12), pp. 1438-1444.

14. Crombaghs, M., de Min E., and Strang van Hees, G. (2002) "The first absolute gravity measurements in The Netherlands, period 1991-1999", Publications on Geodesy 50, ISBN 90 6132 275 8, ISSN 0165 1706 https://ncgeo.nl/downloads/50Crombaghs.pdf

15. Dach, R., S. Lutz, P. Walser, P. Fridez (Eds); (2015): Bernese GNSS Software Version 5.2. User manual, Astronomical Institute, University of Bern, Bern Open Publishing. DOI: 10.7892/boris.72297; ISBN: 978-3-906813-05-9.

16. Ellmann, A., Märdla, S., and Tõnis, O. (2019) "The 5 mm geoid model for Estonia computed by the least squares modified Stokes's formula", Survey Review, DOI: 10.1080/00396265.2019.1583848

17. Eshagh, M. (2021) Satellite Gravimetry and the Solid Earth, Chapter 2 - Satellite gravimetry observables, Elsevier, Pages 45-90, ISBN 9780128169360, https://doi.org/10.1016/B978-0-12-816936-0.00002-5.

18. Farahani, H., Klees, R., and Slobbe, D. (2017) "Data requirements for a 5-mm quasi-geoid in the Netherlands". Studia Geophysica et Geodaetica. 10.1007/s11200-016-0171-7.

19. Featherstone, W. E. and Lichti, D. D. (2008) "Fitting gravimetric geoid models to vertical deflections", *Journal of Geodesy* **83**(6):583-589, 2008. DOI: 10.1007/s00190-008-0263-4

20. Förste, C., Bruinsma, S. L., Abrikosov, O., Lemoine, J.-M., Marty, J. C., Flechtner, F., Balmino, G., Barthelmes, F., Biancale, R. (2014): EIGEN-6C4 The latest combined global gravity field model including GOCE data up to degree and order 2190 of GFZ Potsdam and GRGS Toulouse. https://doi.org/10.5880/ICGEM.2015.1

21. Foroughi, I., and Tenzer, R. (2017) "Comparison of different methods for estimating the geoid-to-quasigeoid separation". Geophysical Journal International. 210. 1001-1020. 10.1093/gji/ggx221.

22. Freeden, W., (1985). Computation of spherical harmonics and approximation by spherical harmonicexpansions, Report / Department of Geodetic Science and Surveying, the Ohio State University; 362, Ohio.

23. Fu, L.-L., Christensen, E. J., Yamarone, C. A., Lefebvre, M., Ménard, Y., Dorrer, M., and Escudier, P. (1994), TOPEX/POSEIDON mission overview, J. Geophys. Res., 99( C12), 24369– 24381, doi:10.1029/94JC01761.

24. Haines, G. (1985a) "Spherical Cap Harmonic Analysis", *Journal of Geophysical Research*, Vol. **90** No. B3.

25. Haines, G. (1985b) "Spherical Cap Harmonic Analysis of Geomagnetic Secular Variation over Canada 1960-1983"*, Journal of Geophysical Research*, Vol. **90** No. B14.

26. Haines, G. (1988) "Computer programs for Spherical Cap Harmonic Analysis of Potential and General Fields", *Computer & Geosciences*, Vol. **14**, No. 4.

27. Halicioglu, K., Deniz, R., and Ozener, H. (2012a) "Determination of Astro-Geodetic Vertical Deflections using Digital Zenith Camera System in Istanbul, Turkey," FIG Working week, Rome, Italy, 2012.

28. Halicioglu, K., Deniz, R., and Ozener, H. (2012b) "Digital zenith camera system for Astro-Geodetic applications in Turkey," Journal of Geodesy and Geoinformation, Chamber of Surveying and Cadastre Engineers vol. 1, Issue 2, Journal No. 106, 2012, pp. 115-120. Doi: 10.9733/jgg.131212.1.

29. Haritonova, D., Balodis, J., Janpaule, I., and Morozova, K., (2015). IOP Conference Series: Materials Science and Engineering, Volume 96, 2nd International Conference on Innovative Materials, Structures and Technologies 30 September to 2 October 2015, Riga, Latvia

30. Heck, B. (1990) An evaluation of some systematic error sources affecting terrestrial gravity anomalies. Bull. Geodesique 64, 88–108. https://doi.org/10.1007/BF02530617

31. Heiskanen, W., and Moritz, H. (1967). Physical Geodesy. W.H. Freeman and Company, London.

32. Heiskanen, W., and Moritz, H. (1984) Physical Geodesy.

33. Hirt, C. and Bürki, B. (2002) "The Digital Zenith camera – A new high-precision and economic astrogeodetic observation system for real-time measurement of deflections of the Vertical," Proceed. 3rd Meeting International Gravity and Geoid Comission of the International Association of Geodesy, Thesaloniki (ed. I. Tziavos), Editions Ziti, 2002, pp. 161-166.

34. Hirt C., Reese B., Enslin H. (2005) "On the Accuracy of Vertical Deflection Measurements Using the High-Precision Digital Zenith Camera System TZK2-D". In: Jekeli C., Bastos L., Fernandes J. (eds) Gravity, Geoid and Space Missions. International Association of Geodesy Symposia, vol 129. Springer, Berlin, Heidelberg, DOI: https://doi.org/10.1007/3-540-26932-0_34

35. Hirt, C., Bürki, B., Guillaume, S., and Featherstone, W. (2010a) "Digital Zenith Cameras – State-of-the-Art Astrogeodetic Technology for Australian Geodesy," Proceedings FIG International Congress, Sydney, Australia.

36. Hirt, C., Bürki, B, Somieski, A., and Seeber, G. (2010b). "Modern Determination of vertical deflections using digital zenith cameras," Journal Surveying Engineering 136(1), Feb 2010, 1-12. DOI: 10.1061/_ASCE_SU.1943-5428.0000009.

37. Hirt, C., Claessens, S., Fecher, T., Kuhn, M., Pail, R., and Rexer, M. (2013). "New ultra-high resolution picture of Earth's gravity field". Geophysical Research Letters. 40. 10.1002/grl.50838.

38. Hobson, E. W., (1931). The Theory of Spherical and Ellipsoidal Harmonics, Cambridge University Press, Cambridge.

39. Hofmann-Wellenhof, B. and Moritz, H., (2005). Physical geodesy, Wien [et al.]: Springer, 2005

40. Hofmann-Wellenhof, B., Legat, K. and M. Wieser (2003): Navigation - Principles of Positioning and Guidance. Springer.

41. Hofmann-Wellenhof, B., and Moritz, H. (2006) Physical Geodesy, second edi. Springer Wien NewYork, Austria

42. Holmes, S. A. and Featherstone, W. E. (2002). A unified approach to the Clenshaw summation and the recursive computation of very high degree and order normalised associated Legendre functions Journal of Geodesy, 76(5).

43. Hwang, C., Wang, C., and Lee, L. (2002). "Adjustment of relative gravity measurements using weighted and datum-free constraints". Computers & Geosciences - COMPUT GEOSCI. 28. 1005-1015. 10.1016/S0098-3004(02)00005-5.

44. Ince, E. S., Barthelmes, F., Reißland, S., Elger, K., Förste, C., Flechtner, F., Schuh, H. (2019): ICGEM – 15 years of successful collection and distribution of global gravitational models, associated services and future plans. - Earth System Science Data, 11, pp. 647-674,DOI: http://doi.org/10.5194/essd-11-647-2019. (accessed 1 February, 2022)

45. Janpaule, I., Jäger, R. J., Younis, G., Kaminskis, J., & Zariņš, A. (2013) "DFHRS-based computation of quasi-geoid of Latvia". Geodesy and Cartography, 39(1), 11-17. https://doi.org/10.3846/20296991.2013.788827

46. Jäger, R. (2002-2022) Satellite Geodesy. International Masterprogramme Geomatics (MSc). Lecture Notes. Karlsuhe University of Applied Sciences.

47. Jäger, R. (2010) "Geodätische Infrastrukturen für GNSS-Dienste (GIPS)," Festschrift zur Verabschiedung von Prof. Dr.-Ing. G. Schmitt. Karlsruhe Institute of Technology (KIT), ISBN 978-3-86644-576-5. pp.151 – 169.

48. Jäger, R., Kaminskis, J., Strauhmanis, J., and Younis, G. (2012) "Determination of quasi-geoid as height component of the geodetic infrastructure for GNSS positioning services in the Baltic States," Latvian J. of Physics and Technical Sciences 3, pp. 5–15.

49. Jäger, R. (2000-2022): DFHBF-Website, http://dfhbf.de/ (accessed 1 April, 2022)

50. Jekeli, C. (1999) "An analysis of vertical deflections derived from high-degree spherical harmonic models", *Journal of Geodesy,* vol. **73**, pp 10-22.

51. Jekeli, C. (2001:) Inertial Navigation Systems with Geodetic Applications. Walter de

Gruyter.

52. Kaminskis, J. (2010) "Latvijas ģeoīda modelis un tā attīstība". Doctoral Thesis Riga: [RTU], 2010. 150 p. (in Latvian)

53. LGIA homepage: https://www.lgia.gov.lv/en/latvian-quasi-geoid-model

54. Kostelecký, J., Klokočník, J., Bucha, B., Bezděk, A., and Förste, C. (2015) Evaluation of gravity field model EIGEN-6C4 by means of various functions of gravity potential, and by GNSS/levelling OAJ Geoinformatics FCE CTU vol. 14, No 1 ttps://doi.org/10.14311/gi.14.1.1

55. Krarup, T., (1969). A Contribution to the Mathematical Foundation of Physical Geodesy. Publication No. 4, Danish Geodetic Institute, Copenhagen. 80 pages.

56. Marchenko, Alexander & Dzhuman, Bohdan. (2015). Regional quasigeoid determination: an application to Arctic Gravity project. Geodynamics Geodynamics (ISSN 1992-142X), Lviv, Ukraine. 1. 7-20.

57. Moore, R. (1999) "How to Compute Geoid Undulations (Geoid Height Relative to a Given Reference Ellipsoid) from Spherical Harmonic Coefficients for Satellite Altimetry Applications" Mathematics Department, Macquarie University, Sydney http://mitgcm.org/~mlosch/geoidcookbook/node16.html (accessed March, 2022).

58. Moritz, H., (1972). Advanced least-squares Methods. Report no. 175, Department of Geodetic Science, Ohio State University. 132 pages.

59. Moritz, H., (1980) Advanced Physical Geodesy, Wichmann, Karlsruhe, 1980

60. Morozova, K., Balodis, J., Jäger, R., Zariņš, A., and Rubāns, A. (2017a) "Digital Zenith Camera's Results and Its Use in DFHRS v.4.3 Software for Quasi-geoid Determination" From: 2017 Baltic Geodetic Congress (BGC Geomatics), Poland, Gdansk, 22.-25. June, 2017. Piscataway: IEEE, 2017, 174.-178.lpp. ISBN 978-1-5090-6041-2. e-ISBN 978-1-5090-6040-5. Available from: doi:10.1109/BGC.Geomatics.2017.74

61. Morozova, K., Jäger, R., Balodis, J., and Kaminskis, J. (2017b) "Software Development and Its Description for Geoid Determination Based on Spherical-Cap-Harmonics Modelling Using Digital-Zenith Camera and Gravimetric Measurements Hybrid Data". IOP Conference Series: Materials Science and Engineering, 2017, Vol.251, pp.1-10. ISSN 1757-8981. e-ISSN 1757-899X. Available from: doi:10.1088/1757-899X/251/1/01206.

62. Niebauer, T. M., Hoskins, J. K., and Faller, J. E. (1986), Absolute gravity: A reconnaissance tool for studying vertical crustal motions, J. Geophys. Res., 91( B9), 9145–9149, doi:10.1029/JB091iB09p09145.

63. Owusu-Banahene, W. (2013) "Further development of the DFHRS concept and software (C++) under Visual Studio 2012 and computation of the Geoid for Albania," Master's thesis Hochschule Karslruhe - University of Applied Sciences.

64. Pahtusovs, M. (2021) "Lokālā kvaziģeoīda modeļa izveidošana". Master's Thesis Riga: [RTU], 2021. 121 p. (in Latvian)

65. Parseliunas, E., Petroskevicius, P., Birvydiene, R. and Obuchovski, R., (2011). Investigation of the automatic gravimeters scintrex CG-5 and analysis of gravimetric measurements, NVIRONMENTAL ENGINEERING, The 8th International Conference May 19–20, 2011, Vilnius, Lithuania, Selected papers, SSN 2029-7106 print / ISSN 2029-7092 online, Vilnius Gediminas Technical University, 2011

66. Pavlis, N. K. (1997) Development and Applications of Geopotential Models, Second International School for the Determination and use of the Geoid, Rio de Janeiro, Brazil, 1997

67. Pavlis, N. K., Factor, J. K., and Holmes, S. (2006) "Terrain-Related Gravimetric Quantities Computed for the Next EGM"

68. Pavlis, N. K, Holmes, S. A., Kenyon, S. C., and Factor, J. K. (2008a): An Earth Gravitational model to degree 2160: EGM2008, *General Assembly of the European Geosciences Union*, Vienna, Austria

69. Pavlis, N. K., Holmes, S. A., Kenyon, S. C. and Factor, J. K. (2008b). EGM2008: An overview of its development and evaluation. , 23-27 June, 2008: National Geospatial-Intelligence Agency, USA, presented at conference: Gravity, Geoid and Earth Observation 2008, Chania, Crete, Greece.

70. Pavlis, N. K., Holmes, S. A., Kenyon, S. C., and Factor, J. K. (2012), The development and evaluation of the Earth Gravitational Model 2008 (EGM2008), J. Geophys. Res., 117, B04406, doi:10.1029/2011JB008916.

71. Reigber, C., Schwintzer, P., and Lühr, H. (1999), The CHAMP geopotential mission, Bol. Geofis. Teor. Appl., 40, 285– 289.

72. Rummel, R., Yi, W., and Stummer, C. (2011) GOCE gravitational gradiometry. Journal of Geodesy 85:777–790. doi: 10.1007/s00190-011-0500-0

73. Sanchez, L. (2013) Classical height systems, vertical datum standardisation (unification), Towords a modern vertical reference system, 11th International School of the Geoid Service: heights and height datum, Loja, Ecuador, October 7-11, 2013.

74. Santis, De, A., and Torta, J. (1997) "Spherical Cap Harmonic Analysis: a comment on its proper use for local gravity field representation", *Journal of Geodesy*, Vol. **71**, 1997

75. Santis, De, A., Torta, J. M., and Lowes, F. J. (1999) "Spherical Cap Harmonics Revisited and their Relationship to Ordinary Spherical Harmonics" *Phys. Chem. Earth* (A), Vol. **24**, No. 11-12, pp 935 – 941

76. Santis, De, A. (1991) "Transalted origin Spherical Cap Harmonic analysis", *Geophysical Journal International* **106**, 253-263

77. Schneid, S. (2006): Investigation of a Digital FEM Height Reference Surface as Vertical Reference Surface, PhD Thesis, University of Nottingham.

78. Schwarz, K., Sideris, M. and Forsberg, R. (1990). The Use of FFT Techniques in Physical Geodesy. Geophysical Journal International. 100. 485 - 514. 10.1111/j.1365-246X.1990.tb00701.x.

79. Sjoberg, L.E. (1984) "Least Squares Modification of Stokes and Venning–Meinesz Formulas by Accounting for Errors of Truncation, Potential Coefficients and Gravity Data". Technical Report. Department of Geodesy, Institute of Geophysics, University of Uppsala.

80. Sjöberg, L. E., (1986). "Comparison of some methods of modifying Stokes' formula". Boll. Geod. Sci. Aff., 46(2), pp. 229-248.

81. Sjöberg, L. E., (1991). "Refined least squares modification of Stokes formula". Manusc.Geod, 16, pp. 367-375.

82. Sjoberg, L.E., Nahavandchi, H. (2000). "The atmospheric geoid effects in Stokes' formula". Geophysical Journal International 140, 95–100.

83. Sjöberg, L. E., (2003a). "A computational scheme to model geoid by the modified Stokes formula without gravity reductions". Journal of Geodesy, 74, pp. 255-268.

84. Sjöberg, L.E., (2003b). A general model of modifying Stokes formula and its least squares solution. Journal of Geodesy, 77, pp. 459-464. http://dx.doi.org/10.1007/s00190-003-0346-1

85. Sjoberg, L.E., (2003c). A solution to the downward continuation effect on the geoid determination by Stokes formula. Journal of Geodesy 77, 94–100.

86. Sjoberg, L.E., (2005). A discussion on the approximations made in the practical implementation of the remove–compute–restore technique in regional geoid modeling. Journal of Geodesy 78, 645–653.

87. Sjoberg, L.E. (2007) "The topographic bias by analytical continuation in physical geodesy". Journal of Geodesy 87, 345–350.

88. Sjöberg, L. (2018) "On the geoid and orthometric height vs. quasigeoid and normal height". Journal of Geodetic Science, 8(1), pp. 115-120. Retrieved 30 Jan. 2019, from doi:10.1515/jogs-2018-0011

89. Tapley, B. D., Bettadpur, S., Watkins, M., and Reigber, C. (2004), The gravity recovery and climate experiment: Mission overview and early results, Geophys. Res. Lett., 31, L09607, doi:10.1029/2004GL019920.

90. Touati, F., Idres, M., and Kahlouche, S. (2009). "A Robust Method for Relative Gravity Data Estimation with High Efficiency". Surveys in Geophysics. 31. 69-83. 10.1007/s10712-009-9088-9.

91. Tenzer, R., Hirt, C., Claessens, S., and Novák, P. (2015) "Spatial and Spectral Representations of the Geoid-to-Quasigeoid Correction". Surveys in Geophysics. 36. 627-658. 10.1007/s10712-015-9337-z.

92. Torge, W. (1989) Gravimetry, Walter de Gruyter, Berlin, New York, 1989

93. Torge, W. (2001) Geodesy: Third completely revised and extended edition, Walter de Gruyter, Berlin, New-York.

94. Trauth M. H., (2006) MATLAB® Recipes for Earth Sciences Springer-Verlag Berlin Heidelberg 2006

95. Tscherning, C.C. (2008) Geoid determination by 3D least-squares collocation, 2008

96. Vaniček, P. (1976) Physical Geodesy, Lecture notes No. 43, University of New Brunswick.

97. Vaníček, P., Kingdon, R., and Marcelo, S. (2012) "Geoid versus quasigeoid: A case of physics versus geometry". Contributions to Geophysics and Geodesy. 42. 101-118. 10.2478/v10126-012-0004-9.

98. Voigt, C., Denker, H., and Hirt, C. (2009) "Regional Astrogeodetic Validation of GPS/Levelling Data and Quasigeoid Models. In: Sideris M.G. (eds) Observing our Changing Earth. *International Association of Geodesy Symposia*, vol **133**, Springer, Berlin, Heidelberg

99. Wang, Y.M., Sánchez, L., Ågren, J. et al. (2021) Colorado geoid computation experiment: overview and summary. J Geod 95, 127. https://doi.org/10.1007/s00190-021-01567-9

100. Xu, G. (2007): GPS – Theory, Algorithms and Applications. Springer

101. Yang, H. J. (2013) Geoid Determination Based on a Combination of Terrestrial and Airborne gravity Data in South Korea, Report No. 507, Geodetic Science, The Ohio State University, Columbus, Ohio 43210, 2013

102. Younis, G., Jäger, R., and Becker, M. (2011) "Transformation of global spherical harmonic models of the gravity field to a local adjusted spherical cap harmonic model," Arabian Journal of Geosciences. DOI 10.1007/s12517-011-0352-1.

103. Younis, G. (2013) "Regional Gravity Field Modeling with Adjusted Spherical Cap Harmonics in an Integrated Approach," Schriftenreihe Fachrichtung Geodäsie der Technischen Universität Darmstadt (39), Darmstadt, Germany, ISBN978-3-935631-28-0.

104. Younis, G. (2015). Practical method to solve large least squares problems using Cholesky decomposition. Geodesy and Cartography. 41. 113-118. 10.3846/20296991.2015.1086118.

105. Zarins, A., Janpaule, I., and Kaminskis, J., (2014). On reference star recognition and identification. Geodesy and Cartography 40 (4): 143-147.

106. Zariņš, A., Rubans, A., and Silabriedis, G. (2016) "Digital zenith camera of the University of Latvia," Geodesy and Cartography, 42:4, pp. 129-135. http://dx.doi.org/10.3846/20296991.2016.1268434.

107. Zarins, A., Rubans, A., and Silabriedis, G. (2018). Performance analysis of Latvian zenith camera. Geodesy and Cartography, 44(1), 1-5. https://doi.org/10.3846/gac.2018.876

108. Zvirgzds, J. (2007). Geodetic meausurements using GPS base station system LatPos.

Geomatics 11, RTU, Riga: 81-89.

109. Zvirgzds, J. (2012). Rational system LatPos, PhD Thesis, Riga Technical university, Department of Geomatics, Riga, 2012, 264p.

110. Лобанов, А. М. (2017) Гравиразведка Краткий курс, Москва УДК 550.83:553.3/4

111. Молоденский М.С., Еремеев В.Ф., Юркина М.И. (1960) Методы изучения внешнего гравитационного поля и фигуры Земли. Труды ЦНИИГАиК. Вып. 131, Геодезиздат, 1960. — 251

112. Молоденский М.С. (2001) Избранные труды: Гравитационное поле, фигура и внутреннее строение Земли. Москва: Издательство «Наука», 2001

113. Молоденский М.С (1945) Основные вопросы геодезической гравиметрии, Труды центрального научно-исследовательского института геодезии, аэросъемки и картографии, выпуск 42, Издательство геодезической и картографической литературы ГУГК при СНК СССР, Москва, 1945

114. Огородова, Л. Б., Шимбирев, Б. П., Юзефович, А. П. (1978) Гравиметрия. М., «Недра», 325 с., УДК 528.5(075.8)

115. Юзефович, А. П., Огородова, Л. В. (1980) Гравиметрия: Учебник для вузов. – М.: Недра, – 320 с. УДК 528.15

# CONFIRMATION

I hereby declare that the Doctoral Thesis "Parameter Estimation on hybrid Zenith Camera and Gravimeter Data for Integrated Gravity Field and Geoid Determination based on Spherical-Cap-Harmonics Modelling" submitted for the review to Riga Technical University for the promotion to the scientific degree of Doctor of Engineering Sciences is my own. I confirm that this Thesis has not been submitted to any other university for the promotion to other scientific degree.